ALMA MATER STUDIORUM
UNIVERSITÀ DI BOLOGNA

DOTTORATO DI RICERCA IN ASTROFISICA

Ciclo 36

Settore Concorsuale: 02/C1 - ASTRONOMIA, ASTROFISICA, FISICA DELLA
TERRA E DEI PIANETI

Settore Scientifico Disciplinare: FIS/05 - ASTRONOMIA E ASTROFISICA

Investigation of the obscuring torus in AGN using multi-wavelength SED

Presentata da: Dhrubojyoti Sengupta

Supervisore: Prof. Cristian Vignali
Co-supervisore: Dr. Stefano Marchesi, Prof. Francesca Pozzi

Coordinatore Dottorato: Prof. Andrea Miglio

Esame finale anno 2024

To maa and baba

"The important thing is not to stop questioning. Curiosity has its own reason for existence."
– Old Man's Advice to Youth: Never Lose a Holy Curiosity. (1955)
Albert Einstein

Abstract

It is commonly accepted that in the local Universe, nuclear obscuration in active galactic nuclei (AGN) is caused by the circum-nuclear material of molecular and dusty clouds called "torus". However, the obscuring medium's geometrical, physical, and chemical properties are far from being accurately known. During my PhD, I worked on characterizing the properties of this medium by analyzing the X-ray and multi-wavelength spectral energy distributions of several accreting supermassive black holes at $z \sim 0$.

Diffuse X-ray emission from the central regions of accreting supermassive black holes in AGN is responsible for most of the cosmic X-ray background (CXB) radiation from a few keV to a few hundred keV. The contribution of unobscured AGN to the CXB is almost completely resolved into point-like sources at E< 10 keV. Compton-thick AGN (CT-AGN; i.e. line-of-sight (LOS) column density $> 10^{24}$ cm^{-2}) significantly contribute ($\sim 15 - 20\%$) to the CXB around its peak ($\sim 20 - 30$ keV). In the local Universe ($z \leq 0.1$), the fraction of CT-AGN revealed by the X-ray observations is found to be $\sim 5\% - 10\%$. This reveals a large discrepancy with the predictions of AGN population synthesis models, which postulate that the fraction of local CT-AGN should be of $\sim 20\% - 50\%$ to model the CXB properly. Therefore, to fill the gap between observations and model predictions, a complete census of obscured AGN is needed at different wavelengths. Moreoever, one of the most efficient method of identifying AGN is in the X-ray band, where even heavily obscured AGN gets detected. In the first part of thesis, I have carried out a X-ray spectral analysis of seven heavily obscured AGN candidates in the local Universe (z < 0.05). These local Seyfert 2 galaxies are observed using sensitive E<10 keV observations with *Chandra* and XMM-*Newton*, coupled with NuSTAR data at E>10 keV, to examine the properties (i.e., obscuration, covering factor) of the torus from an X-ray point of view over the required broad ($\sim 0.5 - 50$ keV) energy range. This is being done by using the most up-to-date X-ray torus models such as `MYTorus` and `borus02`. These models allow for a proper geometrical characterization of the obscuring material in the smooth/clumpy configurations. The result shows, three candidates from the sample are found to be *bona fide* CT-AGN, i.e., they have LOS column density $N_{\mathrm{H,LOS}} > 10^{24}$ cm^{-2} at the $>3\,\sigma$ confidence level. Three of them are classified as Compton-Thin AGN, having $N_{\mathrm{H,LOS}} \approx 10^{22-24}$ cm^{-2}, despite having average torus column density $N_{\mathrm{H,tor}} > 10^{24}$ cm^{-2}. Finally, only one source is found to be significantly less obscured than what was previously claimed based on a joint Swift XRT-BAT fit, a result that further highlights the importance of using *NuSTAR* and XMM-*Newton* to reliably constrain the properties of heavily obscured

AGN. I also found the average column density for the sources in our sample to be $\sim 5 - 20$ times larger than LOS column density, showing either significantly clumpy distribution of the torus clouds along the LOS or a highly dense reflection medium within the inner region of the torus. Combining the analysis of these seven sources with all the previous X-ray analysis on the CT-AGN candidates at z $<$ 0.05, the updated census shows only 35 out of 414 ($\sim 8\%$) AGN are *bona fide* CT-AGN, which is still far below than the predicted fraction from CXB population synthesis models.

In the second part of the thesis, for a more in-depth analysis of the torus in heavily obscured AGN, I have selected NGC 6300, which was classified as a 'transient' or changing-look AGN candidate undergoing through a period of low activity in the observations of early 2000s. This source was previously studied in Jana et al., 2020 by X-ray spectral analysis using phenomenological torus models and MYTorus, considering nine observations from 2007 to 2016. I have carried out a comprehensive and systematic X-ray spectroscopic analysis of NGC 6300, including a new *Chandra* observation taken in 2020. Here, we have used all the latest X-ray torus models: borus02, UXCLUMPY and XCLUMPY for a proper geometrical characterization of the torus in both smooth and clumpy configurations. We used X-ray observations of Suzaku and *Chandra* for E$<$ 10 keV and *NuSTAR* observations to fit within the energy range 3 to 50 keV. The X-ray spectral analysis found no variability along LOS column density, but from the last observation of 2020, an existing signature of intrinsic flux variability is found. We also found the signature of an the inner CT-ring of gas, responsible for the reflection dominated spectra in the hard X-ray band. Along with X-ray analysis, we used aperture photometry to extract fluxes from the optical to far-infrared (FIR) band and used it for broad-band SED fitting tool XCIGALE, using the best-fit results of X-ray spectral fitting. We did so, to investigate the torus geometry with its host galaxy properties in the mid-IR and X-rays, taking into account all of the physical processes and components of AGN. We derived the optical depth, accretion rate, dust and gas influence in obscuration, stellar properties from the SED fitting.

Contents

1 Introduction

In 1908, Edward A. Fath made a notable discovery at the Lick Observatory, finding two unique "spiral nebulae" within the Milky Way— NGC 1068 and NGC 3031 (Messier 81). These objects exhibited an unusual spectrum, featuring strong emission lines instead of the expected absorption lines associated with stellar activities (Fath, 1909). Later, at Lowell Observatory, Vesto M. Slipher observed NGC 1068 with enhanced quality and resolution, identifying emission lines with a broad velocity width ~ 1000 km/s (Slipher, 1917). About a decade later, Edwin P. Hubble's work revealed that around 400 nebulae (now recognized as galaxies) exist beyond the Milky Way, including NGC 1068, marking the dawn of extragalactic astronomy (Hubble, 1926). Over the next decade, more spiral nebulae with similar broad emission lines were identified by Milton L. Humason (NGC 1275; Humason, 1932) and Nicholas U. Mayall (NGC 4151; Mayall, 1934). Later, Carl K. Seyfert discovered more of these galaxies with similar optical characteristics (Seyfert, 1943). In honour of Seyfert's discoveries, these type of galaxies are referred as "Seyfert galaxies". Further investigations have unveiled their distinctive characteristics, where the bolometric luminosity of the nuclei of Seyfert galaxies surpasses the combined luminosity of the rest of the galaxies. Therefore, the astronomy community also identifies these galaxies as "active galaxies", in general, and the bright nuclear regions as active galactic nuclei (AGN).

Over the time, the identification of AGN has increased with the use of modern telescopes covering the electromagnetic spectra from Radio to Gamma radiation. Currently about 10% of observed galaxies are known to carry AGN (e.g., Ho et al., 1997; Goulding and Alexander, 2009; Ho, 2008). In general, these galaxies are classified into two distinct classes, by studying their optical spectra: "type I" or "unobscured" AGN and "type II" or "obscured" AGN. The goal of this thesis is to investigate the obscuring medium of the obscured AGN in the local universe. In this introductory chapter, a concise overview of the thesis is provided.

1.1 AGN morphology and it's multi-wavelength emission

In this section, the physical structure of AGN is outlined, following the most standard AGN unification model of Antonucci, 1993 and Urry and Padovani, 1995. In last three decades, the unification model has evolved with more observations (e.g., Netzer, 2015,

11

Buchner et al., 2019), however the basic idea of AGN remained more or less same.

(a)   (b)
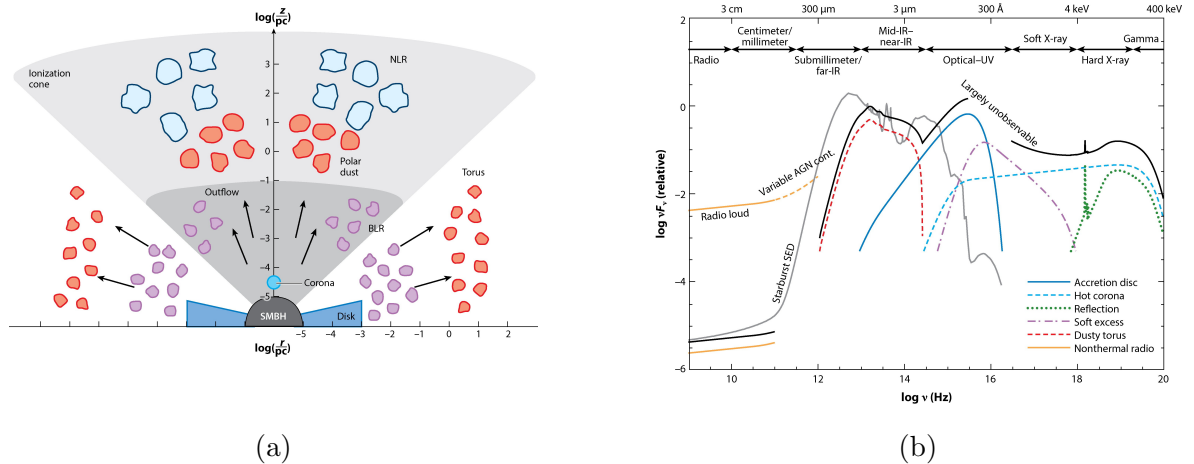
Figure 1: Schematic representation of the structure of an AGN (in left) and spectral energy distribution (in right) of unobscured AGN (black line), mentioning all the main physical components (colored lines). The Starburst spectra (grey line) is presented for comparison. The figures are taken from Hickox and Alexander, 2018.

1.1.1   Central Engine: Black Hole and Accretion Disk

The central engine is composed of the supermassive black hole (SMBH) and the accretion disk. All the primary continuum radiations originates from these regions. AGN is powered by the accreting SMBH. For a given mass of SMBH, we can calculate the characteristic length R_s or "Schwarzschild" radius:

$$R_S = \frac{2GM}{c^2} \approx 3\,\frac{M}{M_\odot}\,\text{km} \tag{1}$$

where G is the gravitational constant, M is the mass of SMBH and c is velocity of light in vacuum. The Schwarzschild radius is often refered as the "event horizon" i.e., no information can emerge from a radius smaller than R_s around the black hole. The accreting material from the host galaxy that approaches close to the SMBH, get gravitationally bounded, forming an optically thick accretion disk (scale ~ 0.01 pc from the SMBH). The accreting material lose angular momentum and spiral inwards. Due to strong viscosity within the disk, electromagnetic (EM) radiation comes out forming a shape of a multi-colored black body in the spectral energy distribution (SED; see

Figure 1b). The spectral shape of this emitted radiation depends on the temperature distribution of the disk. A higher temperature leads to a peak in the SED at the higher energy, typically in the ultra-violet (UV) part ($\lambda \sim 100 - 4000\text{Å}$) at the inner, hottest region (T$\sim 10^{4-5}$ K). As one moves to the outer disk, lower temperatures shift the spectrum peak to the optical band ($\lambda \sim 4000 - 9000\text{Å}$). The output spectrum is the composition of multiple blackbody radiation coming out of different annular disk radii. The dominant part of accretion disk SED is in the UV band, which gets absorbed by the dust and gaseous medium of the host galaxy. Observing the escaped UV radiation from accretion disk is also difficult due to absorption by the Earth's atmosphere.

$$T = 6.3 \times 10^5 \left(\frac{\dot{M}}{\dot{M}_{\text{Edd}}} \right)^{\frac{1}{4}} \left(\frac{M}{10^8 M_\odot} \right)^{-\frac{1}{4}} \left(\frac{r}{R_S} \right)^{-\frac{3}{4}} \text{K} \tag{2}$$

Here, $\dot{M}$ is mass accretion rate through the particular annulus of the accretion disk. The annulus lies at a distance r and k is the Stefan-Boltzmann constant. The rate of energy radiation from the disk, i.e., the total luminosity or "bolometric luminosity" (L_{bol}), depends on the mass accretion rate $\dot{M}$ and radiative efficiency ($\eta = 0.1$, generally) of the accretion disk:

$$L_{\text{bol}} = \eta \dot{M} c^2 \tag{3}$$

By considering the accretion of exclusively ionized Hydrogen and maintaining hydrostatic equilibrium, we can compute the maximum achievable luminosity in a system powered by accretion, called "Eddington luminosity". In this scenario, the gravitational force exerted by the SMBH is balanced by the radiation pressure from the accretion disk. Mathematically, the Eddington luminosity is expressed as:

$$L_{\text{Edd}} = \frac{4\pi GM m_p c}{\sigma_T} \approx 1.26 \times 10^{38} \frac{M}{M_\odot} \text{ erg/s} \tag{4}$$

where m_p is the mass of proton, and σ_T is the Thomson scattering cross-section for an electron. The ratio $L_{\text{bol}}/L_{\text{Edd}}$ is called "Eddington ratio" (λ_{Edd}) used to compare the accretion rates between different mass of SMBH. AGN which have $\lambda_{Edd} \sim 0.01 - 0.1$ are often considered as to have a geomterically thin accretion disk (Shakura and Sunyaev,

1973). However, when $\lambda_{Edd} < 0.01$, a geomterically thick accretion disk is thought to occur, which is radiatively inefficient (e.g., Narayan and Yi, 1994).

1.1.2 Hot Corona

An optically thin hot plasma consists of relativistic electrons, at temperature T $\sim 10^{8-9}$ K, is identified as "corona". Although the exact location, origin and structure of corona are not properly known, but they are thought to reside close to the accretion disk (about few tens of R_s; Chartas et al., 2016; Kara et al., 2016). The photons emitted from the accretion disk interacts with the high energy electrons in the corona and gets inverse-Compton scattered isotropically in all directions. These inverse-Compton photons up-scatters the disk photons, which emits in the X-ray band (E$\sim$ 0.1–300 keV), producing the powerlaw spectral shape that is observed in X-ray SED (Figure 1b). The spectral shape of this emission has the functional forms:

$$F(E) \propto E^{-\Gamma} \tag{5}$$

where $F(E)$ and E are the flux and energy of the photon, respectively. Γ is the photon index which is usually between 1.8-2.0. This emission from the corona is the primary X-ray emission. The plasma particles loose their energy after certain amount of scattering in corona, so we also need to introduce an exponential cut-off at the continuum around few hundred KeV. Throughout this thesis, I will use the term "powerlaw emission" to refer to the X-ray emission AGN emission emitted at these nuclear scales (i.e., the accretion disk and corona).

1.1.3 Torus

Beyond the accretion disk of an AGN, substantial evidence (including X-ray obscuration and mid-infrared interferometry) indicates a donut-shaped geometrically and optically thick circum-nuclear medium exits, composed of gas and dust. This medium is referred as a "torus" or "dusty torus". It exists within the gravitational influence of the SMBH, at a distance $\sim 1 - 30$ pc. The presence of such dusty torus was a fundamental element in AGN studies and classification history. Traditionally perceived as a smooth azimuthally symmetric doughnut-shaped structure, it's modeling was initiated

in Krolik and Begelman, 1988. Later it was crucial for early unification theories, including the work of Urry and Padovani, 1995, aiming to elucidate differences between Type I and Type II galaxies. Depending on it's orientation with respect to central region, along the line-of-sight (LOS), torus can obscure our direct view towards the nucleus of the active galaxy. The powerlaw emission and optical-UV emission from the nucleus is absorbed by the torus, and then re-emitted at infrared (IR) wavelength via thermal radiation, peaking in the mid-IR regime (e.g., Mullaney et al., 2011; Nenkova, Sirocky, Ivezić, and Elitzur, 2008; Polletta et al., 2000). With the advancements of observation quality in last two decades, more precise and inhomogeneous models of the obscuring torus have become necessary (Burtscher, Meisenheimer, Tristram, Jaffe, Hönig, Davies, Kishimoto, Pott, Röttgering, Schartmann, et al., 2013b; García-Burillo et al., 2021a; Nenkova et al., 2002; Nenkova, Sirocky, Ivezić, and Elitzur, 2008; Nenkova, Sirocky, Nikutta, et al., 2008; Ramos Almeida et al., 2014). Some of these models, utilizing infrared information (9.7μm Silicate line, e.g., Hatziminaoglou et al., 2015), successfully replicate the clumpiness crucial for X-ray spectral fitting (Buchner et al., 2019; Tanimoto et al., 2019a. The current widely accepted model is the clumpy torus, comprising clouds of overdense and underdense gas distribution at different location. This structure allows visibility of obscuring features even at lower torus density angles. Thus, it provides with unique absorption, scattering and thermal properties in comparison with homogeneous torus configuration.

1.1.4 Emission Line Regions

Outside the accretion disk, there is also strong evidence for two distinct regions of gas responsible for producing highly ionized emission lines by absorbing the powerlaw emission and disk emission from the central engine. These regions are called the broad line region (BLR) and the narrow line region (NLR). The BLR is located at a nearer to the SMBH ($\sim$ 0.01–1 pc; see Figure 1b), within it's gravitational influence, in between accretion disk and torus. The variability and broadness of the emission lines are formed due to the high Keplerian and thermal velocities (T$\sim 10^4$ K) of the gas in BLR, where the velocity widths of the associated emission lines stretches $\sim 10^{3-4}$ km/s (in full width at half maximum of Gaussian line profile; FWHM). In addition, because of the high gas cloud density (n$\sim 10^{9-10}$ cm^{-3}), the probability of de-excitation through collision for the ionised gas is significantly higher than through natural radiative processes.

Thus, forbidden lines[1] are not so common in this region. On the other hand, both the permitted and forbidden lines are quite common in the NLR as a result of the lower gas density (n$\sim 10^{4-5}$ cm^{-3}). NLR region resides beyond the torus, from 100 pc to few kpc (e.g., Bennert et al., 2006; Scharwächter et al., 2011). The widths of the emission lines in NLR are typically around $500 - 1000$ km/s (FWHM). On the basis of the standard unification model, the different characteristics observed in the optical spectra of type I and type II are due to the orientation of the torus along our LOS, which blocks or obscure the view of BLR in type II AGN. The spectro-polarimetric studies support the observational evidence of this theory, in which Seyfert II sources show broad permitted lines in their polarised spectra (scattered flux spectra), consistent with that seen in Seyfert I total spectra. It indicates that the nuclear regions of Seyfert II are obscured from our direct view, but can be observed if the emission is scattered into our LOS (e.g., Antonucci and Miller, 1985; Capetti et al., 1995).

1.1.5   Jets and Radio Lobes

Radio Loud AGN represents a small fraction of the AGN population, where these components are observed. Studies in the optical band suggest a fraction of radio-loud AGN $\sim 15\%$ (Kellermann et al., 1989), whereas studies at radio wavelengths suggest a much smaller fraction $< 1\%$ (Padovani, 2011). Highly collimated pair of relativistic jets close to the accretion disk can extend upto few kpc scale, from γ to radio band. A large fraction of the radio emission is powered by synchrotron radiation, produced through the interaction between high-energy charged particles and nuclear magnetic fields. Jets are thought to be produced by the spinning BH and accretion disk, coupled with the presence of magnetic fields (Blandford and Payne, 1982; Blandford and Znajek, 1977). However, the mechanism of the jet production at the smallest scale (i.e., at the core) is still not well understood at present. Radio lobes are formed in kpc to Mpc scale by the jets. These large scale structures are produced in the interaction between the jets and the Inter Galactic Medium (IGM) or Intra Cluster Medium (ICM).

---

[1]A forbidden line is produced when an electron spontaneously jumps from an upper energy state, where it can remain for a long time, to a lower energy state; having a very low transition probability. In the Earth's atmosphere, the excited atom would collide with other atoms or free electrons and lose energy quickly in the collision, without producing a photon. However, in the low densities of interstellar space, collisions are extremely rare and there is enough time for the spontaneous decay.

1.2 Obscured AGN

The AGN where the accretion disk emission is not directly observed due to the presence of material medium between the central engine and the line-of-sight of the observer, is classified as an obscured AGN or type II AGN. The obscuration is caused by the obscuring medium, composed of dust and/or gas, by absorbing and/or scattering a large fraction of incident radiation away from the observer. In this section I will briefly describe the physical nature and composition of this obscuring medium from an observational point of view, and classify the obscured AGN. Also I will provide a brief overview on the motivation to study obscured AGN, especially in the local universe.

1.2.1 Nature of obscuring medium

The term 'dust' is generally assigned to the crystal structures like carbonaceous grains and amorphous silicate grains (Draine & Lee, 1984a). It is a dominant source of obscuration at UV-IR wave-bands. On the other hand, the term 'gas' is referred to describe a broad range of gaseous states from hot plasma (ionised gas composed of electrons and protons) to cold neutral clouds of molecular compounds. The metals (i.e. elements heavier than He) in the gas are responsible for the absorption at X-ray wavelength. For majority of these obscured AGN, the obscuring medium exits within the gravitational influence of the SMBH, surrounding the accretion disk. Following the AGN unified model (Antonucci, 1993; Netzer, 2015; Urry and Padovani, 1995), this obscuring medium is geometrically and optically thick clouds of dust and molecular gas, popularly known as "torus". It is often regarded as an extension of the accretion disk in the cold outer regions, where dust grains and neutral molecular compounds can retain it's form. Apart from torus, obscuration can also come from the host galaxy i.e. dust obscured star forming regions and dust lanes. The edge-on and inclined galaxies have similar obscuring nature, especially for merging galaxies, with higher optical depth (and higher absorption) compared to face-on galaxies along the line-of-sight (Buchner and Bauer, 2017; Goulding et al., 2012). Below I explained the different obscuring nature following the above mentioned cases.

Torus: The reverberation time lags in near-IR and mid-IR measurements (e.g., Suganuma et al., 2006; Vazquez et al., 2015) and spatially resolved dust emissions from mid-IR photometry (e.g., López, 2016) suggests a compact region of the torus with

< 1 pc radius. The inner edge of the torus is predicted to follow the relation of dust sublimation radius with AGN UV luminosity $r_{in} \propto L_{UV}^{0.5}$ (Barvainis, 1987; Burtscher, Meisenheimer, Tristram, Jaffe, Hönig, Davies, Kishimoto, Pott, Röttgering, Schartmann, et al., 2013a; Suganuma et al., 2006). Analysing the mid-IR imaging (Asmus et al., 2016; García-Burillo et al., 2021b) and molecular lines (García-Burillo et al., 2016), the scale of the outer edge of the torus is estimated $\sim 10 - 30$ pc. Through X-ray observations, we can find the line-of-sight column density of the obscured AGN varies a wide range from 10^{22} cm^{-2} to 10^{25} cm^{-2} (e.g., Marchesi et al., 2018; Ricci et al., 2015a, 2016; Zhao, Marchesi, Ajello, et al., 2019 and others). Following the observations of last two decades, the AGN torus is found to be highly inhomogeneous in composition, temperature and density, portraying a clumpy structure instead of the classical smooth 'donut' shape. The radiation from the central engine passes through the optically thin gap between the optically thick clumps. This situation results in mid-infrared emission that exhibits significantly less dependence of torus orientation (Nenkova, Sirocky, Nikutta, et al., 2008; Stalevski et al., 2012). Through mid-IR spectroscopy, we find Si absorption features (9.7 and 18 micron; Draine and Lee, 1984a) which provides information on the obscuring nature. Strong Si absorption can signify obscured AGN, but not all exhibit this feature. Deep Si absorption is often linked to larger-scale structures or dust in host galaxies rather than smooth compact tori (Goulding et al., 2012), highlighting the need for diverse interpretations of the obscurer. Moreover, studying the X-ray spectra of nearby AGN through direct observations, show variability along the line-of-sight obscuration (Elvis et al., 2004; Laha et al., 2020; Markowitz et al., 2014; Risaliti et al., 2002). These variability scenarios strongly suggest the presence of moving clumps. The reflected and scattered X-ray photons, coming from the torus also carries information of the it's structure. Recent X-ray observations of many low redshift AGN suggests the presence of a thick reflector in form of a ring, close to the inner regions of torus, to produce the dominant reflection component in the X-ray spectra (Buchner et al., 2019; Pizzetti et al., 2022; Torres-Albà et al., 2023a). It suggests a large difference in composition of the inner regions, where the density varies 10 to 100 times the outer parts of torus. The covering factor or opening angle of the torus is another parameter to understand the extent of the obscuring medium. The covering factor covers a full range from $0° - 90°$, even for AGN with similar mass SMBH and luminosity (e.g., Burtscher, Meisenheimer, Tristram, Jaffe, Hönig, Davies, Kishimoto, Pott, Röttgering, Schartmann, et al., 2013a; Ramos Almeida et al., 2011). Even with this broad diversities, some trends are noticed with covering factor and different AGN

parameters, which helps in investigating the AGN nature.

Nuclear Starbursts: Far-infrared (FIR) observations at the galaxy scale reveal a weak correlation between AGN luminosity and recent star formation. However, this correlation strengthens on smaller scales (e.g., Rosario et al., 2012; Stanley et al., 2015), confirming that accreting SMBH harbor a substantial gas reservoir within the central 100 pc region, enough to fuel a starburst disk. The emergence of a starburst disk on scales less than 100 pc results from a substantial inflow of gas into a galaxy's central regions, which is often crucial for the rapid accretion onto the SMBH (Davies et al., 2009; Thompson et al., 2005). Such gas is kinematically decoupled from the galactic disk, for which the radiation pressure can expand the starburst disk along the azimuthal direction (e.g., Thompson et al., 2005, Hopkins et al., 2016). The column density distributions of these starburst disks are often identical to those observed within an obscured AGN population (Ballantyne, 2008, Hopkins et al., 2016). Compton-thick obscuration from starburst disks in small-scale structures (< 1 pc for $\sim 10^7 M_\odot$ SMBH) challenges differentiation from a torus. On the other hand, Compton-thin obscuration in larger scales (> 10 pc) may significantly contaminate the obscured AGN population (Hickox and Alexander, 2018).

Host Galaxy: The obscuration picture can be directly related to the accretion flows onto the SMBH, encompassing the entire galaxy on a cosmological scale (¿kpc). In models where SMBH-galaxy coevolution is influenced by galaxy mergers, large-scale obscuration results from gas flows onto the SMBH connected to galaxy-scale disturbances caused by merger-driven torques (Alexander and Hickox, 2012; Hopkins et al., 2008). While some studies show a strong connection between merging galaxies and hosting AGN, others suggest no relationship or a dependence on AGN luminosity (Goulding et al., 2018; Weston et al., 2017). Low-luminosity AGN in mergers exhibit a stronger correlation when selected in the IR with WISE telescope compared to optically selected AGN (Satyapal et al., 2014). Reddened quasars, representing highly obscured AGN, demonstrate a significant association with mergers and disturbances, suggesting a potential link between mergers and powerful obscured AGN (Glikman et al., 2015). FIR and submillimeter studies indicate that obscured quasars display stronger emission from cold dust, aligning with X-ray and IR-optical observations (Chen et al., 2015; Page et al., 2011). Spatial correlation studies, examining the large-scale structures of galaxies and AGN, reveal debates regarding host halo masses and clustering differences between obscured and unobscured AGN (Hickox et al., 2011). Neverthe-

less, large-scale measurements from WISE consistently show stronger clustering for the obscured population (DiPompeo et al., 2014; Donoso et al., 2012).
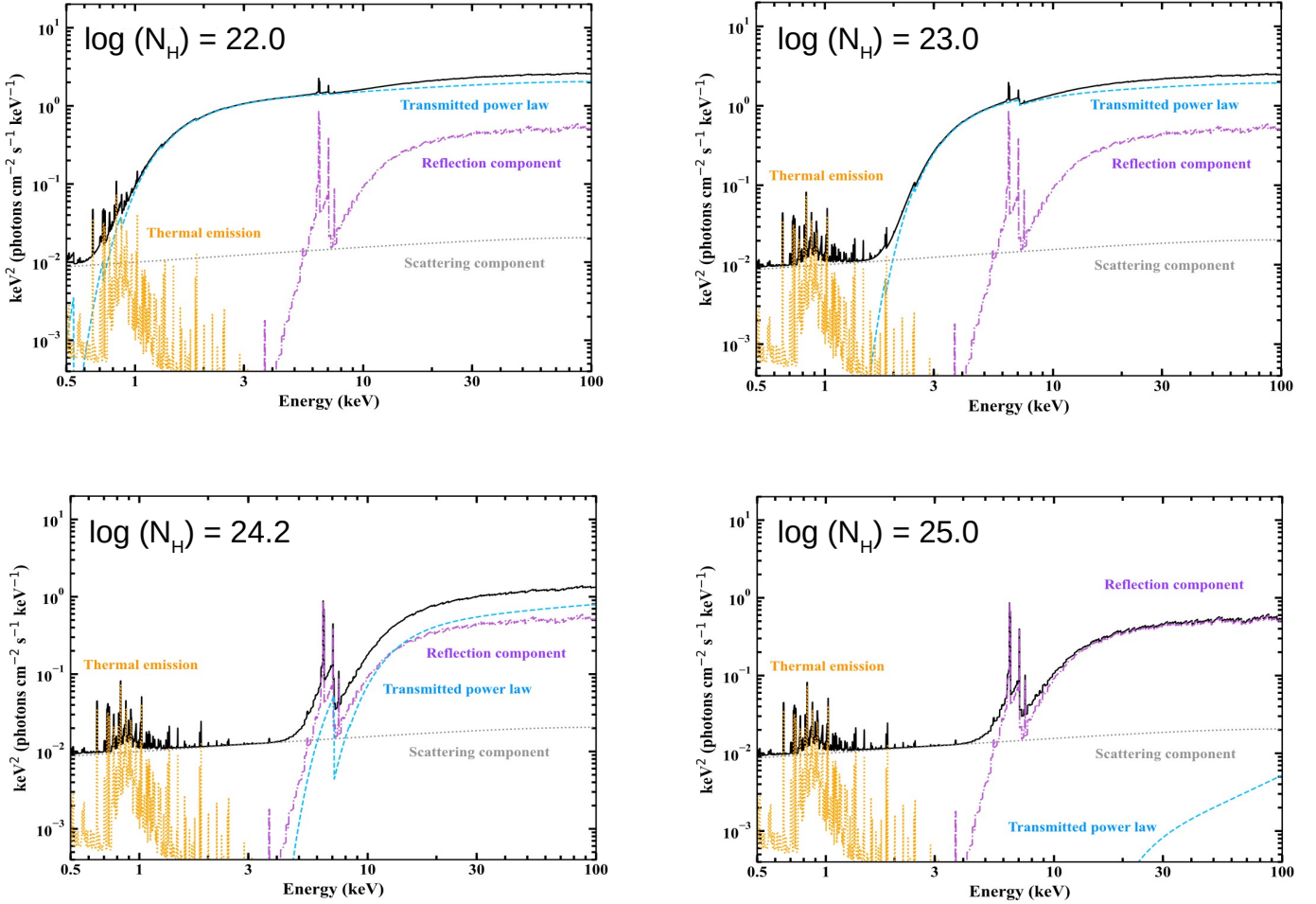
Figure 2: X-ray spectral characteristics for different line-of-sight column densities (in cm^{-2}). As column density increases along the LOS, the reflection component gets more dominated over the transmitted powerlaw. Below 10 keV, the transmitted powerlaw get completely suppressed.

1.2.2 Spectral classifications of obscured AGN

In X-rays, the obscured AGN can be classified into two categories: Compton-thick (CT) and Compton-thin (CTn) AGN. When X-ray obscurer has a line-of-sight column density equal to or larger than the inverse of Thomson scattering cross section, i.e.,

$N_{H,LOS} \geq \sigma_T \simeq 1.5 \times 10^{24}$ cm^{-2}, it is classified as CT-AGN. Otherwise, for 10^{22} cm$^{-2} < N_{H,LOS} < 1.5 \times 10^{24}$ cm^{-2}, we classify it as an obscured CTn-AGN. AGN with $N_{H,LOS} < 10^{22}$ cm^{-2} are classified as unobscured AGN, in X-rays.

In addition to the powerlaw emission originating from the corona (see Section 1.1.2), the X-ray spectra of AGN also exhibit a reflection component. The coronal emission is isotropic, so a significant part of these X-ray photons gets reflected (scattered back or absorbed and re-emitted) either from the accretion disk or inner walls of torus. It typically includes a bump at 20-30 keV (see figure 2) and a distinct iron K_α and K_β lines at 6.4 and 7.06 keV, respectively. In an X-ray SED (see Figure 2), as the LOS column density increases, the *transmitted* powerlaw emission from corona get completely suppressed below 10 keV. The fraction of powerlaw photons which experienced elastic scattering (without loosing energy or getting absorbed) before reaching the observer, are referred as the scattering component. This component dominate the soft X-rays, carrying similar Γ values. In hard X-rays (E > 10 keV), the reflection component dominates over the primary powerlaw emission. The fluorescent iron lines can be broad or narrow, depending on their origin. The line broadening is mainly due to special and general relativistic effects, as the emitting material is close to the SMBH (e.g., Fabian, 2008). Also, the broad lines are commonly observed in type I AGN, where the accretion disk come across less absorption. The obscured type II AGN, where accretion disk view is likely blocked, the line is usually narrow, thought to originate on larger scales like the inner torus walls. Thus, the equivalent width (EW) of K_α and K_β also increases with increasing obscuration (EW$\geq$ 1 keV), due to suppression of the powerlaw continuum at higher column densities. Long-term monitoring of sources with reverberating reflection and iron lines can provide insights into the origin of these features. At lower X-ray energies (E$< 2 - 3$ keV), the AGN spectrum displays another component, often referred as "soft excess". These soft thermal emissions rise due to electron scattering from an ionized zone close extended outside the central engine (Bianchi and Guainazzi, 2007; Fabian, 2012), and its modeling resembles the primary powerlaw, with similar Γ. These emissions can also arise from multiphase medium of starburst regions (Torres-Albà et al., 2018). Various explanations have been proposed for the definite origin of soft excess, but a conclusive answer still remains elusive. This thesis is focused on studying the spectral properties to understand the complex nature of torus obscuration and emission from the central engine, so we followed simple phenomenological models to fit soft excess emissions.

For a comprehensive picture of obscuration, the obscuring torus is also needed be studied in the IR band. AGN exhibit bright emissions in the mid-IR range (see Figure 1b), attributed to thermal radiation from warm-hot dust in the torus. This dust is heated by absorbing thermal optical-UV photons from the accretion disk and powerlaw emission from corona. The intensity of mid-IR emission relies on the covering factor of the dust around the accretion disk, representing the proportion of accretion disk photons absorbed by the dust. This SED peaks at $\lambda \sim 30\mu m$ (e.g., Mullaney et al., 2011; Nenkova, Sirocky, Ivezić, and Elitzur, 2008; Polletta et al., 2000) and dominates along with the dust emissions from the host galaxy. The primary spectroscopic diagnostic for assessing obscuration in AGN is the Si-based dust absorption feature at 9.7 and 18 μm (e.g., Draine and Lee, 1984b). This feature, caused by silicon dust grains, indicates the amount of obscuration by the mid-IR emitting region of the torus. Si absorption is prevalent in obscured AGN, while unobscured type I AGN typically exhibit Si emission features. Unlike the UV-near-IR range, mid-IR wavelengths experience low optical depth, minimizing suppression by obscuring dust. These characteristics make mid-IR observations crucial for studying AGN properties along side with X-rays, providing insights into the geometry and composition of the obscuring material surrounding the accretion disk.

1.2.3 Cosmic X-ray background problem

In the early 1960s, it was discovered that the universe showered X-ray radiation almost isotropically (Giacconi et al., 1962). These X-ray photons are commonly known as the cosmic X-ray background (CXB) radiation. Around similar time, the more famous Cosmic Microwave Background (CMB, Penzias and Wilson, 1965) was discovered. Unlike CMB, the the source of CXB radiations were not very well understood at that time, but it became clear that they had extra-galactic origin. With the deep field surveys of modern grazing incidence telescopes like Chandra and XMM-Newton (Alexander et al., 2003; Jansen et al., 2001), the CXB has been resolved into discrete point sources (Hickox and Markevitch, 2006; Xue et al., 2012). Both these telescopes surveyed the sky for more than 20 years, especially Chandra ultra-deep surveys have resolved about $90 - 95\%$ of the CXB at E< 10 keV. But due to the limitations of soft X-ray energies, these observations also suffers significant absorption bias, when obscured by gas and dust along the LOS. Only a fraction of the intrinsic photons reach us, while most of them get scattered or photo-absorbed by the obscuring media. Therefore, despite we
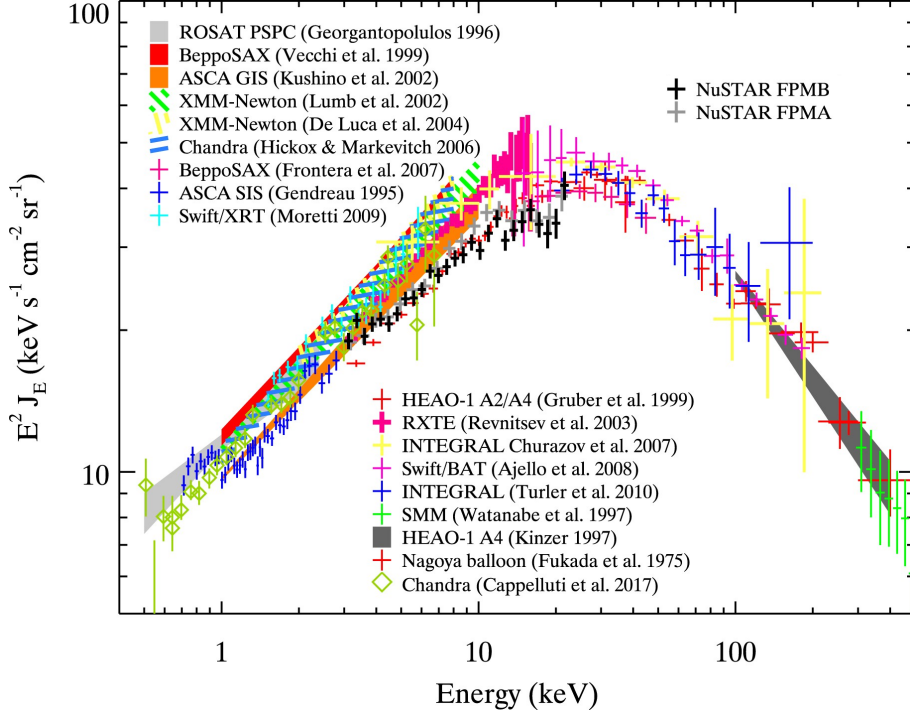
Figure 3: Cosmic X-ray Background Radiation from 0.4-500 keV from Rossland et al., 2023.

progressed in understanding the CXB, thanks to telescopes like Chandra and XMM-Newton, the large majority of the CXB above 10 keV remains unresolved. Due to the technological difficulties in focusing hard X-rays, only coded mask instruments like Swift-BAT and INTEGRAL were employed to complete the wide survey of the hard X-ray sky. Deep surveys with these instruments were able to resolve up to few percent of the total CXB above 10 keV (Ajello et al., 2008; Koss et al., 2016; Ricci et al., 2015b). It was found that most of the CXB radiation from 1 keV to 100 keV is the result of AGN emission (e.g, Gilli et al., 2007). The launch of Nuclear Spectroscopic Telescope Array in 2012 (Harrison et al., 2013), the first hard X-ray grazing incidence telescope operating between 3 keV and 79 keV, opened a new window for X-ray astronomy.

With the observations of all other X-ray telescopes, in last 60 years, the CXB is found to have peaked ∼ 30 keV (see Figure 3). The contribution of unobscured AGN to the CXB at E<10 keV is almost completely resolved into point-like sources. At present, only ∼ 30% CXB has been resolved at it's peak, thanks to several NuSTAR surveys

(e.g., Aird et al., 2015; Harrison et al., 2016). Meanwhile the detection of obscured AGN ($N_H > 10^{22}$ cm^{-2}), which are responsible for a significant fraction ($\sim 40\%$ at the peak) of the CXB emission, is found to be challenging. CT-AGN population produces almost $\sim 15 - 20\%$ of CXB at it's peak (Ananna et al., 2019; Gilli et al., 2007). In local universe (for redshift $z < 0.1$), the observed fraction of CT-AGN is $\sim 5 - 10\%$ (Vasudevan et al., 2013; Ricci et al., 2015b; Torres-Albà et al., 2021). However, CXB population synthesis model predicts this CT-AGN fraction should be $\sim 20 - 50\%$ (Ueda et al., 2014; Ananna et al., 2019) to properly fit the CXB spectra. Thus, there is a significant gap between the observational information and the model predictions, which is still an open question in the astronomy community. This low fraction seems to be due to the observational bias in the detection of obscured CT-AGN in X-rays (e.g., Burlon et al., 2011; Ricci et al., 2015b). At higher redshift, the missing fraction decreases from 70% to $10 - 20\%$ and the contribution of AGN with higher luminosity is needed. A population synthesis model is generally described by the number density of AGN as a function of their luminosity and redshift (i.e., X-ray luminosity function or XLF). In Ueda et al., 2003, the model introduced three components: AGN template spectrum as a function of column density and X-ray luminosity ($L_{2-10\mathrm{keV}}$), space density distribution as a function of $L_{2-10\mathrm{keV}}$ and an absorption function of how this space density is distributed in column density bins. Later models used advanced statistical tools and different parametric approach (e.g., Ueda et al., 2014, Buchner et al., 2015, Aird et al., 2015, Ananna et al., 2019), within a same framework of observed XLF. However, the complex obscuring and emission properties of the obscuring medium in CT-AGN is not properly taken into account on these models, which might lead to an over-estimation also. Therefore, a complete census of obscured AGN population in local universe is needed to fill the gap and overcome the observational bias using multi-wavelength techniques; photometric and spectroscopic studies in the mid-Infrared and X-ray surveys (e.g., Comastri et al., 2015).

2 Methodology

In this section, I have discussed briefly about the X-ray telescopes, whose observation I have used for my analysis. I have also discussed the several spectral analytical methods and models that I have used to classify the obscured AGN.

2.1 X-ray observations
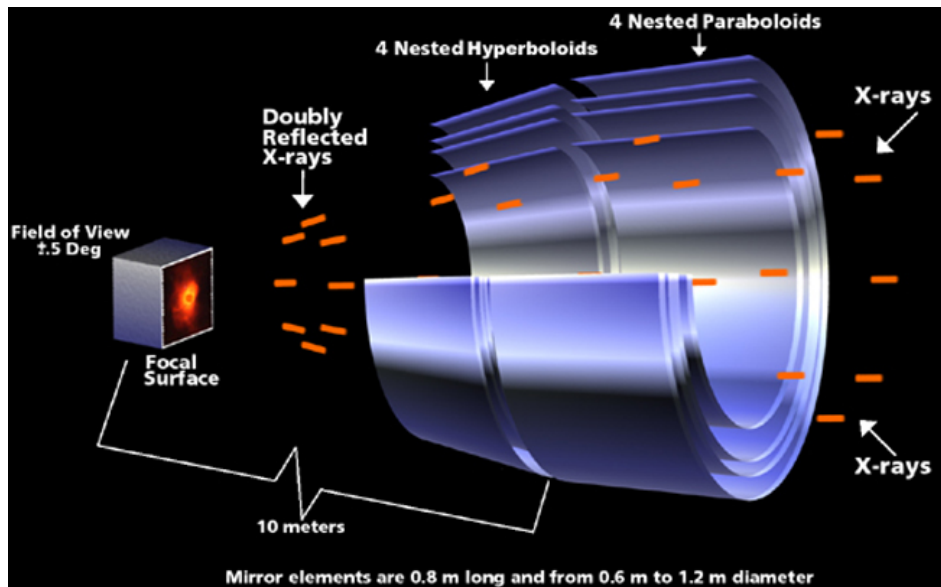
Figure 4: Schematic diagram of the grazing incidence telescope in *Chandra*. It illustrates the design and functioning of the High Resolution Mirror Assembly (HRMA) inside *Chandra*. The X-ray photons gets reflected, instead of getting absorbed, by the mirrors, making very small grazing angles before reaching the focal surface. Image is provided by Chandra X-ray Observatory, NASA.

All the X-ray telescopes are space telescopes because Earth's atmosphere absorbs all the cosmic X-rays. The ability to focus X-ray photons was only developed about 70 years ago by Hans Wolter, using reflective optics. The unique challenge in focusing X-ray photons arises from their high penetrating power. To address this issue, some X-ray telescopes use "grazing incidence" mirrors with small grazing angles. These mirrors are aligned almost parallel to the incident X-ray emission to increase the probability of reflection rather than absorption. The small photon collecting area is mitigated by

nesting multiple mirror shells together. This approach enhances the effective area for collecting X-ray photons.

The mirrors in X-ray telescopes typically consist of two reflecting surfaces (see Figure 4): a paraboloid (primary mirror) and a hyperboloid (secondary mirror). While a paraboloid alone effectively focuses X-ray photons to a point, it distorts off-axis objects. To address this, a hyperboloid surface is added as a secondary mirror. The combination of paraboloid and hyperboloid optics is called Wolter Type I mirror design. This design, known for its short focal length, has been widely used, including in the pioneering Einstein observatory (`HEAO-2`) and modern telescopes like *NuSTAR*, *Chandra*, and XMM-*Newton*. Detectors at the focal point record detailed information about the incident X-ray photons, facilitated by solid-state detectors or charge coupled devices (CCD), allowing simultaneous image and spectroscopic data collection. Unlike optical telescopes, X-ray detectors directly measure the energy of individual photons, enabling precise counting and recording of their properties. However, these detectors may also register non-X-ray events and particle flares. These issues are addressed through techniques like identifying "good time intervals" (the period when the flare is insignificant). These events can also be filtered out during the data processing steps.
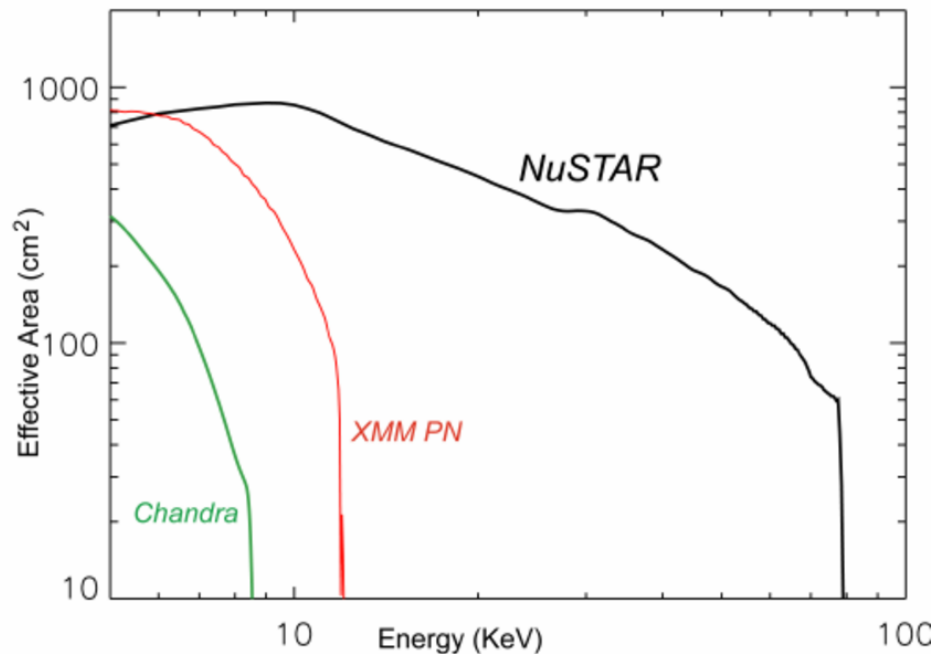
Figure 5: Effective area of *Chandra*, XMM-*Newton* and *NuSTAR* along the energy band. The figure is adopted from Harrison et al., 2010.

26

This section provides an overview of the X-ray telescopes that I have primarily used in our thesis, focusing on the high (*NuSTAR*) and low energy (*Chandra* and XMM-*Newton*) X-ray observatories. The high-energy data (E> 10 keV) are crucial for tracing primary emissions from CT-AGN through obscuring layers, while low-energy observations (E< 10 keV) are essential for probing fluorescence iron line emissions and diffuse thermal emissions. The combination of both datasets enables the creation of a broadband X-ray spectrum, allowing precise measurements of the obscuring properties.

2.1.1 NuSTAR
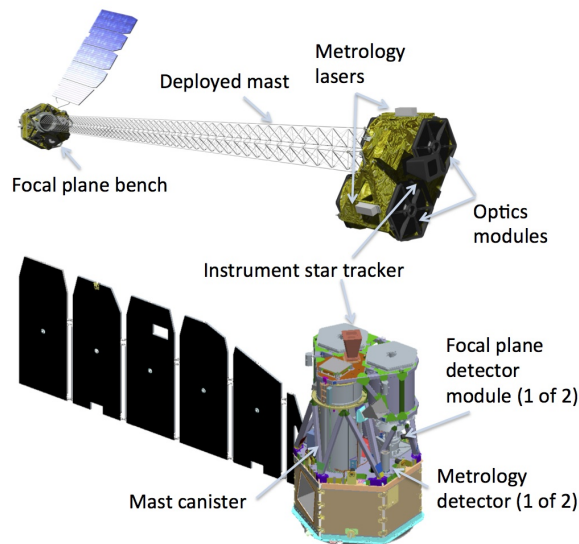
Figure 6: A schematic design of *NuSTAR* telescope. Its features include two co-aligned grazing incidence X-ray telescopes. These telescopes are equipped with state-of-the-art CdZnTe pixel detectors, allowing *NuSTAR* to capture high-energy X-rays in the 3–79 keV range with exceptional sensitivity and spatial resolution. (Image credit: NASA)

NuSTAR marks a significant advancement in hard X-ray astronomy as the first focusing hard X-ray telescope (Harrison et al., 2013), covering the energy range of 3 to 79 keV. It carries eight Cadmium-Zinc-Telluride detectors in a 2×2 array of 32×32 pixel chips, divided into two focal plane modules (FPM) as: FPMA and FPMB. It outlines

the extendable mast deployed in an orbit to achieve a ~ 10 meters focal length. To enhance reflectivity of the high energy incident photons, each of these optical modules adopt the Wolter-I conical approximation design. It carry 133 shells of mirrors coated with layers of Tungsten/Silicon in outer the shells and Platinum/Carbon in the inner shells. The platinum coating starts absorbing X-ray photons for E> 79 keV, for which NuSTAR's energy sensitivity is limited upto that limit. These focal planes are shielded by Cesium-Iodide (CsI) crystals, which surrounds the detector. These crystal shields collect high energy photons and cosmic rays which cross the focal plane from directions other than the optical axis. The sensitivity of NuSTAR is also approximately 100 times compared to coded-mask instruments where the detection of the events are based on the shadows instead of direct imaging. Thus a better spatial accuracy is achieved, with a point spread function (PSF) of FWHM at 18" and a half-power diameter (HPD) of 58". The only drawback has been the contamination of high background affecting deep observations, caused by the metallic mast when fully deployed in orbit, preventing the optics to get perfectly screened by the leaking photons.

One of the primary objectives of NuSTAR is to investigate both local and high redshift AGN. The higher angular resolution and better sensitivity in that energy band helps identifying the CXB contributors, especially at it's peak $\sim 20-30$ keV. It's high-energy bandpass minimizes biases related to absorption, unlike soft X-ray instruments. Thus, it provides excellent coverage for detecting characteristic signatures of obscured AGN like CT-AGN. Properties like fluorescent iron lines at 6.4 keV and 7.06 keV, Compton reflection hump $\sim 20-30$ keV, help to characterise the spectral shape of CT-AGN and CTn-AGN in the local Universe (e.g., Boorman et al., 2016; Marchesi, Ajello, Zhao, Marcotulli, et al., 2019; Zhao, Marchesi, and Ajello, 2019). Moreover, it also helps studying the X-ray variable and *changing-look* obscured AGN candidates.

For the data processing and reduction of NuSTAR data, I have used the NuSTAR Data Analysis Software (nustardas) within Heasoft package, incorporating the calibration database (CALDB). The data processing procedures are followed according to the NuSTAR data analysis guide. Here, I mention briefly how I proceeded, further details are provided in the following chapters of this thesis. The process includes generating calibrated and cleaned event files ("level 2 data") from telemetry data ("level 1" data) through the *nupipeline* script. It incorporates metrology processing, altitude correction, bad and hot pixel flagging, event reconstruction, and grade assignment. Calibrated event files undergo screening for bad time intervals, and subsequent steps

involve extraction of spectra (source and background) and response files using the *nuproducts* task. The final net spectrum, obtained by subtracting background emission from the source spectrum. It is generated by multiplying it with response files that include ancillary response function (ARF) and redistribution matrix file (RMF). The final spectrum is then binned into counts per bin using the *grppha* task.

2.1.2 XMM-Newton
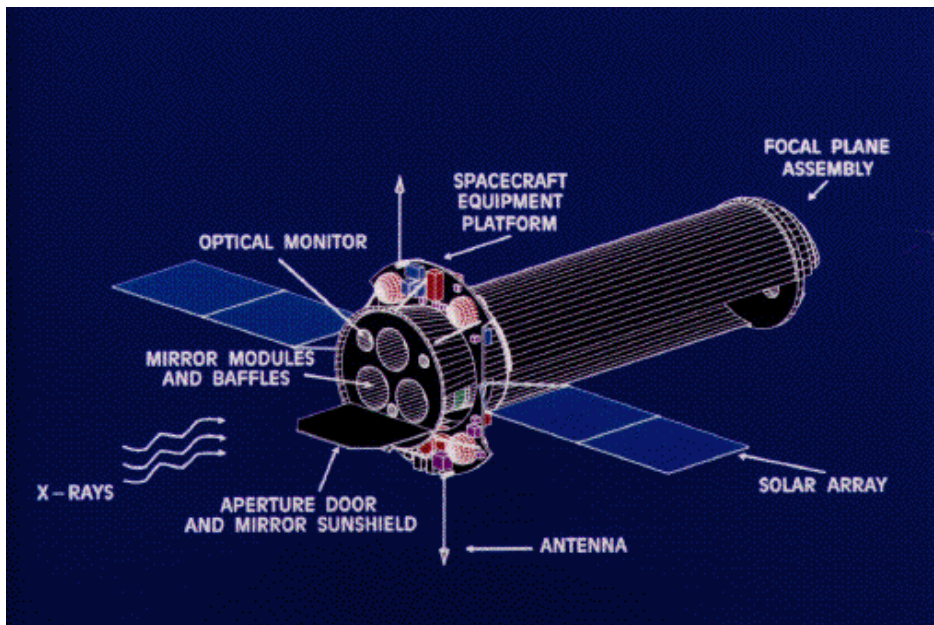
Figure 7: The schematic design of XMM-*Newton* observatory. It is equipped with three high-throughput X-ray telescopes, XMM-Newton utilizes reflection grating spectrometers and imaging cameras for simultaneous observations in different X-ray energy bands. Its innovative design enables astronomers to conduct comprehensive studies of extragalactic X-ray sources below 10 keV. (Image credit: NASA)

The X-ray Multi-Mirror Mission[2] (XMM-Newton) was launched in 1999. It was of the pivotal components of the European Space Agency's (ESA) Horizon 2000 Science program. It is equipped with three co-aligned X-ray telescopes, each adopting the Wolter-I design. XMM-Newton boasts 58 nested gold-coated mirrors with a 7.5 meters focal length. These mirrors has a photon collecting area of approximately 4500 cm^2 at

---

[2]https://www.cosmos.esa.int/web/xmm-newton

1 keV, with a diameter 70 cm. The telescope is sensitive within the energy range 0.1 keV to 12 keV, with a spatial resolution of 6" at FWHM.

XMM-Newton incorporates three main science instrument: the European Photon Imaging Cameras (EPIC), the Reflection Grating Spectrometers (RGS), and the Optical Monitor (OM). These instruments allow for simultaneous X-ray and optical/UV observations. In this thesis, I worked only with EPIC instrument, so I will only focus on it. The EPIC consists of three detecting instruments: a "pn"-camera (PN) and two identical metal-oxide-semiconductor (MOS) cameras (MOS1 and MOS2). The PN camera features 12 arrays of back-illuminated (BI) CCD, each with 64×200 pixels, making it more sensitive and has a higher effective area (1227 cm^2 at 1 keV) compared to the MOS cameras (922 cm^2 at 1 keV). The MOS cameras consist of 7 arrays of front-illuminated (FI) CCDs, each having 600×600 pixels. All three cameras offer a field of view of approximately $30' \times 30'$ and are employed simultaneously during observations. These EPIC cameras are optimized for both high-resolution imaging and moderate-resolution spectroscopy (about 50 eV at 1 keV).

The data processing and data reduction of XMM-Newton data is done by utilizing XMM-Newton's Science Analysis System (SAS). The adopted data reduction approach is briefly outlined, with more comprehensive details available in the XMM-Newton's user handbook[3]. For each observation, we are provided with the Observation Data Files (ODF), containing uncalibrated files. The ODF is processed by the Processing Pipeline Subsystem (PPS), generating scientific products like event and source files, net source spectra and source light curves. These PPS products are accessible to the community after the completion of the observation. Subsequently, the event files from PPS are reprocessed to incorporate updated calibration. Using the *evselect task*, the event files for each EPIC camera are then screened, implementing standard filter flags to account for factors like hot pixels, low pulse height, and undesirable "patterns" (with ranges of 0–12, typically excluding pattern > 4 and > 12 for PN and MOS, respectively). Additionally, the event files undergo manual filtering in case of bad time intervals associated with particle flaring. They are identified by scrutinizing the light curve, after binning the count rates over a given time interval. Using the *tabgtigen* task, the event files are filtered by eliminating the flare contamination. The source and background spectra for each detector are then extracted from the cleaned event

---

[3]https://xmm-tools.cosmos.esa.int/external/xmmusersupport/documentation/uhb/XMMUHB.html

files, employing the *evselect* task and filtered for bad pixels using the *backscale* task. The creation of ARF and RMF files is executed through *arfgen* and *rmfgen* tasks, respectively. Finally, all net spectra are binned using the *grppha* task, and XMM-Newton's count images at various energy bands are generated with the *evselect* task. The combination of XMM-Newton's capabilities supplements NuSTAR data, allowing not only comprehensive spectral analysis but also the resolution and identification of X-ray sources in heavily obscured AGN.

2.1.3 Chandra
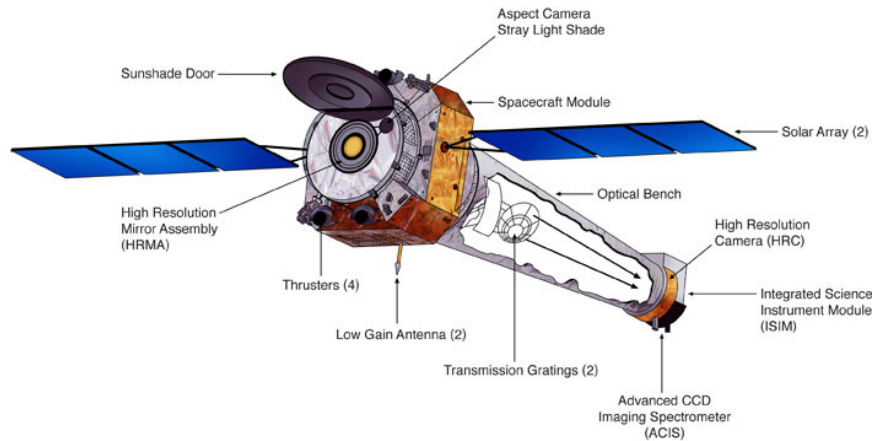
Figure 8: The schematic design of Chandra X-ray Observatory. It features a high-resolution X-ray telescope, with its four sets of nested mirrors. The Advanced CCD Imaging Spectrometer (ACIS) and High-Resolution Camera (HRC) instruments, part of Chandra's instrumentation, allows astronomers to explore extra-galactic objects with exceptional sensitivity. (Image credit: NASA)

The Chandra X-ray Observatory (CXO) was launched in 1999 as part of NASA's flagship mission. With its advanced CCD imaging spectrometer (ACIS) and high-resolution camera (HRC), along with low and high-energy transmission gratings (LETG and HETG), Chandra utilizes the High-Resolution Mirror Assembly (HRMA) adopting the Wolter-I mirror design for focusing X-ray photons. Chandra's optical prowess lies in its HRMA, comprising a set of four grazing incidence mirrors coated with iridium (Ir) to enhance reflectivity, having a focal length of 10 metres. These mirrors are extremely smooth and clean, perfectly aligned making a very precise optical surface. This provides

excellent X-ray resolution of Chandra, in which the majority of the incident photons can be focused at 0.5" radius along the on-axis. I used only ACIS data for my thesis, as the precise spectral resolution and sensitivity in the energy range 0.1–10 keV range ACIS an invaluable tool for the soft X-ray spectra. So, I will not go into the technical details of the other detectors. But in Chandra's proposer's observatory guide, further details on the observatory and other instruments can be found.

Chandra's focal plane instruments include ACIS and HRC, along with LETG and HETG for high-resolution spectroscopy. ACIS consists of two arrays of CCD: ACIS-I (FI; 2×2 array at $16' \times 16'$) optimized for wide-field imaging and ACIS-S (FI and BI; 1×6) usable with the HETG transmission grating for high-resolution spectroscopy. ACIS allows for high-resolution imaging and moderate-spectroscopic and time resolution. Two CCD (ACIS-S1 and S3) are BI, enhancing sensitivity with higher quantum efficiency, by exposing the photo-sensitive region to the incoming photons. The rest are FI CCD. The aimpoint of ACIS-S is ACIS-S3 CCD, which carries a small field of view ($8.3' \times 8.3'$) with better spectral resolution (100 ev at 1 keV) among the ACIS system, without any use of grating. Similar to XMM-Newton, Chandra with NuSTAR also gives a better window to understand the spectral nature of the X-ray emission from the obscured AGN.

2.2   X-ray torus models

In this chapter, I briefly describe the procedure of X-ray spectral fitting using the different X-ray torus models. These models will often be referred as "physically motivated models" throughout this thesis, since they are composed of more physical and detailed structural analysis of the torus.

2.2.1   XSPEC Spectral Fitting

The X-ray torus models are used through 'XSPEC' software (Arnaud, 1996), which is a command-driven, interactive, X-ray spectral-fitting program. The spectrometer of the telescopes captures photons, which is stored as 'photon counts' (C) within it's instrument channels (I). This 'observed spectrum' can be related with the 'true spectrum' using the equation:

$$C(I) = \int f(E)R(I,E)dE \tag{6}$$

Here, $R(I,E)$ is the instrumental response which is proportional to the probability of incoming photon energy E through channel I. Therefore, the true spectrum $f(E)$ can be derived by inverting the equation from the observed spectrum, given as $C(I)$. Each observed spectrum contains two files- data spectrum file (or source file) and background file. XSPEC must also know the specific characteristics of the detector instruments, from $R(I,E)$. For that, this continuous function is converted to a discrete function by using a response matrix, with the energy ranges E_J:

$$R_D(I,J) = \frac{\int_{E_{J-1}}^{E_J} R(I,E)dE}{E_J - E_{J-1}} \tag{7}$$

Here, $R_D(I,J)$ is the response matrix. XSPEC reads both the energy and the response matrix from a response file in a compressed format. It use an auxillary response file (ARF) which contains an array over the energy range as $A_D(J)$, multiplied as $A_D(J) \times R_D(I,J)$. This array is designed to represent the efficiency of the detector with the response file, representing a normalized Redistribution Matrix Function or RMF. For spectral fitting over the data points of the source, XSPEC needs these four file to compile: source file, background file, ARF and RMF files.

2.2.2 Mytorus

The MYTorus model (Murphy and Yaqoob, 2009; Yaqoob, 2012) was developed to be used in the XSPEC environment as a combination of additive and multiplicative tables, which represent different components of X-ray emission from the AGN. MYTorus models the heavily obscured AGN spectra taking into account the direct powerlaw component as MYTZ, absorbed and scattered component as MYTS, and the fluorescent Fe K_α and K_β lines as MYTL. It is one first physically motivated models, which used a doughnut shaped torus, with uniform gas distribution. The evolution of the

radiative transfer through the torus is based on the a Monte Carlo code that calculate grids of Green's functions.

Every simulated photon is traced in its interaction with the reprocessing medium (torus). If the photon escapes the absorbing structure, it is flagged as continuum or as line photon, with a specific energy and direction of propagation.

2.2.3 Physical Geometry
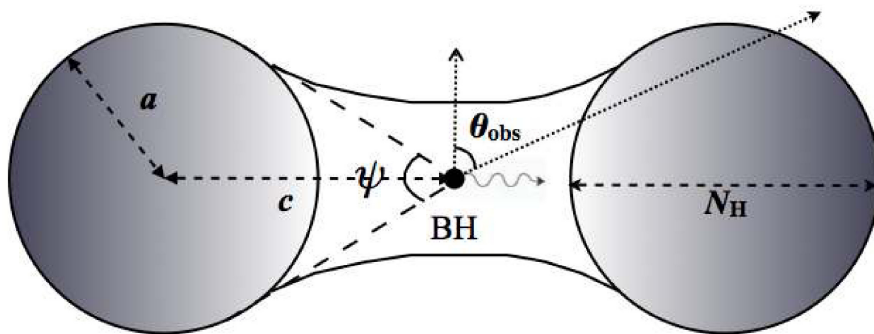
Figure 9: `MYTorus` model adopted from Murphy and Yaqoob, 2009.

`MYTorus` can be used in two different configurations: *coupled* and the *decoupled*. In coupled mode, the parameters such as the column density, inclination angle of the three components (MYTZ, MYTS and MYTL) are tied together. But for our thesis, we have used only the *decoupled* configuration. In this configuration, the component MYTZ is kept free and MYTS is tied with the MYTL, considering both the reflected and line components originates from the similar region. `MYTorus` simulates the interaction between input spectrum photons with the circumnuclear obscuring medium, maintaining a classical doughnut shaped azimuthally symmetric structure. The torus half opening angle represents the fraction of the sky as seen from the center, is defined as $\alpha = [(\pi - \psi)/2] = 60°$, corresponding to a covering factor $C_{TOR} = 0.5$. considering $N_{H,LOS}$ as the column density of the torus, it is calculated as:

$$N_{H,\text{LOS}} = N_H \left[1 - \left(\frac{c}{a} \right)^2 \cos^2 \theta_{obs} \right] \tag{8}$$

Here, N_H is the equatorial column density, the distance from the BH to the center of the torus section is c, and a is the radius of the section (see Figure 9).

2.2.4   Model Components

The MYTZ component is often called the zeroth order component or direct component, as the photons are escaping the torus without being absorbed or scattered. The component MYTS is the scattered or reprocessed continuum, which represents the photons escaping the medium after being scattered one or more times. The scattering probability depends on the absorption and scattering cross-sections through the single-scattering albedo s = $\sigma_s/(\sigma_s + \sigma_a)$, where σ_s and σ_a are the scattering and absorption cross-sections, respectively. The photon's energy get reduced after this interaction, producing the feature of a hump around 20-30 keV (for local CT-AGN). The component MYTL originates close to the inner side of the torus, producing fluorescent iron lines. The *decoupled* configuration is done by fixing the inclination angle of MYTZ at 90° and untie the MYTS parameters from it, making MYTZ a pure LOS component. This adjustment designates the direct continuum column density as representing the LOS column density, while the MYTS column density signifies the "global average" column density arriving from the scattered medium of torus. The homogeneity (or clumpiness) of the torus can me approximated by taking the ratio of column densities of MYTS vs MYTZ. If the ratio is close to 1, it's homogeneous, if it's far from 1, it indicates the scattering region is either under-dense or over-dense than the LOS column density. Following the approach of Yaqoob et al., 2015, the inclination angle can be set for the scattered and fluorescent line components to either $\theta_{S=L} = 90°$ or $\theta_{S=L} = 0°$, replicating an edge-on and face-on geometry respectively. In XSPEC, the configurations are written as follows:

$$
\begin{aligned}
\text{Model MyTorus}_{\text{edge−on}} = const \ * \ phabs \ * \\
(zpow * MYTZ + A_{S,90} * MYTS + A_{L,90} * MYTL+ \\
f_s * zpow),
\end{aligned}
\tag{9}
$$

$$
\begin{aligned}
\text{Model MyTorus}_{\text{face−on}} = const \ * \ phabs \ * \\
(zpow * MYTZ + A_{S,0} * MYTS + A_{L,0} * MYTL+ \\
f_s * zpow).
\end{aligned}
\tag{10}
$$

Here, the galactic absorption is given as *const * phabs*. The A_S and A_L are coefficients for corresponding `MYTorus` components. f_s gives the fraction of the scattered component, without getting absorbed.

2.2.5 Borus02

The BORUS (Baloković et al., 2018) is a Monte Carlo radiative transfer code, that can be used in operating arbitrary 3-D spaces to represent matter density, by applying mathematical functions or data cubes. This allows the calculation of output spectra for the complex matter distributions, anticipated in hydrodynamical simulations around the torus environment. However, for fitting limited-quality X-ray data, these structures are simplified and parameterized. The strength of this model is that it fits the spectral data with having free parameters such as average column density of the torus and its covering factor. This was not possible to deduce even in the decoupled configuration of `MYTorus`. Moreover, the "short" (days, week) timescales variability of the NH,los (e.g., Risaliti et al. 2002; Ricci et al. 2016) is due to the movement of clouds through the LOS. Whereas, the average column density vary on much longer (year) timescales, represents a more reliable parameter to characterize the optical thickness of the torus.

Physical Geometry

This spectral template adopts a toroidal geometry similar to Brightman and Nandra, 2011 (also called `BNtorus`), involving a uniform-density sphere with bi-conical cutouts. This simplification represents a smoothed distribution of individual clouds forming the torus, assuming these clouds are much smaller than the torus itself and occupy most of its volume. The half-opening angle of the polar cutouts (θ_{tor}) is measured from the symmetry axis towards the equator, ranging from zero (full covering) to $84°$ ($\sim 10\%$ covering). The gas is assumed to be uniformly distributed with solar elemental abundances, except for iron, which is a variable parameter. The LOS component (absorbed powerlaw continuum) can possess a different column density than the average column density of the torus. It allows the movement of clouds and variability along the LOS. The average column density is calculated from the reflected continuum, taking into
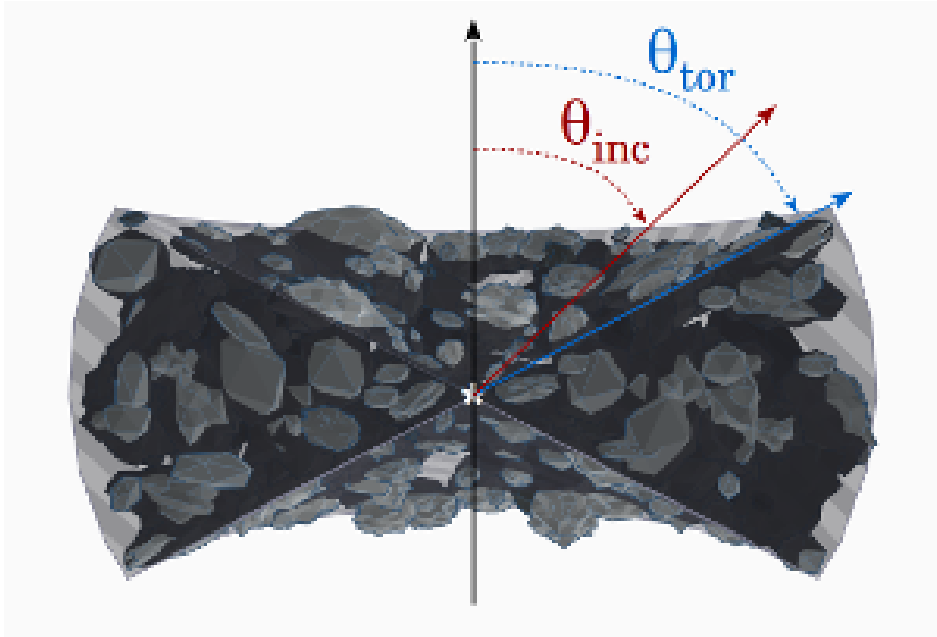
Figure 10: `borus02` model adopted from Baloković et al., 2018.

account the fluorescent line components. Although the geometry of BORUS aligns with Brightman and Nandra, 2011, the enhanced calculation is more detailed and flexible such as, additional chemical elements included, E_{cut} extending to higher energies, relative abundances of iron A_{Fe}.

Model Components

It calculates Green's functions for initial photon energies ranging from 1 keV to 1 MeV. Post-processing involves convolving these functions with a parameterized intrinsic continuum. The simulated medium is assumed to be cold, neutral, and static, and photons propagate until absorption without fluorescent re-emission or escape. Probabilities of photoelectric absorption and Compton scattering at each step are computed based on: NIST/ XCOM[4] elemental abundances from Anders and Grevesse, 1989, and the Klein–Nishina scattering cross-section formula. For absorbed photons, fluorescent emissions, including $K_{\alpha1}$, $K_{\alpha2}$, and K_β lines up to zinc (atomic number < 31), are generated. This comprehensive approach ensures a detailed representation of X-ray interactions within the simulated medium.

---

[4]https://www.nist.gov/pml/xcom-photon-cross-sections-database

This model is composed of four components: (a) galactic absorption ($const * phabs$), (b) `borus02` itself, which is a reprocessed component including Compton-scattered + fluorescent line component with fits file: `borus02_v170323a.fits`, (c) $zphabs * cabs$ to include LOS absorption with Compton scattering through the obscuring clouds; with this component we multiply a $cutoffpl_1$ to take into account the primary power-law continuum, and (d) finally another $cutoffpl_2$ component is included separately with f_s to include a scattered unabsorbed continuum. In our analysis using `XSPEC`, we used the following model configuration:

$$
\begin{aligned}
\text{Model borus02} = C_{Ins} * phabs * (atable\{\texttt{borus02\_v170323a.fits}\} + zphabs \\
* cabs * cutoffpl_1 + f_s * cutoffpl_2)
\end{aligned}
\tag{11}
$$

The `borus02_v170323a.fits` file is composed of eight parameters: photon index, high energy cut-off, torus column density, torus covering factor, inclination angle, relative abundance of iron, redshift and normalization of the intrinsic spectrum (at 1 keV). The $cutoffpl$ is a powerlaw with exponential cut-off, incorporated within `XSPEC`.

2.2.6 XClumpy

CLUMPY model was already introduced in IR-modeling (Nenkova, Sirocky, Ivezić, and Elitzur, 2008; Nenkova, Sirocky, Nikutta, et al., 2008), which utilizes a powerlaw distribution in the radial direction and a normal distribution in the elevation direction to construct spectral models for clumpy tori. This model has been successfully applied to interpret the infrared spectra of nearby AGNs, as highlighted in Ramos Almeida and Ricci, 2017 and associated references. Stalevski et al., 2012 presented an alternative approach, offering insights into infrared spectra from clumpy tori with a two-phase medium and slightly different geometry compared to the CLUMPY model. More recently, in the domain of X-ray spectral modeling from clumpy tori, Liu and Li, 2014 introduced the `CTorus` model, utilizing the Geant4 library, with a clump distribution confined in a partial sphere. Furui et al., 2016 contributed to this endeavor with the Furui model, incorporating a bagel-like geometry through the Monte Carlo simulation for astrophysics and cosmology framework (MONACO: Odaka et al., 2011, 2016), optimizing for astrophysical applications and considering Compton down-scattering of

fluorescence lines. These advancements contribute to a comprehensive understanding of the diverse torus structures in different wavelengths. X-ray clumpy torus model (XCLUMPY) is constructed in Tanimoto et al., 2019b, following these approaches.
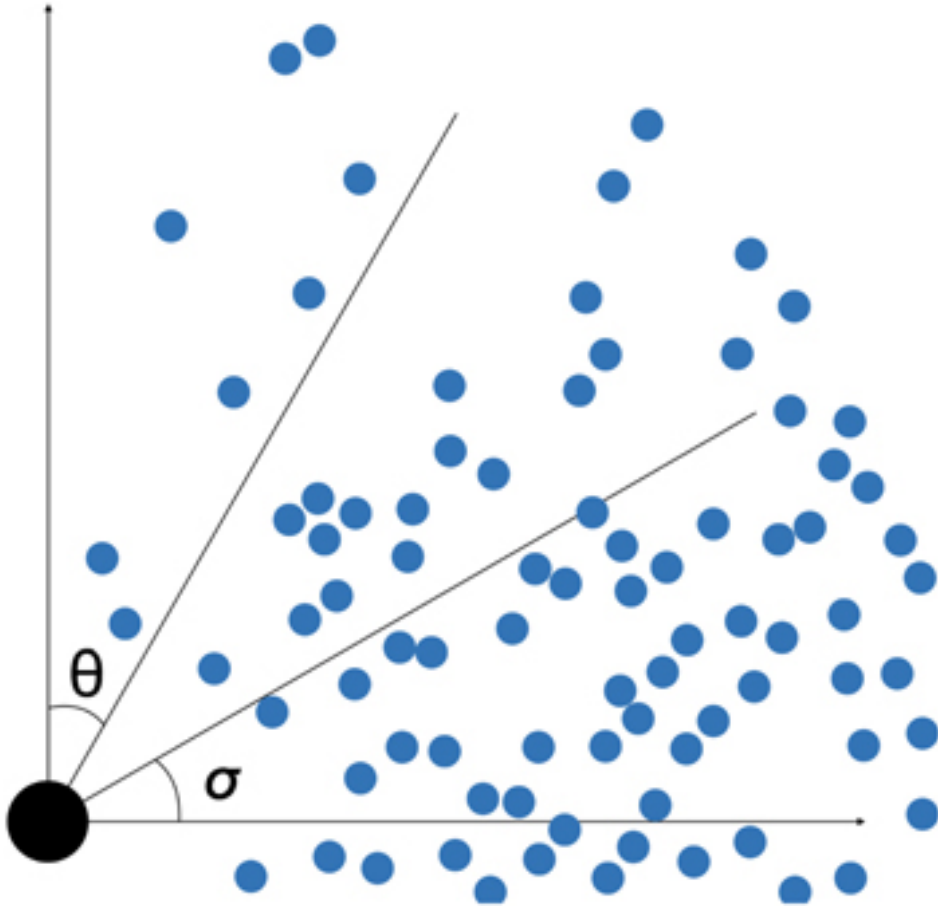
Figure 11: Schematic representation of `XCLUMPY` model adopted from Tanimoto et al., 2019b.

Physical Geometry

In XCLUMPY, the torus is also not a continuous medium but is instead comprised of randomly distributed clumps, following a specified number density function. For simplicity, each clump is modeled as a sphere with a radius denoted by R_c with a uniform hydrogen number density n_H. This model has similar geometric configuration as outlined in Nenkova et al. (Nenkova, Sirocky, Ivezić, and Elitzur, 2008; Nenkova, Sirocky, Nikutta, et al., 2008). It involves assuming a powerlaw distribution of clumps

along the radial direction between inner and outer radii. Along the azimuthal axis, it follows a Gaussian distribution of clumps (Figure 11). Therefore, the number density function, in given as:

$$d_n(r, \theta, \phi) = \alpha \left(\frac{r}{r_{\text{in}}} \right)^{-q} \exp \left(-\frac{(\theta - \pi/2)^2}{\sigma^2} \right) \tag{12}$$

Here, θ is the azimuthal angle, σ is the torus opening angle and α is the normalization constant given as:

$$\alpha = \frac{(1-q) \, N_c^{\text{eq}}}{\pi \, R_c^2 \, r_{\text{in}}^q \, (r_{\text{out}}^{1-q} - r_{\text{in}}^{1-q})} \tag{13}$$

The number of clumps along the equatorial plane is N_c^{eq}. Thus, the number of clumps along the LOS is calculated using equation 13 in equation 12, for a given angle:

$$N_c^{\text{LOS}}(\theta) = N_c^{\text{eq}} \exp \left(-\frac{(\theta - \pi/2)^2}{\sigma^2} \right) \tag{14}$$

The total number of clumps can be calculated as using:

$$N_c^{\text{Total}} = \int_{r_{\text{in}}}^{r_{\text{out}}} \int_0^\pi \int_0^{2\pi} d_n(r, \theta, \phi) \, r^2 \sin\theta \, dr \, d\theta \, d\phi \tag{15}$$

The default parametric values of XCLUMPY (see webpage) provides us $N_c^{\text{Total}} \sim 10^6$. In summary, this model is characterized by eight distinct parameters for the torus properties: r_{in}, r_{out}, R_c, N_c^{eq}, q, σ, N_H^{eq} and inclination angle (i). In Ichikawa et al., 2015, CLUMPY model is applied in IR SED for 21 local AGN. From the result of that SED fitting, the default values of r_{in}, r_{out}, N_c^{eq}, q are fixed at mean values. The clump size R_c is fixed following the theoretical estimate of Kawaguchi and Mori, 2010, 2011, using the logarithmic average of clump diameter within torus region. This value is compatible with the X-ray observations in low redshift AGN (Markowitz et al., 2014). So, only three parameters are kept free to fit the observational data for this code: σ, N_H^{eq} and i.

Model components

XCLUMPY uses the MONACO framework (Odaka et al., 2011, 2016) to model the interaction between X-rays and a clumpy torus irradiated from its central position. For simplicity, it is assumed that all matter in the torus consists of neutral cold gas, disregarding thermal motion. The considered physical processes include photoelectric absorption, followed by fluorescence line emission and Compton scattering. All the Compton scattering are assumed to be occurred with electrons bound to atoms or molecules, instead of a medium with free electrons. Although this assumption may not be valid in the presence of ionized plasma, any deviation would only lead to slight energy shifts of scattered X-rays by electron binding energies. Such deviations are inconsequential, except for high energy resolution spectroscopy, like that achieved by a microcalorimeter (Hitomi Collaboration et al., 2016). The models are calculated by utilizing the photoelectric cross sections compiled from the National Institute of Standards and Technology database (Schoonjans et al., 2011) and adopting Solar abundances following Anders and Grevesse, 1989.

It consists of four components: galactic absorption ($const * phabs$), transmitted continuum ($cabs * zphabs * zcutoffpl$), reflection continuum ($xclumpy\_reflection$) and fluorescent line ($xclumpy\_reflection$). We added another extra component to calculate the scattered unabsorbed powerlaw emission, given as $f_s * zcutoffpl$. The reflection and line component is provided by the fits files[5]: `xclumpy_v01_RC.fits` and `xclumpy_v01_RL.fits`, respectively. Both the components are made up of six parameters: N_H^{eq}, (2) torus angular width (σ), (3) inclination angle (i), (4) photon index (Γ), (5) cutoff energy and (6) a normalization factor. The parameters of reflection and line components are tied together, considering both the components originating from the same region. In `XSPEC` the following model configuration is used:

$$\text{Model XCLUMPY} = const * phabs * (cabs * zphabs * zcutoffpl + f_s * zcutoffpl$$
$$+ atable\{\texttt{xclumpy\_v01\_RC.fits}\} + atable\{\texttt{xclumpy\_v01\_RL.fits}\})$$
$$(16)$$

Following the equation 14, the LOS column density ($N_{H,LOS}$) can be calculated as follows:

---

[5] https://github.com/AtsushiTanimoto/XClumpy

$$N_{\text{H,LOS}} = N_{\text{H,eq}} \left[\exp\left\{ \frac{(\theta_i - 90°)^2}{\sigma^2} \right\} \right] \qquad (17)$$

The 90% confidence error range of $N_{\text{H,LOS}}$ is calculated using the standard error propagation method over the parameters $N_{\text{H,eq}}$, σ and θ_i, from the formula 17.

2.2.7 UXCLUMPY

The obscurer in the Unified X-ray CLUMPY (UXCLUMPY) model, by Buchner et al., 2019, has several clumpy torus geometries of interests. Similar to XCLUMPY, the fundamental idea has been followed from the Nenkova, Sirocky, Ivezić, and Elitzur, 2008; Nenkova, Sirocky, Nikutta, et al., 2008, with equation 12. But to compute the X-ray spectra, they developed a new Python-based Monte Carlo simulation code 'XARS' (X-ray Absorption Re-emission Scattering), which is publicly available[6]. Below, we discussed the geometrical model on the basis of which UXCLUMPY has been constructed using the XARS code.

Physical Geometry

The construction of a clumpy obscurer model can have infinite degrees of freedom, as each point of the obscuration can possesses arbitrary density. The geometrical configuration is constrained in a realistic way, by widening the parametric space of column density distribution. This is achieved by allowing at a given luminosity a diversity of opening angle of torus or by giving the torus clouds a diversity in column densities. UXClUMPY adopted a larger parameter space for column density to take into account the variability within the CT and CTn variations, allowing a range of values for the column density of individual clouds N_H^{cloud}. However, the radial cloud distribution is assumed to be uniform across two orders: $Y = r_{\text{out}}/r_{\text{in}} = 100$ (in comparison, $Y = 20$ for XCLUMPY). They assumed the inner ionised clouds (even those close to the BLR) can also act as an absorber, so they introduced a longer range of the torus width. It adopts an exponential distribution of the angular sizes centred around $\theta^{\text{cloud}} = 1°$. The clouds are assumed to be spherical blobs with diameter $D^{\text{cloud}} = d \cdot \sin(\theta^{\text{cloud}})$ for a distance d from the observer. It is also constructed taking

---

[6]https://github.com/JohannesBuchner/xars

into account the rates nucleus eclipse event. For the clumpy geometry, it assumes for simplicity circular Keplerian orbits, on random planes of orientation. The orbital period of the innermost cloud is set to to one day and outer-most clouds to a period of eight years. These corresponding distances are consistent with observationally inferred distances from Markowitz et al., 2014, in which they showed how the probability to see a cloud event increases with longer span of observations.

To produce a better fit for all kinds of local heavily obscured AGN with high covering fraction and column density ($N_H > 10^{25}$ cm^{-2}), UXCLUMPY introduces an optional inner-ring of CT reflecting 'mirror' to reproduce the narrow high-energy Compton hump those CT-AGN. This reflecting mirror is assumed to be located in the inner region of the torus, in such a way that it is unobscured along the LOS of the observer and coronal emission, while the LOS from the observer and corona is obscured. For this inner ring, the dispersion of the cloud population (TORsigma) and the covering factor of the CT inner ring (CTKcover), by tuning the number of clouds. It decreases the number of cloud by an order as $N_c^{\text{Total}} \sim 10^5$ (check the standard equation 15) and proportionally increases the angular size $\theta^{\text{cloud}} = \sqrt{10} \cdot 1° \approx 3°$, for better computational efficiency without harming the X-ray spectra significantly.

Model components

This model is made up of three components: (a) galactic absorption ($const*phabs$), (b) $uxclumpy$ itself, which is composed of the transmitted and cold reflected component with fluorescent lines, given as fits file `uxclumpy.fits`; and (c) $uxclumpy\_scattered$ which takes into account the warm reflected component responsible for the scattering of the power-law from coronal emission, given as `uxclumpy-omni.fits`. Both the components are composed of seven parameters: (1) photon index (Γ), (2) cutoff energy, (3) normalization factor at 1 keV, (4) LOS column density, (5) inclination angle, (6) vertical cloud dispersion (TORsigma) and (7) covering fraction of inner ring (CTKcover). The following model configuration is used in XSPEC:

$$\text{Model } \mathtt{UXCLUMPY} = const * phabs * (atable\{uxclumpy.fits\}+ $$
$$f_s * atable\{\mathtt{uxclumpy\text{-}omni.fits}\}), \tag{18}$$
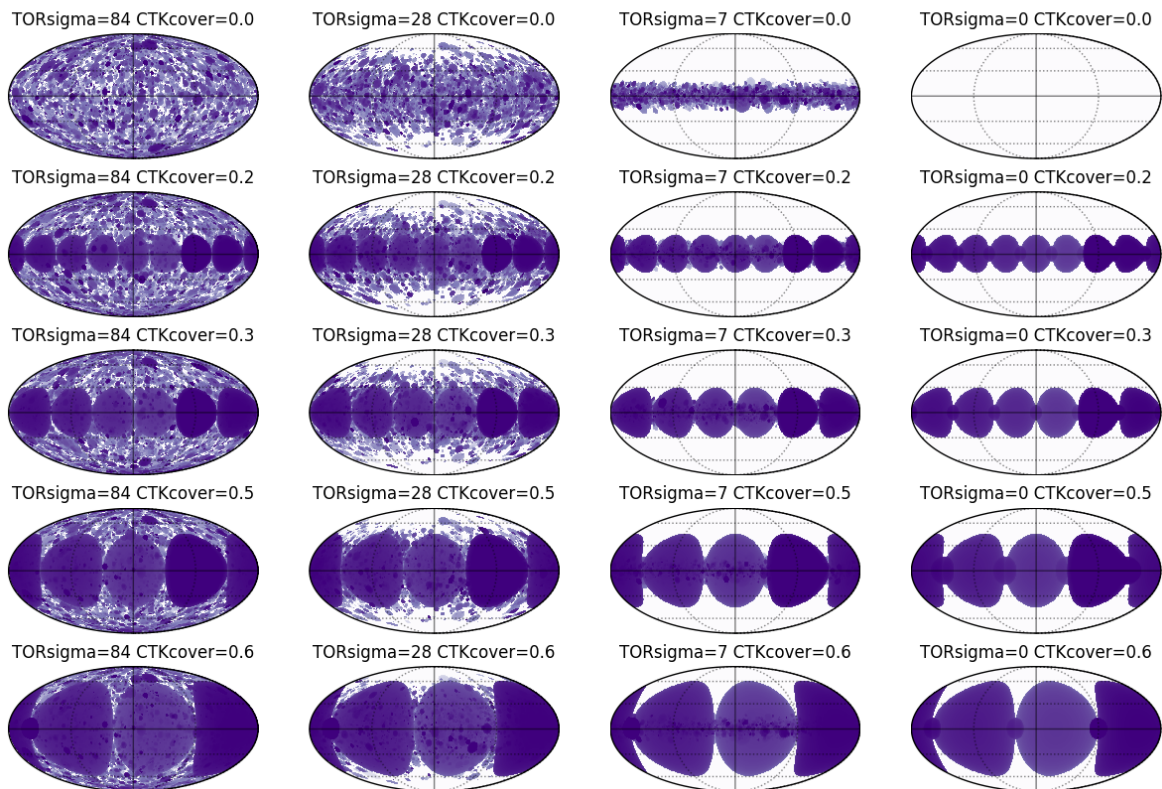
Figure 12: Different model grids of `UXCLUMPY` for different values of TORsigma and covering fraction of inner warm reflector, adopted from Buchner et al., 2019.

The parameters of the components are tied together, only keeping f_s as free to compute the scattering fraction.

2.3 X-Cigale and multi-band SED fitting

SED fitting is a potent technique for understanding astronomical souces. It involves creating models that replicate observed emission spectra across various wavelengths from X-ray to radio, providing insights into properties, such as stellar composition, dust content, and black hole activity. SED modeling relies on the fact that different galaxy components emit radiation at distinct wavelengths. Modeling these contributions help deducing the underlying physical characteristics, such as the presence of specific elements, molecular compounds, and details about the stellar population's age

and metallicity. The first step of SED fitting involves creating a comprehensive grid of models for comparison with observations. Since our sources are obscured AGN, it is essential to generate detailed models for both the host galaxy and the AGN activity. The Code Investigating GALaxy Emission (CIGALE)[7] represents a cutting-edge PYTHON code designed for SED fitting of extragalactic sources (Boquien et al., 2019). The updated version included with the X-ray module of Yang et al., 2020, and now called called 'XCIGALE'. It also utilizes physical models for both AGN and host galaxies, and allows flexible combination between them. In this section, we will briefly discuss the statistical approach and different modules of XCIGALE, that is used in this thesis.

2.3.1   XCIGALE: Bayesian statistics

In Bayesian statistics, the probability of a model being a good representation of the data depends on the given prior knowledge on the observed data. The probability of observing the given data under a specific condition or set of model parameters is called it's probability likelihood function. It is represented as $L(D|\theta)$, where θ represents the model parameters and D is the observed data. Therefore, following Bayes' theorem, the posterior distribution $L(\theta|D)$ is defined as the updated probability of the initial conditions or input model parameters after taking into account the observed data, formulated as:

$$L(\theta|D) = \frac{L(D|\theta) \cdot L(\theta)}{L(D)} \tag{19}$$

Here, $L(\theta)$ is the prior information on the model and $L(D)$ is the probability of observing the data independent of the prior conditions. These likelihood functions are expressed in χ^2-statistics for SED fitting. For a given observed flux $f(\nu_i)$ with a given energy ν, model flux $f_\theta(\nu_i)$ and uncertainty σ_i, the χ^2 distribution is given as:

$$\chi^2 = \sum_i \frac{[f_\theta(\nu_i) - f(\nu_i)]^2}{\sigma_i^2} \tag{20}$$

Therefore, the likelihood function is calculated as $L = \mathrm{e}^{-\chi^2/2}$, assuming Gaussian distribution. For a given model parameters, the low χ^2 values show high probability

---

[7]https://cigale.lam.fr

that the model is a good representation of the observed data. The SED fitting process aims is to find out the physical properties of the astrophysical source. It is achieved by comparing the observed SED with a range of SED models that represent various physical situations. The prior information (the input values) influences the likelihood function, giving more weightage to the output paramteric values to produce a better fit.

XCIGALE enables users to input model parameters, to generate the SED models with all possible parameter combinations. It convolves these SED with filters to obtain model fluxes and compare them with the observed fluxes. The comparison is done using the likelihood function L for each model. It supports two types of statistical analyses: maximum likelihood (with minimum $\chi 2$) and Bayesian approach. In the maximum likelihood analyses, it selects the model with highest L value to calculate physical properties (like stellar mass, star forming rate etc.) for that model only. In Bayesian analyses, it calculates the marginalized probability distribution function (PDF) for each physical property based on the L value of all the models. Thereafter, it derives the estimated value of the physical parameter from probability-weighted mean and uncertainity from the standard deviation. In the next two section, I discussed the prior conditions in form of different physical conditions of the input models, that is used in XCIGALE to derive the best-fit.

2.3.2   X-ray and AGN models

The nuclear emission from an active galaxy is moduled into three components by XCIGALE: accretion disk, torus and polar dust. The old CIGALE AGN model (Fritz et al., 2006) employed within the range of UV-to-IR SED, assumed a smooth structure for the dusty torus. However, recent theoretical and observational studies propose that the torus is primarily composed of dusty clumps (e.g., Buchner et al., 2019; Stalevski et al., 2012; Tanimoto et al., 2019a). In response, the XCIGALE framework has introduced the 'SKIRTOR' model (Stalevski et al., 2012, 2016), composed of two-phase clumpy torus model based on the 3D radiative-transfer code SKIRT (Baes et al., 2011; Camps and Baes, 2015). Most of the dust in SKIRTOR are composed of high density clumps (mass fraction 97%), while the remaining are smooth distribution. In place of isotropic disk emission of Fritz's model, SKIRTOR assumes anisotropy in the accretion disc emission. Thus, SKIRTOR is recommended to use as it's more

compatible with observations, even though Fritz model is also available to be used in XCIGALE. Additionally, it was found that SKIRTOR overestimates the fraction of far UV luminosity in comparison with observation. To overcome this discrepancy, a new disk SED (Feltre et al., 2012) is introduced following the observations (Duras et al., 2017) in the updated XCIGALE code.

The polar dust model is introduced to address the dust extinction in type I AGN. It outlines the geometry of obscuring materials, termed 'polar dust,' responsible for type I AGN obscuration. Local Seyfert galaxies have revealed polar dust through high-resolution mid-IR (MIR) imaging. Instead of constructing a grid of physical models, XCIGALE employs empirical extinction curves, including those from nearby star forming galaxies (Calzetti et al., 2000), large dust grains (Gaskell et al., 2004) and small magellanic clouds (SMC; Prevot et al., 1984), which users are free to choose. The extinction amplitude, parameterized as E(B-V), remains a user-defined free parameter. Following the AGN-unification scheme, XCIGALE aligns with the model where the AGN type depends on the viewing angle (or inclination). Type I AGN, observed in polar directions, experience moderate extinction from polar dust. While type II (or obscured) AGN, have disc emission significantly obscured by the torus. Users can constrain inclination angle based on known AGN types or adopt multiple angles, enabling XCIGALE to freely select between them.

Along with these AGN modules, the X-ray emission from the central engine is also responsible to drive the spectral shape. Also, host galaxies can contribute to the X-ray emission. The X-ray module in XCIGALE is designed to work on the intrinsic X-ray fluxes in the given energy band (including both soft and hard X-ray band). Just like the coronal powerlaw emission from equation 5, XCIGALE adopts:

$$f_\nu \propto E^{-\lambda+1} \, e^{-E/E_{cut}} \tag{21}$$

Here, E_{cut} is the high energy exponential cut-off energy. The typical value for E_{cut} is set at 300 keV (Dadina, 2008; Ricci et al., 2017) from the observations of Seyfert galaxies, keeping $\Gamma = 1.8$ (Liu et al., 2017; Yang et al., 2016). It's noteworthy that, as the cut off energy exceeds the highest observable energy for most X-ray observatories (e.g., Chandra and XMM–Newton). However, the specific selection of E_{cut} has negligible effects on the fitting with XCIGALE in the majority of cases. Besides AGN, there are three main origins of X-ray emission from the host galaxies: low-mass X-ray binaries

(LMXB), high-mass X-ray binaries (HMXB), and hot gas. These emissions are most of the times, much weaker than the powerlaw emissions of AGN. The details of how these three components are modeled will be found in Yang et al., 2020. Since this thesis is based on AGN, I will strictly focus on the coronal emissions.

XCIGALE also includes the $\alpha_{ox} - L_{2500\text{Å}}$ relation for AGN as a prior, assuming a universal behavior across all luminosities originating from the fundamental accretion mechanism (e.g., Just et al., 2007; Lusso and Risaliti, 2017; Steffen et al., 2006). It adopt this well-studied relation, where $L_{2500\text{Å}}$ is the AGN intrinsic luminosity at 2500Å and α_{ox} is the SED slope between UV and X-ray (at 2 keV). The code adopts the observed $\alpha_{ox} - L_{2500\text{Å}}$ relation from Just et al., 2007:

$$\alpha_{ox} = -0.137 \log(\text{L}_{2500\text{Å}}) + 2.638 \tag{22}$$

Here the unobscured AGN emission is assumed to be isotropic at both UV/optical and X-ray band. However, due to the dynamic nature of the accretion disk, the angular distribution of the radiative energy is anisotropic in nature in the UV/optical band. Thus, the disc luminosity can be approximated following the angular dependence as $\text{L}_{\text{disk}} \propto \cos\delta(1 + 2\cos\delta)$ (e.g., Netzer, 1987), where δ is the angle from the vertical axis of AGN. This equation was adopted within the SKIRTOR model. For simplicity, the X-ray emission is assumed to be more isotropic than the UV/optical emission, because it is a reprocessed emission originating from the inverse Compton scattering with the hot plasma.

2.3.3 Dust and stellar models

Galaxies undergo complex evolutionary processes involving gas accretion-expulsion and interactions, leading to substantial variations in their SFR over cosmic times. Constraining the star formation history (SFH) of galaxies is challenging due to the intricate nature of these variations. With advancements in numerical simulations, more realistic SFH derived from simulations or semi-analytic models (e.g., Boquien et al., 2014; Pacifici et al., 2012) become feasible. CIGALE accommodates both analytical SFH dependent on various parameters and arbitrary SFH to encompass these diverse approaches. There are primarily three modules: SFH defined by single or double exponentials (`sfh2exp`), delayed SFH with an optional exponential burst (`sfhdelayed`),

and periodic SFH (`sfhperiodic`). A straightforward approach to galaxy star formation history (SFH) modeling involves employing one or two decaying exponentials. Following this conceptual framework, in `sfh2exp`, the initial exponential characterizes the long-term star formation responsible for the bulk of the stellar mass, while the subsequent exponential represents the more recent burst of star formation. For `sfhdelayed` model, the SFR peaks at a particular time τ and then exponentially decays. In contrast, `sfhperiodic` follows a periodic star formation. For stellar spectra, XCIGALE relies on two popular single stellar population (SSP) libraries: `bc03` (Bruzual and Charlot, 2003) and `m2005` (Maraston, 2005). The differential reddening between young stellar populations within their dust clouds and older populations (e.g., Charlot and Fall, 2000) are calculated and stored separately. This allows to compute the attenuation independently in the subsequent module. XCIGALE models the nebular emission through a multi-step process. It selects the nebular templates of Inoue, 2011, based on ionization parameter (U) and metallicity (Z). These templates are derived from CLOUDY 13.01 (Ferland et al., 1998, 2013), predict the intensities of 124 lines from H II regions. The helium and nitrogen abundances are scaled following the metallicity Nagao et al., 2011.

The code also utilizes attenuation laws to model the effect of dust on observed radiation within galaxies. These laws exhibit variations across different redshifts and galaxies, necessitating a wide range of shapes and normalizations for comprehensive coverage. Two distinct approaches are offered by XCIGALE to model attenuation curves: the implementation of the Charlot and Fall, 2000 model within the `dustatt_modified_CF00` module and the utilization of flexible laws inspired by the starburst curve of Calzetti et al., 2000, within the `dustatt_modified_starburst` module. While the former acknowledges the differences in attenuation curves between young stars within their birth clouds and those within the interstellar medium, the latter employs an empirical approach based on the Calzetti et al., 2000 starburst attenuation curve, allowing for parametrization for enhanced flexibility. It also includes adjustments to the slope and the incorporation of a UV bump modeled as a Drude profile. For dust emission, XCIGALE has three sets of models: Dale et al., 2014, updated Draine and Li, 2007 and Casey, 2012. The `dale2014` module employs empirical templates derived from nearby star-forming galaxies, with the dust mass characterized by a power-law index intricately linked to the 60–100 μm color. Despite it's simplicity, this approach exhibits limited variability in polycyclic aromatic hydrocarbon (PAH) emission concerning the total IR band. In contrast, the models in Draine and Li, 2007 incorporate a mix-

49

ture of amorphous silicate, graphite, and PAH, delineating dust emission into diffuse and star-forming components. The `dl2014` module refines these models, broadening the parameter space and enhancing aspects like the treatment of graphite and dust mass normalization. However, it's important to note that these more flexible models come with a larger parameter space, rendering them computationally more demanding compared to the `dale2014` templates. For `casey2012`, the modeling of dust emission involves two components: firstly, a single-temperature modified black body in the FIR representing the reprocessed starburst emission throughout the entire galaxy. Secondly, a powerlaw in the mid-IR that serves as an approximation for hot-dust emission resulting from AGN heating or clumpy, hot starbursting regions.

3 Compton-thick AGN in the NuSTAR Era: Analysis of seven local CT-AGN candidates

In this chapter, the analysis of seven local CT-AGN candiates are presented, using physically motivated torus models as mentioned in Section 4.3.2. It is broadly based on the results showed in Sengupta et al., 2023.

3.1 Introduction

Diffuse X-ray emission from the central regions of accreting supermassive black holes in active galactic nuclei (AGN) is responsible for most of the cosmic X-ray background (CXB) radiation from a few keV to a few hundred keV (Comastri, 2004; Gilli et al., 2007; Ueda et al., 2014). The contribution of unobscured AGN to the CXB is almost completely resolved into point-like sources at E< 10 keV (Hickox and Markevitch, 2006; Worsley et al., 2005). Compton-thick AGN (CT-AGN; i.e. line-of-sight (LOS) column density $> 10^{24}$ cm^{-2}) significantly contribute ($\sim 15 - 30\%$ Ananna et al., 2019; Gilli et al., 2007) to the CXB around its peak ($\sim 20 - 30$ keV; Ajello et al., 2008). In the local Universe ($z \leq 0.1$), the fraction of CT-AGN revealed by the X-ray observations is found to be $\sim 5\% - 10\%$ (Ricci et al., 2015a; Torres-Albà et al., 2021; Vasudevan et al., 2013). This reveals a large discrepancy with the predictions of AGN population synthesis models, which postulate that the fraction of local CT-AGN should be of $\sim 20\% - 50\%$ (Ananna et al., 2019; Ueda et al., 2014) to model the CXB properly.

For low-redshift AGN, the circum-nuclear dusty torus clouds are considered as the dominant medium of obscuration; that is, obscuration from the interstellar medium (ISM) of the host galaxy is expected to be less significant (e.g. Gilli et al., 2022). Due to significant suppression of intrinsic X-rays below 10 keV by these obscuring Compton-thick clouds, it is difficult to detect heavily obscured AGN at $z \sim 0$ in the soft X-ray (E< 10 keV) band. As heavily obscured AGN have a noticeable Compton hump at $\sim 20 - 40$ keV, hard X-ray (E> 10 keV) observatories allow the detection and characterisation of these kinds of sources at $z \sim 0$. For example, the *Swift* Burst Alert Telescope (BAT) is used as it is less biased against CT-AGN sources, being sensitive in the 15-150 keV range. To determine the existing CT-AGN fraction, using a BAT volume-limited sample is among the most efficient ways to reduce the bias

against the obscured sources. The importance of an obscuring medium surrounding the meso scale ($\sim 1 - 100$ pc) around AGN has been highlighted by several theoretical and numerical investigations (Gaspari et al., 2020, for a review). Briefly, in realistic turbulent environments, the host diffuse medium is expected to recurrently condense in a top-down multi-phase condensation cascade of warm and cold clouds, which then rain onto the central AGN. Such chaotic cold accretion (CCA; Gaspari et al., 2013) is therefore often responsible for a clumpy distribution at the meso scale, and boosts the feeding rates at the micro-scale (< 1 pc). This multi-scale rain has been constrained and detected in a wide range of galaxies and AGN (e.g. Gaspari et al., 2019; Maccagni et al., 2021; Marchesi et al., 2022; McKinley et al., 2022; Rose et al., 2019; Temi et al., 2022).

The 100 month Swift-BAT catalogue[8] (the updated 150 month BAT catalogue is in preparation, K. Imam et al.) consists of 414 AGN at $z < 0.05$. From this AGN population, our Clemson-INAF research group[9] selected a sample of 55 CT-AGN candidates[10] for which archival and Guest Observer observations with the Nuclear Spectroscopic Telescope Array are available (*NuSTAR*; Harrison et al., 2013). The target sources are observed by *NuSTAR* within the energy range of 3-79 keV with high sensitivity, because *NuSTAR* is the first instrument to focus X-ray photons at E>10 keV. For the soft X-ray coverage at E<10 keV, we used the available X-ray spectra from XMM-*Newton*, *Chandra*, or *Swift-XRT*. We carried out a systematic and comprehensive spectral analysis in $0.6 - 50$ keV band on each of the 55 sources using the uniform torus models, MYTorus and borus02 (see Marchesi et al., 2018; Torres-Albà et al., 2021; Traina et al., 2021; Zhao et al., 2021). In this work, we present the results of the last seven sources from this sample. Here, we independently computed LOS column density ($N_{H,LOS}$) and average torus column density ($N_{H,avr}$ or $N_{H,tor}$) in order to study the clumpiness of the torus clouds even within the uniform torus framework. The $N_{H,LOS}$ is derived from the absorbed powerlaw coming directly from the 'corona'. The $N_{H,avr}$ is instead obtained from the reflection component, which can be modelled to derive the average properties of the obscuring medium, such as the above-mentioned average torus column density, the obscuring medium covering factor (C_{Tor}), and its inclination angle (θ_{Inc}) with respect to the observer.

This paper is organised as follows: In Section 3.2, we discuss the selection methods and

---

[8]http://bat.ifc.inaf.it/100m_bat_catalog/100m_bat_catalog_v0.0.htm
[9]https://science.clemson.edu/ctagn/
[10]These CT-AGN candidates were also present in the 70 month BAT catalogue.

data analysis techniques. In Section 3.3, we present physically motivated torus models used in this work. Then, in Section 3.4, we show the results of each of the sources we analysed. In Section 3.5, we analyse and discuss our CT-AGN at $z < 0.05$, and display the current census of such objects, combining our results with those obtained in previous works. Finally, in section 3.6, we present the conclusions and a brief summary of our work, and mention some possible future projects. In Appendix A and B, we show the tables of best-fit parameters and X-ray spectral fitting plots, respectively. All reported error ranges are at the 90% confidence level unless stating otherwise. Through the rest of the work, we assume a flat ΛCDM cosmology with $H_0 = 69.6\,\mathrm{km\,s^{-1}\,Mpc^{-1}}$, Ω_m=0.29, and Ω_Λ=0.71 (Bennett et al., 2014).

3.2   Sample selection and data reduction

The seven sources (see Table 1 for details) of our sample are CT-AGN candidates selected from the volume-limited sample of the Swift-BAT 100 month catalogue in the local Universe (z< 0.05, $D \lesssim 200$ Mpc). These Seyfert galaxies were previously classified as CT-AGN in the Ricci et al., 2015a. They used the `BNtorus` model (Brightman and Nandra, 2011), where *Swift-XRT* was used for E< 10 keV (except for ESO138-G001, where XMM-*Newton* data were used) and *Swift-BAT* for E> 10 keV. Instead of BAT observations (15-150 keV), we are using *NuSTAR* in the 3-50 keV range, as it is a grazing incidence telescope with lower background and a smaller field of view, resulting in excellent sensitivity to source detection with better photon statistics. At E< 10 keV, we preferred XMM-*Newton* or *Chandra* for better data quality, particularly in terms of source statistics compared to *Swift-XRT*. For NGC 2788A, only *Swift-XRT* data were available. The objects analysed in this work are CT-AGN candidates in the 100 month BAT sample for which no analysis with `MYTorus` or `borus02` of the joint soft X-ray and NuSTAR spectra have yet been published.

NuSTAR **data reduction**

We used both focal plane modules FPMA and FPMB of *NuSTAR* for each source. The collected data have been processed by NuSTAR Data Analysis Software– NUSTARDAS version 2.0.0. The raw event files are calibrated by the *nupipeline* script using the response file from the Calibration Database– CALDB version 20210202. The source

Table 1: Observational details of each sources.

Source	AGN Types	log flux[a]	Redshift (z)	Instrument	Sequence ObsID	Start Time (UTC)	Exposure Time (ks)	Net Counts[b]
MCG-02-12-017	Sy2	8.84	0.03246	XMM-*Newton*	0762920601	2016-03-01	30.0	753, 225, 270
				NuSTAR	60001160002	2014-11-28	34.0	441, 379
				NuSTAR	60101015002	2016-03-02	19.5	349, 369
NGC 4180	Sy2	17.58	0.00699	*Chandra*	9438	2008-11-16	2.1	6
				NuSTAR	60201038002	2016-07-14	23.4	429, 387
				NuSTAR	60160480002	2020-07-14	31.6	212, 212
NGC 2788A	Sy2	21.46	0.01335	*Swift-XRT*	*[c]	2008—2020	17.8[d]	34
				NuSTAR	60469001002	2019-06-14	27.6	608, 617
				NuSTAR	60160344002	2020-08-14	23.2	639, 530
NGC 1106	Sy2	15.49	0.01447	XMM-*Newton*	0821870301	2019-03-02	32.6	1129, 257, 422
				NuSTAR	60469002002	2019-02-22	18.7	285, 332
				NuSTAR	60160130002	2020-09-09	22.3	360, 354
ESO406-G004	Sy2	12.38	0.02897	*Chandra*	14050	2012-06-07	5.1	25
				NuSTAR	60201039002	2016-05-25	36.3	390, 357
				NuSTAR	60161799002	2020-06-26	23.7	120, 86
2MASX J20145928+2523010	Sy2	10.55	0.04422	XMM-*Newton*	08024505501	2017-11-18	44.8	5232, 1980, 1134
				Chandra	21299	2018-12-17	3.7	532
				NuSTAR	60201032002	2017-05-27	28.1	1252, 1137
				NuSTAR	60160731002	2020-04-21	9.4	608, 624
ESO138-G001	Sy2	19.46	0.00914	XMM-*Newton*	0690580101	2013-02-24	135.4	27058, 8878, 9016
				NuSTAR	60201040002	2016-05-22	45.7	3101, 2806
				NuSTAR	60061274002	2020-04-01	53.2	3463, 3328

[a]These fluxes are measured in erg cm^{-2} s^{-1} units. AGN types and log flux between 14 and 195 keV is reported from the 105 month BAT catalogue of Oh et al., 2018. Only for ESO406-G004 is the AGN type reported from Koss et al., 2016.

[b]The reported XMM-*Newton* net counts (background-subtracted total source counts) are those of the PN, MOS1, and MOS2 modules for a radius of 30" in 0.3–10 keV, respectively. The reported *NuSTAR* net counts are those of the FPMA and FPMB modules for a radius of 30" between 3 and 50 keV, respectively. The reported *Chandra* net counts are for the ACIS-I detector for a radius of 5" in 0.5–7 keV. The reported *Swift-XRT* net counts are for a radius of 12" in 0.5–10 keV.

[c]Collection of the following ObsID- 00081038001, 00037312004, 00037312002, 00037312001, 00037312003, 03106140004, 03106140005, 03106140004, 03106140001, 03106140002, 07002346001, 07002347001.

[d]Total exposure time of all the *Swift-XRT* observations

54

and background spectra are extracted from $30''$ ($\approx 50\%$ of the encircled energy fraction–EEF at 10 keV) and $50''$ circular regions, respectively. Using *nuproducts* scripts, we generated source and background spectra files, along with response matrix files–RMF and ancillary response files–ARF. Finally, the *NuSTAR* spectra are grouped with at least 20 counts per bin using *grppha*. For each source, we used all the available *NuSTAR* observational data taken during different epochs in order to (a) check variability, and (b) improve the statistics of the spectra of these obscured sources between 3 and 50 keV.

XMM-*Newton* data reduction

In XMM-*Newton*, we collected the data from the PN, MOS1, and MOS2 detectors. Using SAS version 19.0.0, we processed the data using *epproc* and *emproc* for the PN and MOS filters, respectively. Finally, we reduced and cleaned the flares using *evselect*. The source photons were obtained from a $30''$ circular region, with $\sim 85\%$ EEF for EPIC-PN at 1.5 keV. Background spectra were extracted from a $50''$ circle near the source. Each spectrum has been binned at 20 counts per bin using *grppha*. We prefer to use XMM-*Newton* wherever it is available, because the effective area of XMM-*Newton* in 0.3-10 keV is approximately ten times bigger than the *Swift-XRT* one and approximately two times bigger than the *Chandra* one.

***Chandra* data reduction**

Although the effective area of *Chandra* is smaller than that of XMM-*Newton*, it is still five times larger than that of *Swift-XRT*. Also, *Chandra* shows better angular resolution, a lower background, and has a greater capacity to resolve extended emission from non-nuclear sources. We use *Chandra* in two different scenarios: (1) when XMM-*Newton* data are not available and (2) to improve the photon statistics at E< 10 keV when they are. CIAO version 4.13 is used to process and reduce the data. The source spectra are extracted using a circular region of $5''$ radius, which includes > 99% EEF.

3.3 X-ray spectral modeling

For X-ray spectral fitting on the objects in our sample, we used `XSPEC` Arnaud, 1996 version 12.11.1 in HEASOFT. The metal abundance is fixed to solar metallicity from Anders and Grevesse, 1989, while the photoelectric cross sections for all absorption components are obtained using the approach of Verner et al., 1996. The Galactic absorption column density is fixed for each source in our sample following Kalberla et al., 2005. We also used a thermal `mekal` (Kaastra, 1992; Liedahl et al., 1995; Mewe et al., 1985) component to phenomenologically model the soft excess which is often observed in the spectra of obscured AGN.

We followed a standard approach to analyse the CT-AGN candidates —using self-consistent and up-to-date physically motivated uniform torus models— based on Monte Carlo simulations: `MYTorus` (Murphy and Yaqoob, 2009; Yaqoob, 2012) and `borus02` (Baloković et al., 2018), which are specifically developed to characterise the X-ray spectra of heavily obscured AGN. In this section, we describe how these two uniform torus models are used.

MyTorus

The obscuring material in `MYTorus` follows a toroidal or donut-like geometry, with circular cross-section. This model consists of three components: direct continuum ($MYTZ$), Compton-scattered continuum ($MYTS$), and a fluorescent line component ($MYTL$). The $MYTZ$, also called the zeroth-order component, models the attenuation of intrinsic X-ray radiation by the obscuring torus on the LOS of the observer. The second component, $MYTS$, computes the Compton-scattered photons, which are responsible for the Compton hump near $\sim 20-30$ keV. Finally, $MYTL$ models prominent fluorescent emission lines such as: Fe K_α and Fe K_β around 6.4 keV and 7.06 keV, respectively. Following the techniques in Yaqoob, 2012 and from the previous results of Marchesi et al., 2018, Marchesi, Ajello, Zhao, Marcotulli, et al., 2019, Marchesi, Ajello, Zhao, Comastri, et al., 2019, Zhao, Marchesi, Ajello, et al., 2019, Zhao, Marchesi, and Ajello, 2019, Traina et al., 2021, Torres-Albà et al., 2021 and Silver et al., 2022, we used only the decoupled configuration of `MYTorus` to estimate the clumpiness of the torus clouds. Here, we calculated the column density from direct continuum ($N_{H,z}$) and scattered continuum ($N_{H,S}$) separately, allowing flexibility on the parameter estimation

even within a uniform cloud distribution framework. The ratio $N_{H,z}/N_{H,S}$ is used to evaluate the clumpiness, depending on how far the ratio is from unity. In `XSPEC`, the configuration is as follows:

$$\text{Model MyTorus}_{\text{edge−on}} = C_{Ins} \; * \; phabs \; *$$
$$(zpow * MYTZ + A_{S,90} * MYTS + A_{L,90} * MYTL+ \tag{23}$$
$$f_s * zpow + mekal + zgauss),$$

$$\text{Model MyTorus}_{\text{face−on}} = C_{Ins} \; * \; phabs \; *$$
$$(zpow * MYTZ + A_{S,0} * MYTS + A_{L,0} * MYTL+ \tag{24}$$
$$f_s * zpow + mekal + zgauss).$$

Here, equation 23 models the edge-on view ($\theta_{\text{Inc}} = 90°$) and equation 24 the face-on view ($\theta_{\text{Inc}} = 0°$) of the AGN. We used both inclination angles to carry out a comparative study of the scattering column density arising from the polar dust (edge-on) versus that from the back-reflection of the torus (face-on). We equated and fixed the relative normalisations from scattering and line components, $A_S = A_L = 1$, as we consider them to have originated from the same regions where the direct power-law emerged. C_{Ins} is a cross-calibration constant between the different instruments of telescopes (or a cross-normalization constant between different observations of the same telescopes). We also included some additional components: f_s to compute the scattering fraction from the direct power law that does not interact (or elastically interacts) with the torus, *mekal* to phenomenologically model the soft excess, and *zgauss* to include any additional emission lines.

BORUS02

The obscuring medium in `borus02` consists of a spherical geometry with biconical (polar) cut-out regions (Baloković et al., 2018). This model is composed of three components: (a) `borus02` itself, which is a reprocessed component (including Compton-scattered + fluorescent line component), (b) $zphabs * cabs$ to include LOS absorption with Compton scattering through the obscuring clouds; with this component we multiply a $cutoffpl_1$ to take into account the primary power-law continuum, and (c) finally

another $cutoffpl_2$ component is included separately with f_s to include a scattered unabsorbed continuum. The significant difference between borus02 and MYTorus is that the torus covering factor (C_{Tor}) in this model is kept as a free parameter varying in the range of $0.1 - 1$ (i.e. the torus opening angle is in the range of $\theta_{Tor} = 0° - 84°$), along with inclination angle θ_{Inc}, which is kept free between $18°$ and $87°$. In our analysis using XSPEC, we used the following model configuration:

$$\begin{aligned}
\text{Model borus02} = C_{Ins} * phabs * (borus02 + zphabs \\
* cabs * cutoffpl_1 + f_s * cutoffpl_2 \\
+ mekal + zgauss),
\end{aligned} \tag{25}$$

where $mekal$ is included to compute the soft excess below 1 keV, and $zgauss$ is introduced if there is any emission line signature not included in borus02.

3.4 Results of the X-ray spectral analysis

In this section, we show the results of X-ray spectral fitting on each CT-AGN candidate from Ricci et al., 2015a using both physically motivated models mentioned in Section 3.3, with two versions of MYTorus and one borus02. Table 7 displays the summary of our analysis on the sample using borus02. The best-fit parameters are reported in Table 2 and in A. The plots with X-ray spectral fitting are shown in Figure 13 and B. The background contribution for all these sources is within 20%, unless mentioned otherwise. The tables also report the observed flux and intrinsic luminosity for each source.

MCG-02-12-017

The source was marked as a CT-AGN candidate based on the data of *Swift-XRT* and *Swift-BAT*, with log $N_{H,LOS}$=$24.25^{+1.06}_{-0.46}$ in cm^{-2}. For our analysis, we used the quasi-simultaneous observations of XMM-*Newton* and *NuSTAR*, along with another *NuSTAR* observation taken about 15 months earlier with a longer exposure time of ~ 34 ks. The

Table 2: Summary of best-fit solutions of XMM-Newton and NuSTAR data using different models for MCG-02-12-017

Model:	MyTorus Edge-on	MyTorus Face-on	borus02
χ^2/dof	192/200	192/200	186/198
C_{Ins_1} [a]	$0.88^{+0.11}_{-0.10}$	$0.89^{+0.09}_{-0.08}$	$0.89^{+0.11}_{-0.10}$
C_{Ins_2} [b]	$1.24^{+0.16}_{-0.15}$	$1.28^{+0.12}_{-0.14}$	$1.25^{+0.15}_{-0.17}$
Γ	$1.94^{+0.14}_{-0.14}$	$1.98^{+0.06}_{-0.12}$	$2.11^{+0.13}_{-0.16}$
C_{Tor} [c]	—	—	$1.00^{+*}_{-0.35}$
θ_{Inc} [d]	—	—	49^{+*}_{-*}
$N_{H,z}$ [e]	$0.26^{+0.03}_{-0.03}$	$0.26^{+0.03}_{-0.02}$	$0.27^{+0.03}_{-0.03}$
$N_{H,S}$ [f]	$2.00^{+2.83}_{-1.10}$	$10.0^{+*}_{-9.99}$	$1.98^{+1.07}_{-0.52}$
f_s [g] 10^{-2}	$0.25^{+0.16}_{-0.13}$	$0.17^{+0.09}_{-0.09}$	$0.20^{+0.12}_{-0.11}$
kT [h]	$0.46^{+0.41}_{-0.37}$	$0.48^{+0.29}_{-0.19}$	$0.47^{+0.49}_{-*}$
$F^i_{2-10keV}$	$5.65^{+0.40}_{-0.67}$	$5.59^{+0.44}_{-0.71}$	$5.55^{+0.45}_{-1.76}$
$F^j_{10-40keV}$	$1.57^{+0.11}_{-0.36}$	$1.65^{+0.34}_{-0.41}$	$1.63^{+0.17}_{-0.60}$
$L^k_{2-10keV}$	$4.98^{+2.13}_{-1.52}$	$4.82^{+0.56}_{-0.59}$	$5.17^{+1.89}_{-1.47}$
$L^l_{10-40keV}$	$4.69^{+2.01}_{-1.44}$	$4.27^{+0.51}_{-0.51}$	$3.77^{+1.37}_{-1.07}$

[a] $C_{Ins_1} = C_{FPMA/PN}$ is the cross calibration constant between *NuSTAR* observation of 2014 and XMM-*Newton* observation of 2016.
[b] $C_{Ins_2} = C_{FPMA/PN}$ is the cross calibration constant between *NuSTAR* observation of 2016 and XMM-*Newton* observation of 2016.
[c] Covering factor: fraction of sky covered by the torus, as seen by the nucleus, given by $C_{Tor} = \cos(\theta_{Tor})$.
[d] Inclination angle: angle (in degrees) between the symmetry axis of the torus and the LOS angle
[e] "Line of sight" column density in 10^{24} cm^{-2}.
[f] Average column density from scattering in 10^{24} cm^{-2}.
[g] Fraction of primary emission getting scattered, rather than absorbed by the obscuring material.
[h] Temperature in the thermal component *mekal* in keV.
[i] Flux between 2 and 10 keV in 10^{-13} erg cm^{-2} s^{-1}.
[j] Flux between 10 and 40 keV in 10^{-12} erg cm^{-2} s^{-1}.
[k] Intrinsic luminosity between 2 and 10 keV in 10^{42} erg s^{-1}.
[l] Intrinsic luminosity between 10 and 40 keV in 10^{42} erg s^{-1}.

cross-calibration ratio between XMM-*Newton* and the *NuSTAR* detector for quasi-simultaneous observations is $\sim 75\%$, whereas for the previous NuSTAR observation, this ratio is $\sim 85\%$.

This source is very well fitted (see Table 2 and Figure 13) by all three models. All the physically motivated models are in agreement that the observed LOS column density $N_{\mathrm{H,LOS}} = (0.23 - 0.30) \times 10^{24}$ cm^{-2} is Compton-thin, in disagreement with the Ricci et al., 2015a result. Even when we only used the quasi-simultaneous observations, the LOS column density is consistent with each other's observation having range $N_{\mathrm{H,LOS,qs}} = (0.24 - 0.32) \times 10^{24}$ cm^{-2}. The average torus column density is instead found to be close to or above the Compton-thick threshold by `MYTorus` Edge-On and `borus02` ($N_{\mathrm{H,tor}} = (0.9 - 4.83) \times 10^{24}$ cm^{-2}). The best-fit value of the photon index is found to be in range of Γ=1.94 – 2.11, considering all the models. Estimation of the torus properties, such as covering factor and opening angle in `borus02`, is found to be difficult, because the reflection component is subdominant.

NGC 4180

This target was classified as a CT-AGN candidate based on the data of *Swift-XRT* and *Swift-BAT*, log N_H=24.15$^{+0.27}_{-0.22}$ cm^{-2}. For our analysis, we included only the two *NuSTAR* observations, excluding the *Chandra* observation due to its extremely poor photon statistic (Table 1). We used the Portable Interactive Multi-Mission Simulator[11] to convert the *NuSTAR* spectrum for E>2 keV, and found the predicted count rate (1.56×10^{-3} cts/s) for *Chandra* to be within the error range of the observed count rate ($1.42\pm0.82\times10^{-3}$ cts/s). Moreover, the cross-normalisation ratio between two separate observations (2016 and 2020) of the FPMA detector is $\sim 50\%$, portraying noticeable variability of the source.

The source is very well fitted (see Table 13 and Figure 22) by all models, with models showing consistent results with one other, giving Compton-thick LOS column density $N_{\mathrm{H,LOS}} = (1.25-6.10)\times10^{24}$ cm^{-2} in agreement with the results obtained by Ricci et al., 2015a. Even the average torus column density, which is more accurately constrained by `MYTorus` Edge-On and `borus02` in this case, shows $N_{\mathrm{H,tor}} = (0.66 - 4.56) \times 10^{24}$ cm^{-2}, suggesting a moderate CT nature of the obscuring material as a whole. The best-fit values of photon index are $\Gamma \sim 1.40 - 1.66$, considering all the models. The hard

---

[11]https://cxc.harvard.edu/toolkit/pimms.jsp
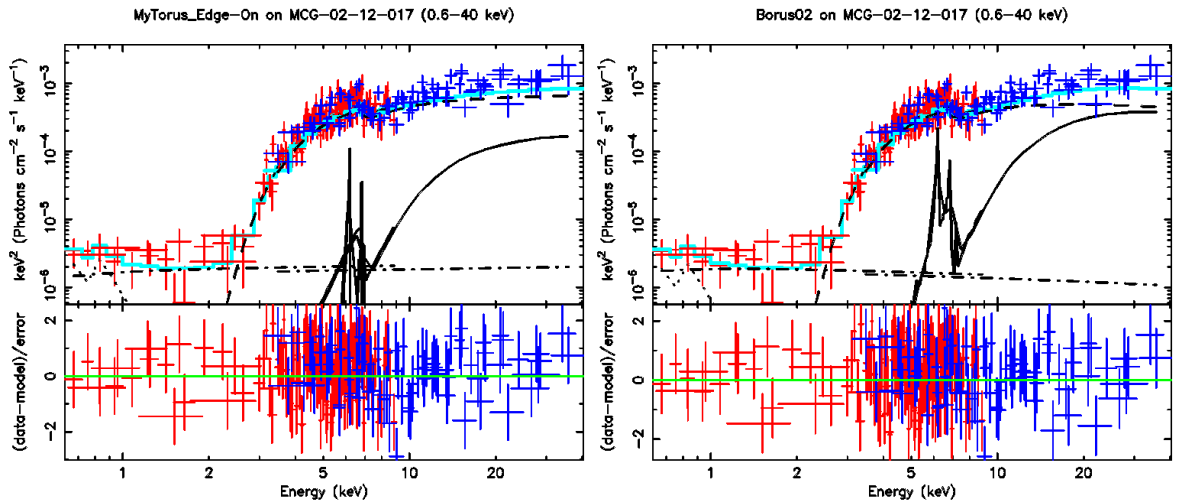
Figure 13: X-ray spectral fitting of decoupled Edge-On `MYTorus` (left) and `borus02` (right) models of MCG-02-12-017 data. In both the plots, the soft X-ray data (from XMM-*Newton*) are marked in red and hard X-ray data (from *NuSTAR*) are marked in blue. The joint best-fit model in both soft and hard X-rays is plotted as a cyan line. The individual model components are shown as black lines as follows: direct power-law emission (dashed), reflected emission (solid), scattered emission (dot-dashed), iron line (solid; in `MYTorus` it is separate, in `borus02` it is included in reflected emission), and mekal (dotted).

index value shows that the models might not be able to properly estimate the direct power-law component contribution in the absence of soft X-ray data, and therefore cannot fully break the $N_{H,LOS}$–Γ degeneracy. For similar reasons, the covering factor and inclination angle also show a large range of uncertainty. However, as shown in Figure 22, the overall spectral emission is dominated by the reflected component over the LOS component. Therefore, from the available data, this source can be identified as a bona fide CT-AGN. However, soft X-ray observations would be required to put stronger constraints on the different obscuring material parameters.

NGC 2788A

This source was marked as a CT-AGN candidate based on the data of *Swift-XRT* and *Swift-BAT*, with log N_H=25.55$^{+*}_{-1.41}$ in cm^{-2}. For our analysis, we have two *NuSTAR* observations (taken in 2019 and 2020; total exposure $\sim$ 51 ks). To cover the $<$ 3 keV energy range, we make use of 12 *Swift-XRT* observations taken from 2008 to 2020[12]. Due to very low spectral counts in soft X-ray ($\sim$ 34 counts; see Table 1), we grouped the spectra from XRT with 1 count/bin and jointly fitted the *Swift-XRT* and *NuSTAR* spectra applying C-statistics over the entire range in `XSPEC`. The cross-calibration variability between *Swift-XRT* and *NuSTAR* detectors fall within $\sim$ 20%.

This source is very well fitted using the physically motivated models (see Table 14 and Figure 20). The results are consistent between all models. The LOS column density $N_{H,LOS} = (1.67 - 2.36) \times 10^{24}$ cm^{-2} shows a CT column density, which validates the result of Ricci et al., 2015a, although with a significantly lower value. In comparison with the average column density of the torus, the best-fit value of `MYTorus` Face-On and `borus02` are close to each other with the range $N_{H,tor} = (1.72 - 22.69) \times 10^{24}$ cm^{-2}, agreeing with the CT nature of the cloud distribution. On these two models, the best-fit value of Γ is around 1.8-1.9. In addition, the `borus02` model best fits the data with an intermediate covering factor, although with large uncertainties ($0.49^{+0.47}_{-0.28}$) and inclination angles in the range $47° - 72°$. In Figure 20, both models show considerable dominance of the reflection component over the LOS component, even more strongly suggesting the CT nature of the source. From the available *NuSTAR* data, this source is confirmed to be a bona fide CT-AGN. However, further observations below 10 keV are needed for a better understanding of the properties of the obscuring material.

---

[12]We obtained a joint spectrum using the tool available at www.swift.ac.uk/user_objects/

NGC 1106

This candidate was marked as a CT-AGN based on the data of *Swift-XRT* and *Swift-BAT*, which suggest a log N_H=24.25$^{+0.29}_{-0.17}$ in cm^{-2}. For our analysis, we used a XMM-*Newton* observation (taken in 03/2019; $\sim$ 33 ks) and *NuSTAR* observations (taken in 02-2019 and 09-2020; total exposure $\sim$ 41 ks). The cross-calibration ratio between XMM-*Newton* and *NuSTAR* detectors is 1.4.

This source is very well fitted (see Table 15 and Figure 21). All three models show consistent results. The LOS column density $N_{H,LOS} = (2.83 - 5.73) \times 10^{24}$ cm^{-2} shows a CT column density, which validates the result of Ricci et al., 2015a. The torus average column density is $N_{H,tor} = (1.34 - 7.98) \times 10^{24}$ cm^{-2}, in agreement with the CT nature of the torus. It is also interesting to note that `borus02`, which has a better reduced χ^2 value ($\sim$ 1.04) and a value of Γ ($\sim$ 1.92) closer to the AGN average (Marchesi et al., 2016), also estimates that the LOS column density is in agreement with the average torus column density, suggesting that the obscuring material is likely uniform (see Table 15). In addition, the `borus02` model gives a high covering factor ($0.87^{+0.11}_{-0.24}$), and moderate inclination angle in the range of $28° - 74°$. Figure 21 shows how the reflection component is dominant over the direct power law. From the above analysis, this source can be counted as a *bona fide* CT-AGN.

ESO406-G004

This target was marked as a CT-AGN candidate based on the data of *Swift-XRT* and *Swift-BAT*, which suggest a log N_H=24.74$^{+*}_{-0.55}$ in cm^{-2}. For our analysis, we have a *Chandra* observation with very low exposure ($\sim$ 5.1 ks) and only 25 spectral counts in soft X-rays. Furthermore, even though the two archival *NuSTAR* observations have a much higher exposure time (total $\sim$ 60 ks), the source count statistic is significantly lower than that of the other sources ($\sim$ 747 net counts in 2016 and $\sim$ 206 net counts in 2020; see Table 1). Due to such low spectral counts, we used C-statistics to fit the data after binning with 1 count/bin in *Chandra*, and 10 counts/bin and 20 counts/bin on *NuSTAR* observations of 2020 and 2016, respectively. It is also noticeable that the observations were taken after large gaps ($\sim$ 4 years), and the cross-calibration ratio between ACIS (of *Chandra*) and FMPA (of *NuSTAR*) detectors shows large variability: $\sim 1.3 - 1.7$. Furthermore, in the *NuSTAR* observation of June 2020, the background-

noise contribution on the spectral signal is $\sim 30\% - 40\%$, whereas the other data sets show contributions of $< 20\%$.

This source is very well fitted by all the models. All three models show consistent results. The LOS column density for this source of $N_{H,LOS} = (0.59 - 1.28) \times 10^{24}$ cm^{-2} shows a mostly Compton-thin column density, contrary to the result of Ricci et al., 2015a. The decoupled MYTorus estimates $N_{H,tor} = (0.13 - 2.03) \times 10^{24}$ cm^{-2} and borus02 estimates, with a large error range, $N_{H,tor} = (0.11 - 5.01) \times 10^{24}$ cm^{-2}. Overall, the fit suggest mostly Compton-thin clouds with upper bounds crossing the CT threshold. Due to the lack of XMM-$Newton$ data, it is likely that the low-statistic in the soft X-ray, along with a fairly low statistic in the hard X-rays, make it difficult to properly disentangle the Γ–$N_{H,LOS}$ degeneracy. For similar reasons, we find that borus02 computes a low covering factor (best-fit value ~ 0.10) and a small inclination angle ($18°$) with a high or unconstrained error range.

Furthermore, we noticed a significant cross-calibration variability for the two $NuSTAR$ observations (see Table 16). We therefore also carried out a comparative study of the $NuSTAR$ observations of this source taken in May 2016 and June 2020 in order to check flux and LOS column density variability (following the approach of Marchesi et al., 2022; Pizzetti et al., 2022; Torres-Albà et al., 2023b); these are listed in Table 3. The cross-calibration flux value is measured with respect to the $Chandra$ observation of June 2012. We fixed all the other parameters for these two $NuSTAR$ observations to the best-fit values, and only kept the $N_{H,LOS}$ and flux free to vary. We studied the variability by fixing one of the two parameters and leaving the other free to vary, and finally compared the values by varying both of them. We find that the $N_{H,LOS}$ increases $\sim 53\%$ from 2016 to 2020 and the flux is significantly increased ($\sim 230\%$) in the 2020 observation with respect to the 2016 one. However, from the reduced C-stat value, we find that the residual (data-model) worsens if we vary only the LOS column density; whereas fixing the $N_{H,LOS}$ does not significantly change the fit with respect to varying both flux and column density for the different $NuSTAR$ epochs. This indicates that the variability observed between the two $NuSTAR$ observations can be explained within a pure luminosity variability scenario, while the fit improvement is not significant when allowing the LOS column density to vary.

Table 3: Flux and column-density variability of ESO406-G004 from *NuSTAR* observations using borus02

Parameter	Fixing only $N_{H,LOS}$	Fixing only C_{Ins}	Varying both
$C_{Ins,NuS1}$ [a]	$0.77^{+0.15}_{-0.12}$	$0.84^{+0.22}_{-0.16}$	$0.82^{+0.18}_{-0.14}$
$C_{Ins,NuS2}$ [b]	$0.35^{+0.08}_{-0.07}$	"	$0.25^{+0.13}_{-0.08}$
$N_{H,LOS,NuS1}$ [c]	$0.82^{+0.15}_{-0.12}$	$0.88^{+0.21}_{-0.16}$	$0.86^{+0.17}_{-0.14}$
$N_{H,LOS,NuS2}$ [d]	"	$1.88^{+0.78}_{-0.45}$	$0.58^{+0.29}_{-0.21}$
C-Stat/d.o.f.	84/93	92/93	82/92

[a]Cross-calibration value from FPMA detector, observed in 2020
[b]Cross-calibration value from FPMA detector, observed in 2016
[c]LOS column density from FPMA detector in 10^{24} cm^{-2}, observed in 2020
[d]LOS column density from FPMA detector in 10^{24} cm^{-2}, observed in 2016

2MASX J20145928+2523010

This candidate was also classified as a CT-AGN based on the data of *Swift-XRT* and *Swift-BAT*, which suggest log N_H=24.42$^{+0.20}_{-0.17}$ in cm^{-2}. For our analysis, we have *Chandra* (taken in 12/2018) and XMM-*Newton* (taken in 11/2017) spectra with excellent photon statistics in the $0.6 - 10$keV energy range (total spectral counts $\sim$ 9k). Even in hard X-rays, the two archival *NuSTAR* observations (taken in May 2017 and April 2020) have a high exposure time and net spectral counts (total $\sim$ 3.6k). It is worth noting that for the joint *NuSTAR* and XMM-*Newton* observation taken in 2017, we measure a cross-calibration ratio of < 1.4. However, the flux values of the 2018 *Chandra* and the 2020 *NuSTAR* observations are almost twice ($\sim 1.93 - 2.15$) that of the 2017 XMM-*Newton* observation. There is also significant flux variability (factor of 0.77) between the *NuSTAR* and XMM-*Newton* observations taken only 6 months apart.

This source is very well fitted by all the models (see Table 17). All three models show consistent results. The LOS column density for this source is $N_{H,LOS}$ = $(1.86 - 2.29) \times 10^{22}$ cm^{-2}[13], with a fairly low LOS column density just above the standard 10^{22} cm^{-2} threshold used to classify obscured AGN. Such a result is in strong disagreement with that of Ricci et al., 2015a. Even the average column density of the torus is $N_{H,tor} = (9.07 - 28.66) \times 10^{22}$ cm^{-2}, that is, Compton-thin. The decoupled `MYTorus` model shows a better estimate of the photon index $\sim 1.69 - 1.89$ compared to `borus02`, in terms of consistency with the expected value. Due to strong domination of the intrinsic power law over the reflection component in the hard X-ray regime, `borus02` fails to compute the covering factor and inclination angle properly. Noticing the absence of a reflection component, we also tested a simple phenomenological model using photoelectric absorption and a power law above 3 keV. We find $\chi^2_\nu \sim 0.99$ with $N_{H,LOS}$ and Γ within the error range of `borus02` results, considering a direct power law along the LOS. Therefore, for the similarity of the results and to maintain consistency with the other sources, we have shown the results of physically motivated torus models only in Table 17.

Furthermore, for this source, we also find a cross-calibration variability for different *NuSTAR* observations. Therefore, in Table 4 we show a comparative study of the *NuSTAR* observations of this source taken in May 2017 and April 2020, which was carried out in order to check for flux and LOS column density variability; the table

---

[13]In Table 17, the LOS column density is shown in 10^{22} cm^{-2}

Table 4: Flux and column-density variability of 2MASX J20145928+2523010 from $NuSTAR$ observations using borus02

Parameter	Fixing only $N_{H,LOS}$	Fixing only C_{Ins}	Varying both
$C_{Ins,NuS1}$[a]	$1.23^{+0.05}_{-0.04}$	$1.53^{+0.07}_{-0.07}$	$1.25^{+0.07}_{-0.05}$
$C_{Ins,NuS2}$[b]	$1.94^{+0.09}_{-0.09}$	”	$1.94^{+0.09}_{-0.09}$
$N_{H,LOS,NuS1}$[c]	*	$5.63^{+1.96}_{-1.78}$	$0.33^{+1.61}_{-*}$
$N_{H,LOS,NuS2}$[d]	”	*	*
$\chi^2/d.o.f.$	558/587	645/587	558/586

[a]Cross-calibration value from FPMA detector, observed in 2017
[b]Cross-calibration value from FPMA detector, observed in 2020
[c]LOS column density from FPMA detector in 10^{22} cm^{-2}, observed in 2017
[d]LOS column density from FPMA detector in 2020 is unconstrained, represented as *

is similar to Table 3. The cross-calibration value is measured with respect to the XMM-*Newton* observation of November 2017. Here, we also see the reduced χ^2 value does not show any significant change when fixing only LOS column density, but the $\chi^2/d.o.f.$ increases and worsens the fit when we fix the cross-calibration parameter only. Therefore, similarly to the previous case, the observed flux change for this source can also be explained by the intrinsic luminosity variability.

ESO138-G001

Table 5: Best-fitting parameters of the different emission lines on ESO138-G001, using different torus models.

Lines	MyTorus	MyTorus	borus02
	Edge-on	Face-on	
EW of Mg XI	$0.10^{+0.01}_{-0.01}$	$0.09^{+0.01}_{-0.01}$	$0.10^{+0.01}_{-0.01}$
Intensity of Mg XI 10^{-5}	$0.66^{+0.06}_{-0.06}$	$0.66^{+0.06}_{-0.06}$	$0.67^{+0.06}_{-0.06}$
EW of S XV	$0.10^{+0.02}_{-0.02}$	$0.10^{+0.02}_{-0.02}$	$0.09^{+0.02}_{-0.01}$
Intensity of S XV 10^{-5}	$0.23^{+0.05}_{-0.05}$	$0.23^{+0.05}_{-0.05}$	$0.22^{+0.05}_{-0.05}$
EW of Si XIII	$0.07^{+0.02}_{-0.01}$	$0.07^{+0.01}_{-0.01}$	$0.07^{+0.01}_{-0.01}$
Intensity of Si XIII 10^{-5}	$0.28^{+0.04}_{-0.04}$	$0.28^{+0.04}_{-0.04}$	$0.28^{+0.04}_{-0.04}$

(1) We summarise here the details of the three most prominent emission lines in Figure 25 of joint XMM-*Newton*–*NuSTAR* spectra following the publications- De Cicco et al., 2015a; Piconcelli et al., 2011a.
(2) Equivalent width (EW) of the lines are shown in keV. Normalisation of line components are shown in photons/cm^{-2} s^{-1}.

This source was marked as a CT-AGN based on the data of XMM-*Newton* and *Swift-BAT*, which suggest log N$_H$=25.25$^{+*}_{-0.31}$ cm^{-2}. For our analysis, we used XMM-*Newton* and *NuSTAR* observations, both having excellent count statistics ($\sim 45k$ counts in the

$0.5 - 10$ keV and $\sim 12.7k$ counts in the $3 - 50$ keV band, respectively). The cross-calibration ratio of the *NuSTAR* detector on XMM-*Newton* for the source is ~ 1.15.

The fit is worse (reduced $\chi^2 \sim 1.33 - 1.45$; see Table 18 and Figure 25) than those measured for the other sources. The models are better fitted in the soft X-rays when adding all the emission lines listed in Table 5 following the previous works of De Cicco et al., 2015b; Piconcelli et al., 2011b. All three models are almost consistent with each other.

Studying all the models, the LOS column density $N_{H,LOS} = (0.30 - 0.40) \times 10^{24}$ cm^{-2} shows Compton-thin clouds, which differs from the results of Ricci et al., 2015a. In comparison with the average column density of the torus, the decoupled MYTorus (Face-On) and borus02 estimate $N_{H,tor} = (2.45 - 10.43) \times 10^{24}$ cm^{-2}, supporting a CT average column density scenario. It is also noticeable that the borus02 gives a comparatively better reduced χ^2 value (~ 1.33) and $\Gamma \sim 1.95 - 1.99$. In addition, the borus02 model further computes a moderate-to-high covering factor $(0.68 - 0.83)$, but low inclination angle with unconstrained error. We also had to include an extra Gaussian line profile for the fluorescent lines in the models to account for a broader line profile than the one implemented within the torus models. The high $N_{H,tor}$ and high covering factor show that the reprocessed emission is significantly dominant with a prominent Fe line.

3.5 Discussion

This paper reports the analysis of seven CT-AGN candidates: MCG-02-12-017, NGC 2788A, NGC 4180, 2MASX J20145928+2523010, ESO406 G-004, NGC 1106, and ESO138 G-001 from the 100 month Palermo BAT sample. For the first time, we analysed the *NuSTAR* spectra of these sources using MYTorus and borus02.

3.5.1 Clumpy torus and variability

The LOS column density and average torus column density of three out of the seven sources in our sample (NGC 4180, NGC 2788A and NGC 1106) are found to be in agreement within their uncertainty ranges and above the Compton-thick threshold $(> 10^{24}$ cm$^{-2})$. For ESO406 G-004, the column densities are compatible within their
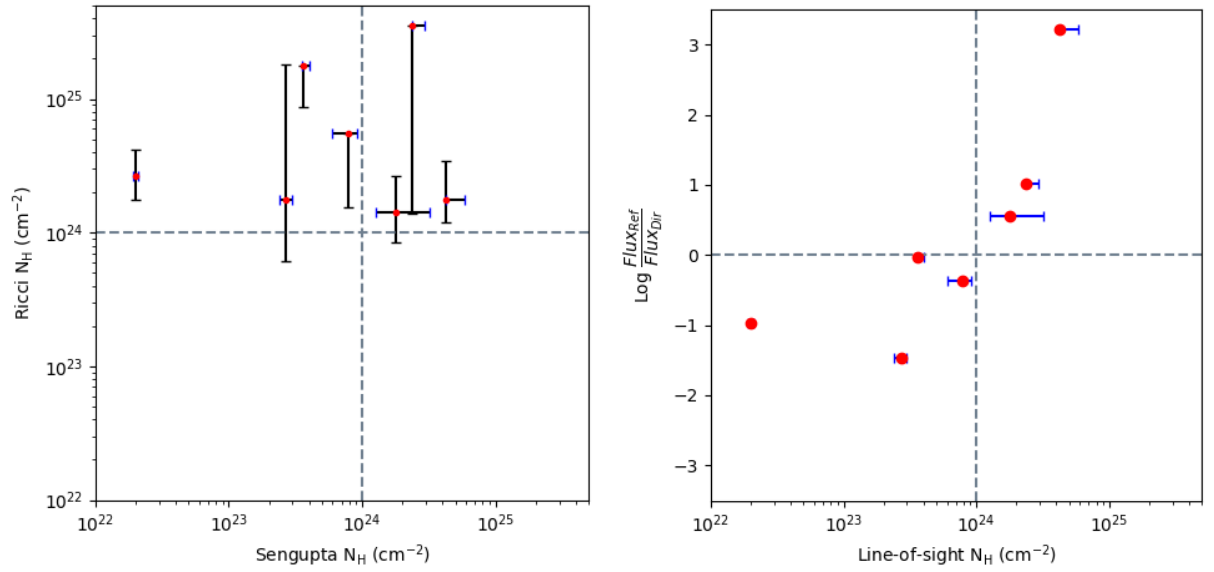
Figure 14: Comparisons of X-ray spectral properties of the seven sources. *Left:* Comparison of the LOS column density values (as red dot) and its uncertainty values from Ricci et al., 2015a (black markers) with those of the present study (blue markers). The horizontal and vertical grey-dashed lines classify the CT column density threshold. *Right*: Observed (i.e. non-absorption corrected) flux ratio of the reflected component over the direct transmitted component in the 2-10 keV band for each source of our sample, plotted along the LOS column density on the X-axis.

error range, but fall in the Compton-thin range. The remaining three sources (MCG-02-12-017, 2MASX J20145928+2523010, ESO138 G-001) show incompatible column densities, hinting at a clumpy nature of the obscuring medium. In the left panel of Figure 14, we compare the LOS column density results of our sample using `borus02` along with the results of Ricci et al., 2015a. All seven candidates from Ricci et al., 2015a lie above the CT threshold with large uncertainties, whereas the use of *NuSTAR* data instead of *Swift-BAT* reduces the error bar significantly, displaying only three sources above the CT line, leading to the confirmation of only three sources as CT. The right panel of Figure 14 shows a clear trend of the flux ratio at 2-10 keV as a function of $N_{H,LOS}$: the larger the LOS column density, the stronger the flux of reflected continuum over direct continuum.

Furthermore, in Figure 15, we show the distribution of $N_{H,LOS}$ and $N_{H,avr}$ of our sample AGN along with all the previous results of the CT-AGN candidates analysed by the Clemson-INAF group. The $\frac{N_{H,LOS}}{N_{H,avr}}=1$ line is shown as a brown-dashed line and 1:2 and 2:1 ratios are shown as pink dot-dashed lines to classify the sources with a comparatively homogeneous torus when they produce a column density ratio of within $\sim 0.5 - 2.0$. Only 12 sources ($\sim 22\%$ of the sample) fall within this region. The remaining 43 sources ($\sim 78\%$ of the sample) instead show significant inhomogeneity, and considering the error bar at the $3\,\sigma$ level, 34 sources ($\sim 62\%$) fall completely outside the given area. This is also a natural outcome of the CCA scenario, in which the multi-phase clouds continuously rain through the meso scale, thus recurrently obscuring the LOS. The residual gas experiencing less inelastic collisions (and therefore less angular momentum cancellation) tends to accumulate in a clumpy torus-like structure at this scale (Gaspari et al., 2017). Therefore, based on all previous results, in addition to those presented in this work, we can conclude that most of these obscured active galaxies have a significantly clumpy torus ($\sim 78\%$ of the total population). It is also important to note that the two column densities are significantly uncorrelated. By statistically analysing the parameters for all 55 sources, their Pearson correlation coefficient[14] yields $\rho \approx 0.003$ (similar to the value of -0.017 obtained by Torres-Albà et al., 2021). This suggests that a bona fide CT-AGN is not necessarily likely to be made of CT-torus. As supported by hydrodynamical simulations (see e.g. Gaspari et al., 2020), a realistic torus is a composition of multi-phase and multi-scale clouds, whose integral (e.g. density) can substantially change along each LOS. The non-correlation we find is even consistent

---

[14]$\rho \approx 1$ or $\rho \approx -1$ for strong linear correlation or anti-correlation, respectively, and $\rho \approx 0$ for lack of correlation.

with the results of Zhao et al., 2021, in which a sample of approximately 100 local Compton-thin AGN were studied (along with CT-AGN) using high-quality *NuSTAR* data along with soft X-ray data, with the authors showing that similar values of $N_{H,tor}$ ($\sim 1.4 \times 10^{24}$ cm^{-2}) are found for different $N_{H,LOS}$. In Figure 15, we increased our sample by including 74 sources from Zhao et al., 2021, marked as small grey circles. All of these sources have $N_{H,LOS}$ ¿ 10^{22} cm^{-2}. We find that the total percentage of homogeneous tori comes down to $\sim 16\%$ of the enlarged sample, including the Compton-thin sources. By calculating the Pearson correlation coefficient between the column densities with this enlarged sample, we find a similar non-correlation scenario (~ -0.012), as obtained before including these Compton-thin AGN.

Through multi-epoch X-ray monitoring of these obscured sources, we can study the LOS column density variability and confirm the inhomogeneity of the circumnuclear cloud distribution. Some previous observations have reported extreme variability, and even a 'changing-look' nature from CT to Compton-thin or vice versa; for example, for NGC 7582 (Bianchi et al., 2009; Rivers et al., 2015), IC 751 (Ricci et al., 2016), and NGC 1358 (Marchesi et al., 2022), among others. In our sample, 2MASX J20145928+2523010 shows strong variability over a three-year time span. On the other hand, ESO138 G-001 shows almost no variability after a seven-year observational gap (Section 3.4). In order to obtain a clearer picture of the variability of such sources (i.e. clumpiness) over timescales from weeks to years, we would need follow-up observations with longer exposures on each source. Nevertheless, to properly assess the complex cloud distribution within the torus of each of these obscured sources, a joint analysis of both X-ray and mid-infrared (MIR) is required at multiple epochs Berta et al., 2013; Buchner et al., 2019; Esparza-Arredondo et al., 2021. We will consider this in future work.

3.5.2 Updated census of local CT-AGN candidates

Out of the seven 100 month BAT candidate CT-AGN analysed in this work, we confirm three bona fide CT-AGN. This brings the total number of CT-AGN at $z < 0.05$ to 35[15] Georgantopoulos and Akylas, 2019; Kammoun et al., 2020; Koss et al., 2016; Marchesi et al., 2018; Marchesi, Ajello, Zhao, Comastri, et al., 2019; Marchesi, Ajello, Zhao, Marcotulli, et al., 2019; Oda et al., 2017; Tanimoto et al., 2019a; Torres-Albà

---

[15]https://science.clemson.edu/ctagn/
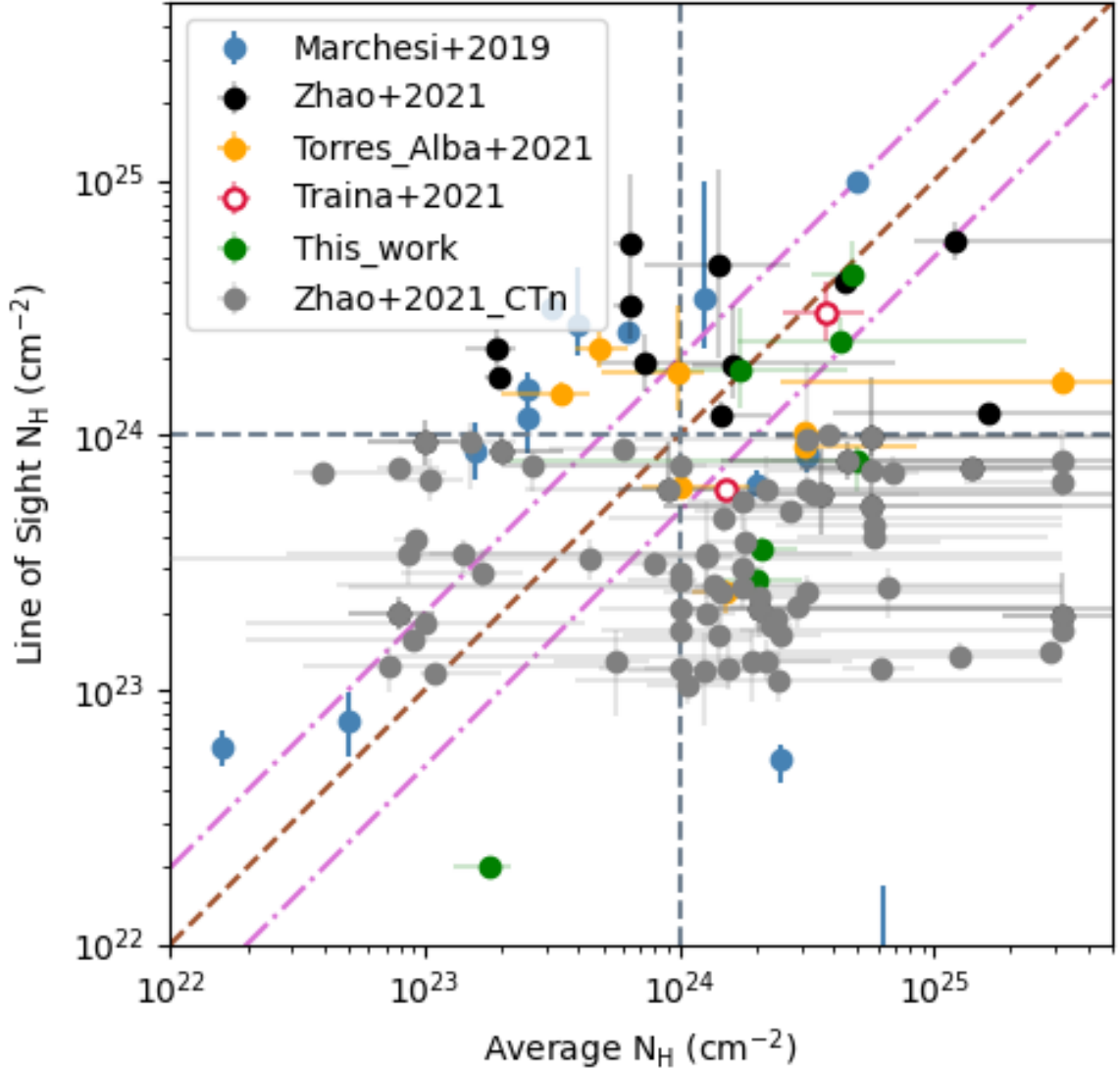
Figure 15: We show the census of the previous results of CT-AGN candidates (selected from Ricci et al., 2015a) having z< 0.01 with archival *NuSTAR* data, analysed by the Clemson-INAF group: Marchesi et al., 2018, Zhao et al., 2021, Torres-Albà et al., 2021, Traina et al., 2021 and including our analysis. The sample of these CT-AGN candidates are marked as large circles. In the parameter space of average vs LOS column density, grey-dashed lines drawn horizontally and vertically marks the CT column density threshold. The brown-dashed diagonal line (i.e the "Line of Homogeneity") identifies an homogeneous obscuring material distribution. The region within the pink dot-dashed lines is used to classify the number of sources with homogeneous torus. We also included the sample of 74 Compton-Thin sources from Zhao et al., 2021, shown as small grey circles.

et al., 2021; Traina et al., 2021; Zhao et al., 2020, 2021. In the left panel of Figure 15, we study 55 CT-AGN candidates analysed by our Clemson-INAF group in the parameter space of observed $N_{H,LOS}$ and computed $N_{H,avr}$. Of these, 27 ($\sim 50\%$) have $N_{H,LOS} > 10^{24}$ cm^{-2}.

The total percentage of confirmed CT-AGN from *Swift-BAT* (i.e., hard X-ray flux) selection within the local Universe (z< 0.05) is $\sim 8\%$ (35/414), which is much lower than the CT-AGN fraction predicted by the population synthesis models. Our results also update the CT-AGN fraction within the distance $z < 0.01$ to ($\sim 22\% \pm 5.9)\%$[16] (11 CT-AGN out of 50 AGN; Torres-Albà et al., 2021 showed 10 CT-AGN). Figure 16 shows the fraction of CT-AGN from the total AGN population in the 100 month *Swift-BAT* catalogue. The fraction drops when moving towards higher redshifts ($z > 0.01$) because the CT-AGN sources become too faint to be detected by *Swift-BAT* (Koss et al., 2016).

3.5.3 Comparison with XClumpy results

Recently, Tanimoto et al., 2022 (T22 hereafter) published the results of an X-ray spectral analysis with the `XCLUMPY` model (Tanimoto et al., 2019b) of the sources analysed in this work (as part of a larger sample of low-redshift, heavily obscured AGN). The `XCLUMPY` model considers the torus as clumpy and inhomogeneous, assuming a power-law distribution along the radial axis and a Gaussian distribution along the vertical axis of the torus. Below, we compare the results of these latter authors with those obtained using `MYTorus` decoupled and `borus02` in this work.

- **MCG-02-12-017:** For this source, T22 used the quasi-simultaneous observations of XMM-*Newton* and *NuSTAR* (ObsID: 60101015002). The LOS column density and photon index, at 90% confidence, are $N_{H,LOS} = (0.21 - 0.28) \times 10^{24}$ cm^{-2} and $\Gamma = 1.53 - 1.88$, respectively. The results are very consistent with ours (see Table 2). Similarly, the computed equatorial (average) column density mostly falls within the limits of the error range ($N_{H,eq} = (1.16 - 9.59) \times 10^{24}$ cm^{-2}) of our analysis, which is also in agreement with our prediction of the clumpy nature of the torus. Overall, for this source, the *XClumpy* model is in agreement with the decoupled `MYTorus` and `borus02` models.

---

[16]Standard error in binomial distribution.
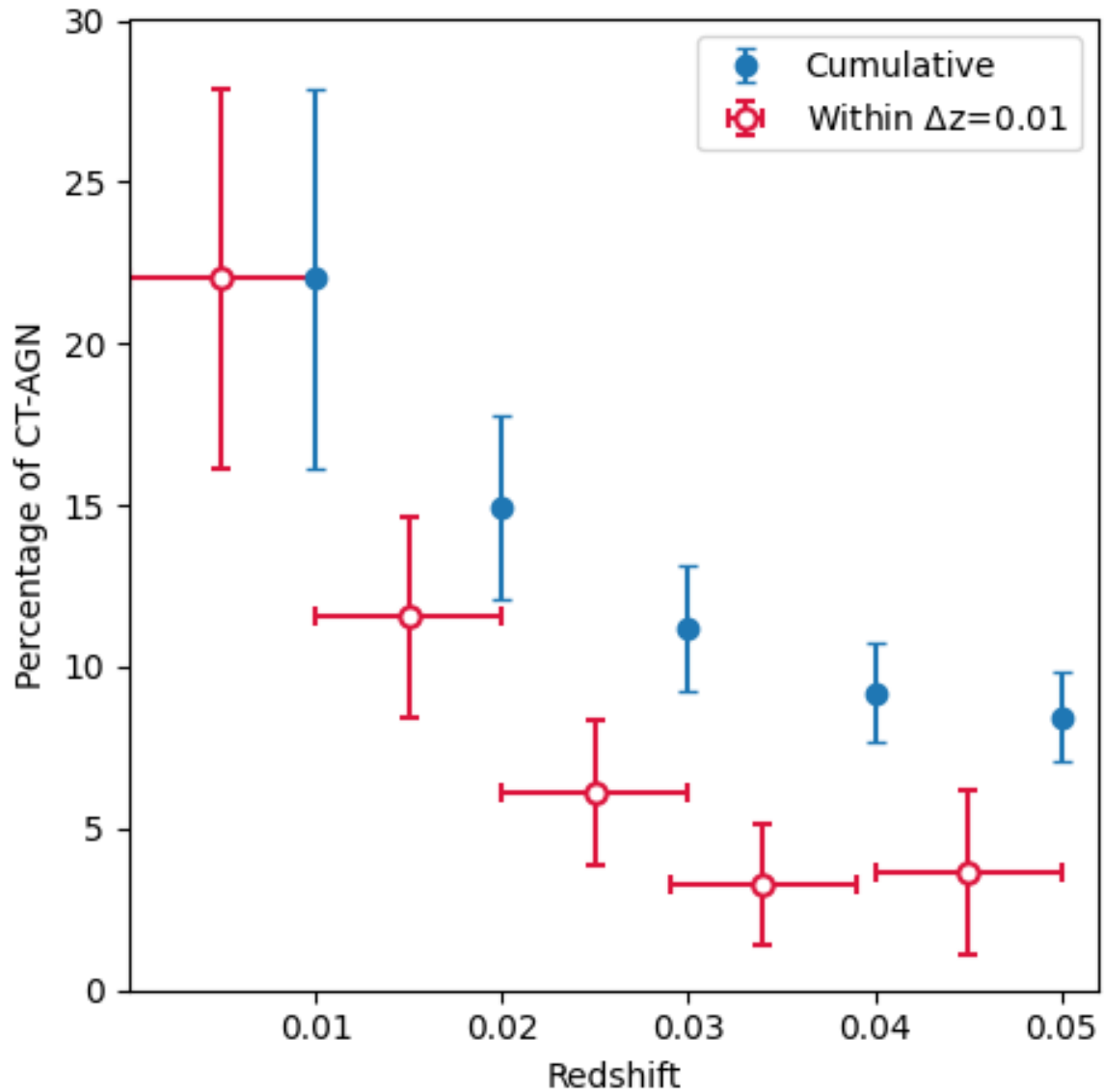
Figure 16: Evolution of observed CT-AGN fraction from the 100 month *Swift-BAT* catalogue as a function of redshift (for z< 0.05). The red points represent the CT-AGN fraction within the given redshift bin of 0.01 and blue points show the cumulative value of the fraction within the given redshift. The displayed error bars are in binomial statistics. This figure is updated from the CT-AGN fraction plot of Torres-Albà et al., 2021.

Table 6: Comparisons of best-fit values for Γ (photon index) and torus column density using the torus models

Models:	borus02		MYTorus (Decoupled Edge-On)		XCLUMPY	(from T22)
Sources	Γ	$N_{\mathrm{H,torus}}$ $(10^{24}\ \mathrm{cm}^{-2})$	Γ	$N_{\mathrm{H,S}}$ $(10^{24}\ \mathrm{cm}^{-2})$	Γ	$N_{\mathrm{H,eq}}$ $(10^{24}\ \mathrm{cm}^{-2})$
MCG-02-12-017	$2.11^{+0.13}_{-0.16}$	$1.98^{+1.07}_{-0.52}$	$1.94^{+0.14}_{-0.14}$	$2.00^{+2.83}_{-1.10}$	$1.54^{+0.18}_{-0.45}$	$9.59^{+*}_{-8.43}$
NGC4180	$1.55^{+0.44}_{-*}$	$1.74^{+2.82}_{-1.08}$	$1.66^{+0.39}_{-*}$	$1.97^{+0.33}_{-0.73}$	$1.61^{+0.05}_{-0.17}$	$4.10^{+*}_{-2.18}$
NGC2788A	$1.95^{+0.32}_{-0.31}$	$4.26^{+18.43}_{-2.54}$	$1.56^{+0.20}_{-*}$	$1.25^{+0.24}_{-0.60}$	$1.67^{+0.11}_{-0.08}$	$2.37^{+2.20}_{-0.19}$
NGC1106	$1.92^{+0.44}_{-0.35}$	$4.83^{+*}_{-1.38}$	$1.40^{+0.00}_{-*}$	$1.46^{+0.18}_{-0.12}$	$1.67^{+0.16}_{-0.30}$	$8.17^{+1.63}_{-1.51}$
ESO406-G004	$1.42^{+0.02}_{-*}$	$4.97^{+*}_{-4.80}$	$1.48^{+0.30}_{-*}$	$0.49^{+1.11}_{-0.62}$	$1.10^{+0.28}_{-*}$	$0.64^{+0.55}_{-0.23}$
2MASX J20145928+2523010	$1.52^{+0.05}_{-0.04}$	$0.18^{+0.05}_{-0.04}$	$1.79^{+0.10}_{-0.10}$	$0.12^{+0.04}_{-0.03}$	$1.42^{+0.03}_{-0.09}$	$1.01^{+0.89}_{-0.67}$
ESO138-G001	$1.98^{+0.01}_{-0.03}$	$10.35^{+0.08}_{-0.08}$	$1.53^{+0.05}_{-0.05}$	$1.47^{+0.60}_{-0.49}$	$1.45^{+0.03}_{-0.06}$	$5.34^{+1.53}_{-3.66}$

- **NGC 4180:** For this source, T22 used the observations of *Chandra* and *NuSTAR* (ObsID: 60201038002). The LOS column density and photon index, at the 90% confidence level, are $N_{H,LOS} = (0.68 - 3.75) \times 10^{24}$ cm^{-2} and $\Gamma = 1.44 - 1.66$, respectively. The results are consistent with the decoupled Face-ON `MYTorus` and `borus02` results (see Table 13). Similarly, the computed equatorial (average) column density mostly falls within the range ($N_{H,eq} = (1.92 - 4.10) \times 10^{24}$ cm^{-2}) computed in our analysis, which is also in agreement with our prediction of the clumpy nature of the torus. Even though we only used *NuSTAR* data on this source in our analysis, the results of the `MYTorus` and `borus02` model are still in agreement with the *XClumpy* results.

- **NGC 2788A:** For this source, T22 used the observations of *Suzaku* (obsID: 710007010) and *NuSTAR* (ObsID: 60469001002). The LOS column density and photon index, at the 90% confidence level, are $N_{H,LOS} = (1.55 - 2.83) \times 10^{24}$ cm^{-2} and $\Gamma = 1.59 - 1.78$, respectively. The results are very consistent with our results (see Table 14), even though we used *Swift-XRT* instead of *Suzaku* at energies E< 10 keV. The computed equatorial (average) column density also falls within the range ($N_{H,eq} = (2.18 - 4.57) \times 10^{24}$ cm^{-2}) of our analysis. Even for the covering factor measurement, *XClumpy* estimates $\theta_{Tor} = 19° - 46°$, which significantly narrows the error range and falls within the `borus02` computed range of $\theta_{Tor} = 16° - 78°$. Also, while computing the inclination angle $\theta_{Inc} = 62° - 85°$, the values can be considered to be in agreement within the uncertainties with the `borus02` fitting ($47° - 72°$). Overall, for this source, the results obtained using the *XClumpy* model can be regarded as consistent with those obtained using the decoupled `MYTorus` and `borus02` ones.

- **NGC 1106:** For this source, T22 used the observations of XMM-*Newton* and *NuSTAR* (ObsID: 60469002002). The LOS column density and photon index, at 90% confidence, are found to be $N_{H,LOS} = 3.45 - 4.29 \times 10^{24}$ cm^{-2} and $\Gamma = 1.37 - 1.83$, respectively. These results are consistent with our results (see Table 15). On the other hand, the computed equatorial (average) column density falls in the upper limits of the error range ($N_{H,eq} = (6.66 - 9.80) \times 10^{24}$ cm^{-2}) compared to our analysis. Regarding the computation of the inclination angle $\theta_{Inc} = 60° - 77°$ and covering factor $\theta_{Tor} = 14° - 31°$, the results of T22 fall within the large confidence range of our analysis ($\theta_{Inc} = 28° - 74°$ and $\theta_{Tor} = 11° - 51°$). It is noticeable that the error ranges are significantly reduced while using *XClumpy*. Nevertheless, for this source, the *XClumpy* model results are compatible with

Table 7: Best-fit `borus02` parameters for the sample

Sources	Γ	$N_{\mathrm{H,LOS}}$	$N_{\mathrm{H,torus}}$	C_{Tor}	θ_{Inc}
		$(10^{24}~\mathrm{cm}^{-2})$	$(10^{24}~\mathrm{cm}^{-2})$		(Degees)
MCG-02-12-017	$2.11^{+0.13}_{-0.16}$	$0.27^{+0.03}_{-0.03}$	$1.98^{+1.07}_{-0.52}$	$1.00^{+*}_{-0.35}$	49^{+*}_{-*}
NGC4180	$1.55^{+0.44}_{-*}$	$1.78^{+1.40}_{-0.51}$	$1.74^{+2.82}_{-1.08}$	$0.88^{+*}_{-0.77}$	49^{+12}_{-*}
NGC2788A	$1.95^{+0.32}_{-0.31}$	$2.34^{+*}_{-0.58}$	$4.26^{+18.43}_{-2.54}$	$0.49^{+0.47}_{-0.28}$	63^{+9}_{-16}
NGC1106	$1.92^{+0.44}_{-0.35}$	$4.79^{+*}_{-1.96}$	$4.83^{+*}_{-1.38}$	$0.87^{+0.11}_{-0.24}$	37^{+37}_{-9}
ESO406-G004	$1.42^{+0.02}_{-*}$	$0.79^{+0.04}_{-0.12}$	$4.97^{+*}_{-4.80}$	0.10^{+*}_{-*}	18^{+69}_{-*}
2MASX J20145928+2523010	$1.52^{+0.05}_{-0.04}$	$0.02^{+0.00}_{-0.00}$	$0.18^{+0.04}_{-0.05}$	$1.00^{+*}_{-0.23}$	18^{+*}_{-*}
ESO138-G001	$1.98^{+0.01}_{-0.03}$	$0.47^{+0.07}_{-0.06}$	$10.35^{+0.08}_{-0.08}$	$0.80^{+0.03}_{-0.12}$	18^{+*}_{-*}

those obtained using the decoupled `MYTorus` and `borus02` models.

- **ESO406 G-004:** For this source, T22 used the observations of *Swift-XRT* (ObsID: 00081420001) and *NuSTAR* (ObsID: 60161799002). The LOS column density and photon index, at the 90% confidence level, are found to be $N_{\mathrm{H,LOS}} = (0.38 - 6.34) \times 10^{24}~\mathrm{cm}^{-2}$ and $\Gamma = 1.10 - 1.38$, respectively. As we used *Chandra* and both available *NuSTAR* data, our results show better constraints (see Table 16) on this source compared to the results of T22. However, the computed equatorial (average) column density mostly falls within the range $(N_{\mathrm{H,eq}} = (0.41 - 1.19) \times 10^{24}~\mathrm{cm}^{-2})$ of our analysis. The *XClumpy* model is compatible with decoupled `MYTorus` and `borus02` results.

- **2MASX J20145928+2523010:** For this source, T22 used the observations of XMM-*Newton* and *NuSTAR* (ObsID: 60201032002). For the LOS column density and photon index, at 90% confidence, T22 find $N_{\mathrm{H,LOS}} = (0.01 - 0.03) \times 10^{24}~\mathrm{cm}^{-2}$ and $\Gamma = 1.33 - 1.45$, respectively. The results of $N_{\mathrm{H,LOS}}$ show consistency with our results, but the Γ value is much lower than provided by `MYTorus` and `borus02` (see Table 17). However, the computed equatorial (average) column density falls

within the range ($N_{H,eq} = (0.34 - 1.90) \times 10^{24}$ cm^{-2}) of our analysis, which is also in agreement with our prediction of clumpy torus clouds. Overall, for this source, the *XClumpy* model is consistent with most of the results of decoupled `MYTorus` and `borus02` models, except in Γ.

- **ESO138 G-001:** For this source, T22 used the observations of XMM-*Newton* and *NuSTAR* (ObsID: 60201040002). T22 find an LOS column density and photon index, at 90% confidence, of $N_{H,LOS} = (0.42 - 0.50) \times 10^{24}$ cm^{-2} and $\Gamma = 1.42 - 1.51$, respectively. The results are quite inconsistent with our results (see Table 18), especially when compared to the photon index from `borus02`, which is $\Gamma = 1.95 - 1.99$. Similarly, the computed equatorial (average) column density has a value within the range ($N_{H,eq} = (1.68 - 6.87) \times 10^{24}$ cm^{-2}) of our analysis. Their covering factor of $\theta_{Tor} = 10° - 13°$ lies far below the `borus02` estimates of $\theta_{Tor} = 34° - 47°$. For this source, the *XClumpy* model in T22 is inconsistent with the decoupled `MYTorus` and `borus02` results. We note that `borus02` results in a better fit (reduced χ^2 value ~ 1.32) compared to the fit found by T22 (reduced $\chi^2 = 1.39$).

In summary, from the above comparisons, we find *XClumpy* places stronger constraints on the different torus parameters with respect to `borus02` and `MYTorus` given the smaller associated uncertainties. The only exception is ESO138 G-001, which is best-fitted using `borus02` in our analysis, because T22 did not include the prominent emission lines that we mention in Table 5. We also notice that the `XCLUMPY` model shifts the best-fit value of photon index to harder values by $\sim 6\% - 22\%$ compared to `borus02` and by $\sim 0.6\% - 26\%$ compared to the best-fit model of decoupled `MYTorus` in our sample. In Table 6, we show the values of photon index and average torus column density computed using different torus models for each source. We note that T22 used only one *NuSTAR* observation for each source. In this work, we used all the available observations from *NuSTAR* for these heavily obscured sources in order to increase the photon statistic over 10keV and minimise the under- and overestimation of spectral parameters. Overall, for our sources, we do not find any significant discrepancies when using *XClumpy* in comparison with `borus02` and decoupled `MYTorus` models.

3.6 Conclusions and Summary

In this work, we studied and classified seven CT-AGN candidates from the 100 month *Swift-BAT* catalogue using archival *NuSTAR* observations. All sources have at least one *NuSTAR* observation covering the 3–50 keV energy range. In the 0.6–10 keV band, we used XMM-*Newton* data for three targets, *Chandra* data for two targets, and both XMM-*Newton* and *Chandra* for one target. NGC 2788A has only *Swift-XRT* data in the soft X-ray. We classified the sources on the basis of their best-fit value of LOS hydrogen column density; that is, if $N_{H,LOS} \geq 10^{24}$ cm^{-2} the candidates are marked as bona fide CT-AGN. Otherwise, they are identified as partially CT-AGN or Compton-thin AGN depending on their column density. The summary of our results and conclusions are as follows:

1. From the seven CT-AGN candidates, three are confirmed CT-AGN with moderate to high covering factors based on *NuSTAR* data above 10 keV. Three of them show a Compton-thin LOS column density, but a torus column density above the CT threshold. Only 2MASX J20145928+2523010 shows Compton-thin values in both the column densities. A summary of the results for all of these sources with the `borus02` model is displayed in Table 7.

2. This present work updates the total number of *NuSTAR*-confirmed CT-AGN to 35 for $z < 0.05$, which is $\sim 8\%$ of the total AGN population in the 100 month BAT catalogue. This value is still relatively far below the value predicted by the CXB population synthesis models ($\sim 20\% - 50\%$), which suggests that a significant fraction of heavily obscured AGN are missed even by a hard-X-ray telescope such as *Swift-BAT*.

3. Out of 55 CT-AGN candidates analysed by our Clemson-INAF research group, adding the results of this work brings the population of confirmed CT-AGN to 27 ($\sim 50\%$). Among these, only 14 ($\sim 25\%$) candidates show both $N_{H,LOS}$ and $N_{H,avr}$ above the CT threshold.

4. We find no correlation between these two column densities ($N_{H,LOS}$ and $N_{H,avr}$) from our sample. Our results state that identifying a bona fide CT-AGN, that is, an obscured AGN with $N_{H,LOS} > 10^{24}$ cm^{-2} , does not necessarily mean that the torus is also CT. Similarly, a Compton-thin $N_{H,LOS}$ does not necessarily signify that the torus is also Compton-thin.

5. Most of these obscured galaxies have a significantly clumpy or inhomogeneous distribution of clouds. Multi-epoch monitoring of these sources using telescopes such as XMM-*Newton*, *Chandra*, and *NuSTAR* will help us to study their intrinsic flux and LOS column density variability. This will lead to a better understanding of cloud movements in the obscuring medium and X-ray emission from the central engine.

6. `MYTorus` and `borus02` results are consistent with each other in estimating the column densities and other parameters of the sources. In most cases, `borus02` shows better fitting from a statistical point of view. It also estimates the torus opening angle and inclination angle of the obscured AGN, which are fixed parameters in `MYTorus`.

7. We find our results on the seven CT-AGN candidates using the uniform torus models to be compatible with the results of the non-uniform torus model `XCLUMPY` in Tanimoto et al., 2022. However, we also notice the trend that `XCLUMPY` shifts the photon index to harder values in comparison to the uniform torus models we use here. For reference, we display the Γ and torus column density values of T22 with respect to our results in Table 6.

In the next chapter, a joint analysis of the X-ray properties and the reprocessed emission at mid-IR is carried out in order to gain a better understanding of the torus structure and obscuration properties. There, I have also used multi-epoch observations to understand the dynamic nature of the obscuring medium.

4 Multi-Wavelength Overview of the AGN Torus: NGC 6300

In this chapter, I presented the analysis on torus and nuclear emissions of NGC 6300, using physically motivated X-ray torus models and optical-FIR SED fitting. It is extensively based on the results that will be showed in Sengupta et al. 2024 (in prep).

4.1 Introduction

According to the unification theory of active galactic nuclei (AGN, Urry and Padovani, 1995), the accreting supermassive black holes (SMBH) are surrounded by an obscuring medium of dust and gas, commonly referred as 'torus'. This torus is homogeneous and obscures the broad line region (BLR) from the line-of-sight (LOS) observation. The torus acts as an absorber of optical-ultraviolet (optical-UV) radiation from the accretion disk of SMBH, and re-emits at infrared (IR) wavelengths (Netzer, 2015; Ramos Almeida and Ricci, 2017). However, recent IR observations and analyses of spectral energy distributions (SED) suggest an alternative scenario where the torus exhibits a clumpy structure instead of being homogeneous (e.g., García-Burillo et al., 2021a; Nenkova et al., 2002; Ramos Almeida et al., 2014). The LOS obscuration of local AGN in the X-ray spectra supports the clumpy torus scenario (e.g., Risaliti et al., 2002). LOS X-ray Variability (of hydrogen column density- $N_{H,LOS}$) due to the obscuration has been identified across a broad spectrum from the timescales of approximately one day (e.g., Elvis et al., 2004; Risaliti and Elvis, 2004) to years (e.g., Markowitz et al., 2014). Also, there is a diverse range of observed density fluctuations in obscuration: from minor variations of $\Delta(N_{H,los}) \sim 10^{22}$ cm^{-2} e.g., Laha et al., 2020 to the intriguing cases of changing-look AGN which goes through the transitions between Compton-thin (10^{22} cm^{-2} ¡ $N_{H,LOS} < 10^{24}$ cm^{-2}) and Compton-thick ($N_{H,LOS} > 10^{24}$ cm^{-2}) states (e.g., Bianchi et al., 2009; Marchesi et al., 2022; Risaliti et al., 2005; Rivers et al., 2015 and more).

Studies with fairly large source samples and regular observations can provide valuable insights into the torus structure. The $\Delta(N_{H,los})$ method, applied between two observations separated by Δt, establishes upper limits to cloud sizes and distances to the SMBH (Marchesi et al., 2022; Pizzetti et al., 2022; Risaliti et al., 2002; Torres-Albà

et al., 2023c). Along with $\Delta(\mathrm{N_{H,los}})$, we can also study the fraction of flux variability (Δ(flux)) that is not linked with the column density changes, but with a variation in the intrinsic radiation coming from the central engine of the AGN.

This paper is focused on studying the local Seyfert 2 galaxy NGC 6300 ($z = 0.0037$; RA=$17°16'59.47''$, Dec=$−62°49'14.0''$). This source is selected from the Compton-Thin sample of Zhao et al., 2021, in continuation with the work by Torres-Albà et al., 2023c and Pizzetti et al. (submitted) to investigate the column density variability of Compton Thin AGN in the local Universe (z ¡ 0.1). NGC 6300 is classified as a barred spiral SBb-type galaxy. It has been observed by the Rossi X-ray Timing Explorer (*RXTE*) in 02/1997 (Leighly et al., 1999), *BeppoSAX* in 08/1999 (Guainazzi, 2002) and XMM-*Newton* in 03/2001 (Matsumoto et al., 2004). From these early studies, it was classified as a 'transient' or changing-look AGN candidate undergoing through a period of low activity. Later, in five epochs from 2007 to 2016, it was observed nine times using *Chandra X-ray Observatory* (*Chandra*), `Suzaku` and the *Nuclear Spectroscopic Telescope Array* mission (*NuSTAR*; Harrison et al., 2013). In Jana et al., 2020, all these observations were studied through time analysis and X-ray spectral analysis using phenomenological models like *powerlaw, compTT, pexrav* and one of the first physically motivated homogeneous torus models: `MYTorus` (Murphy and Yaqoob, 2009). They showed the presence of a clumpy torus using decoupled configuration (where direct powerlaw, reflected and line components are untied) of `MYTorus`, but did not find any significant flux or column density variability. They also showed the intrinsic luminosity of the source varies ($\Delta \mathrm{L_{int}} \sim 0.54 \times 10^{42}$ erg s^{-1}) from 2009 to 2016.

In this work, we have carried out a comprehensive and systematic X-ray spectroscopic analysis of NGC 6300, including a new *Chandra* observation taken in 2020. Along with that, for a better characterization of the obscuring torus, we also used optical-IR SED fitting. Firstly, we have conducted the X-ray spectral analysis combining sensitive E<10 keV observations by *Chandra* and `Suzaku`, with *NuSTAR* data at E>3 keV: these observations cover a time period from 2007 to 2020. We examined the torus properties, such as inclination angle, covering factor, column density from an X-ray point of view. This is being done by using the latest physical motivated X-ray torus models like `borus02` (Baloković et al., 2018), `UXCLUMPY` (Buchner et al., 2019) and `XCLUMPY` (Tanimoto et al., 2019b) which allow us for a proper geometrical characterization of the obscuring material in both smooth and clumpy configurations. Secondly, using aperture photometry, we extracted fluxes from the optical to far-infrared (FIR)

band. Using the fluxes and the output parameters of X-ray spectral fitting, we used the broad-band SED fitting tool `XCIGALE` (Yang et al., 2020) to infer the torus geometry with its host galaxy properties in the mid-IR and X-rays, taking into account all of the physical processes and components of AGN (Buchner et al., 2019; Esparza-Arredondo et al., 2021; Esparza-Arredondo et al., 2019). Thus, a joint analysis has been carried out by combining the mid-IR SED-derived view of the obscuring medium with that from X-rays. Along with these two approaches, we have also implemented the procedures of Marchesi et al., 2022; Torres-Albà et al., 2023c, using the multi-epoch X-ray monitoring to link flux and hydrogen column density variability in different epochs, revealing the dynamical properties of the obscuring medium.

The data reduction processes from X-ray observations and optical-FIR photometry selection procedures are discussed in Section 4.2. In Section 4.3, we give a brief description of the X-ray torus models and mid-IR models we have used. The results and analysis from the X-ray spectral fitting and `XCIGALE` SED fitting are presented in Section 4.4. Finally, in Section 4.5, we summarize our analysis and discuss the conclusions of this paper. All reported error ranges from X-ray spectral analysis are at the 90% confidence level unless stated otherwise. Through the rest of the work, we assume a flat ΛCDM cosmology with $H_0 = 69.6 \, \mathrm{km \, s^{-1} \, Mpc^{-1}}$, Ω_m=0.29, and Ω_Λ=0.71 (Bennett et al., 2014).

4.2 Multi-wavelength observations

NGC 6300 has been observed ten times from 2007 to 2020, using X-ray telescopes, as shown in Table 8. It has also been observed multiple times in the optical-FIR band. In this section, we discuss the data reduction and data processing techniques of the different X-ray telescopes whose archival data we are using in this work. Also, we discuss the photometry extraction procedure from optical-FIR images.

4.2.1 X-ray observations and data reductions

NuSTAR **data reduction**

The source has been observed by *NuSTAR* three times. The collected data have been processed using the *NuSTAR* Data Analysis Software (NUSTARDAS) version 2.1.2.

Table 8: X-ray observational log of NGC6300

Instrument	ObsID	Start Time (UTC)	Exposure time (ks)	Net spectral counts[a]
Suzaku	702049010	2007-10-17	82.6	21213
Chandra	10289	2009-06-03	10.2	2714
Chandra	10290	2009-06-07	9.8	3524
Chandra	10291	2009-06-09	10.2	2796
Chandra	10292	2009-06-10	10.2	3404
Chandra	10293	2009-06-14	10.2	3124
NuSTAR	60061277002	2013-02-25	17.7	6294,6457
NuSTAR	60261001002	2016-01-24	20.4	6405,6555
NuSTAR	60261001004	2016-08-24	23.5	8604,8296
Chandra	23223	2020-04-26	10.1	1011

[a]The reported net spectral counts are background-subtracted total source counts. For *NuSTAR* net counts are those of the FPMA and FPMB modules for a radius of 30" between 3 and 50 keV, respectively. The reported *Chandra* net counts are from the ACIS-S detector, except for ObsID 23223 it is ACIS-I, for a radius of 5" in the 0.8–7 keV energy range . The Suzaku net counts are from XIS-1 detector for a radius of 150" in the 0.8–8.0 keV energy range.

Calibration of the raw event files are performed using the *nupipeline* script and the response file from *NuSTAR* Calibration Database (CALDB) version 20211020. We utilized both focal plane modules (FPMA and FPMB) of the *NuSTAR*. The source and background spectra are extracted from $30''$ ($\approx 50\%$ of the encircled energy fraction–EEF at 10 keV) and $50''$ circular regions, respectively. The *nuproducts* scripts are used to generate the source and background spectra files, along with response matrix files (RMF) and ancillary response files (ARF). Finally, using *grppha*, the *NuSTAR* spectra are grouped with at least 20 counts per bin. We have used all the three available *NuSTAR* observational data taken from 2013 to 2016, in order to check variability and improve the statistics of the spectra between 3 and 50 keV.

Chandra data reduction

NGC 6300 has been observed by *Chandra* five times in 2009 and one time in 2020, using the Advanced CCD Imaging Spectrometer (ACIS). All the observations of 2009 were carried out in FAINT mode, while the 2020 observation was instead taken in VFAINT[17] mode. We processed and reduced the data with Chandra Interactive Analysis of Observations (CIAO) software version– 4.13 and *Chandra* CALDB version 4.9.5. We begin with processing the level-2 event files for each observation using the CIAO script *chandra_repro*. The source and background spectra are extracted from $5''$ (includes $> 99\%$ of EEF) and $15''$ circular regions, respectively, using the *dmextract* and *specextract* tools at 0.3-7.0 keV energy range.

Suzaku data reduction

For this work, we used a Suzaku observation taken on 2007-10-17. The data were extracted following the ABC guide[18] from HEASARC. Running the aepipeline, we extracted the spectra from both the frontside (XI0, XI3) and back-side (XI1) illuminated chips unit of the X-ray Imaging Spectrometers (XIS) on a source region of 150". The response, ancillary and background files were generated running the tasks xisrmfgen, xissimarfgen and xisnxbgen, respectively. We then grouped the data to a minimum of 50 counts per bin in order to use the χ^2 statistics.

---

[17]https://cxc.cfa.harvard.edu/ciao/why/aciscleanvf.html
[18]https://heasarc.gsfc.nasa.gov/docs/suzaku/analysis/abc/

4.2.2 Optical-FIR observations and photometry

In order to comprehensively assess the flux of NGC 6300 over a range of wavelengths, we conducted aperture photometry using a fixed circular aperture with a radius of 9". This choice was deliberate, as it ensured the inclusion of the Full Width at Half Maximum (FWHM) of the Point Spread Function (PSF) for each filter employed in our analysis.

For the optical bands (450W, 606W, and 814W), we leveraged the highest-quality images available from the Hubble Space Telescope (HST), sourced from the Mikulski Archive for Space Telescopes[19]. Expanding our measurements into the near-infrared (NIR) to far-infrared (FIR) bands, we incorporated data from the JHKs bands (Two Micron All Sky Survey - 2MASS), Spitzer IRAC and WISE, Spitzer MIPS 24 and 70 microns, Herschel PACS at 70 and 160 microns, and Herschel SPIRE at 250 microns. All data from these bands were obtained from calibrated images available in the Dustpedia database[20].

For the background subtraction, we implemented a two-dimensional modeling approach for background calculation using Photutils library version 1.9[21]. This method involved sigma clipping, a statistical technique that identifies and eliminates outliers from the dataset, while also applying a mask derived from the larger isophote provided by the Dustpedia database to exclude the galaxy as much as possible. In addition to these general background subtraction techniques, we used the star subtraction algorithm from Clark et al., 2018 to eliminate the influence of two stars (2MASS J17170066-6249261 and 2MASS J17165801-6249120) aligned with the extended part of the galaxy along the line of sight in the optical bands. Furthermore, we conducted aperture corrections and factored in the impact of Milky Way extinction on the observed brightness of NGC 6300. These procedures improve the quality of our data, and also remove any significant contamination from any other sources.

---

[19]https://mast.stsci.edu/
[20]http://dustpedia.astro.noa.gr/Data
[21]https://photutils.readthedocs.io/

4.3 Spectral modeling

For the X-ray spectral fitting of NGC 6300, we have used `XSPEC` Arnaud, 1996 version 12.13.0 within the HEASOFT software (version 6.31). The metallicity is fixed at solar values from Anders and Grevesse, 1989, and the photoelectric cross sections for all absorption components are determined using the method described in Verner et al., 1996. The Galactic absorption column density is fixed at 8.01×10^{20} cm^{-2}, following Kalberla et al., 2005.

4.3.1 Soft X-ray Model

Due to the large extraction region of `Suzaku`, we needed to handle the influence of a complex multiphase medium below 2 keV. To tackle this issue, we introduced a simple soft excess model, following Torres-Albà et al., 2023c, in an attempt to produce a good fit in the soft X-ray part of the X-ray spectra from `Suzaku`:

$$\text{Soft Model} = vapec_1 + zphabs * vapec_2 \tag{26}$$

For NGC 6300, we used the variant$-apec$ or $vapec$ parameter to adjust the metal abundance pattern of the host galaxy. The first component is a standard thermal emission component and the second component is multiplied with a photoelectric absorption component $zphabs$ to represent a medium closer to the nucleus. We find the metallicity abundance ratios of a typical type II supernova explosion (SNe) properly reproduce a good fit in the soft X-ray emission part. The ratios we used: (Mg, Si)/O = 1, (Ne, S)/O = 0.67, (Ar, Ca, Ni)/O = 0.46 and Fe/O = 0.27 (Dupke and Arnaud, 2001; Iwasawa et al., 2011). We also find from Table 9, the temperature of the medium closer to the center is cooler than the outer region ($T_1 > T_2$), which is observed within a minor population of Torres-Albà et al., 2018. This first approximation model is not sufficient enough to understand all the complexities within the multiphase media of the host galaxy. As this model produces a better fit and our work is focused on characterizing the torus model, which comes from the reflection and line component (> 2 keV), we keep this model to fit the soft part of the spectra.

4.3.2 X-ray torus models

We have adopted a standard approach for analyzing the X-ray spectra of a heavily obscured AGN. This approach employs self-consistent and physically motivated smooth (uniform distribution of gas) and clumpy X-ray torus models, utilizing Monte Carlo simulations. For smooth geometry we used `borus02` (Baloković et al., 2018) and for clumpy geometry we used `UXCLUMPY` (Buchner et al., 2019) and `XCLUMPY` (Tanimoto et al., 2019b). In the following sections, we provide an overview of how these models were applied in our analysis.

`borus02`

The obscuring medium in `borus02` consists of a spherical geometry with biconical (polar) cut-out regions. This model is composed of three components: (a) `borus02` itself, which is a reprocessed component (including Compton-scattered + fluorescent lines component), (b) $zphabs*cabs$ to include line-of-sight (LOS) photoabsorption with Compton scattering through the obscuring clouds; with this component, we multiply a $cutoffpl_1$ to account for the primary power-law continuum, and (c) finally, another $cutoffpl_2$ component is included separately, multiplied by a scaling factor $f_s < 1$, to incorporate a scattered unabsorbed continuum. The torus covering factor (C_{Tor}) in `borus02` vary within the range of $0.1 - 1$ (i.e., the torus opening angle falls within the range of $\theta_{Tor} = 0° - 84°$). The inclination angle θ_{Inc} is kept free, ranging from $18°$ to $87°$. We used the following model configuration in `XSPEC`:

$$\text{Model } \texttt{borus02} = C_{flux} * phabs * (borus02 + zphabs$$
$$* cabs * cutoffpl_1 + f_s * cutoffpl_2 \tag{27}$$
$$+ \text{Soft Model}),$$

The C_{flux} component is a cross calibration constant which takes into account the total flux change of different observations. We included in all the models this flux-related parameter to study any flux variability that is not related with $N_{H,LOS}$. We linked all the `borus02` parameters like covering factor, inclination angle, $N_{H,av}$ and others with

each epoch, varying only $N_{H,LOS}$ (from $zphabs * cabs * cutoffpl_1$) and C_{flux} to study the LOS column density and flux variability, respectively.

UXCLUMPY

The obscurer in the Unified X-ray CLUMPY (UXCLUMPY) model has several torus geometries of interests, produced by Monte Carlo codes. This model is made up of two components: (a) *uxclumpy* itself, which is composed of the transmitted and cold reflected component with fluorescent lines and (b) *uxclumpy_scattered* which takes into account the warm reflected component responsible for the scattering of the power-law from coronal emission. This model includes clumpiness and dispersion of the obscuring medium, along with an inner Compton-Thick ring of clouds modelled by *CTKcover* ranging from 0 to 0.6. The cloud dispersion is modelled using the parameter *TORsigma* from 6° to 90°. The following model configuration is used in XSPEC.

$$\text{Model UXCLUMPY} = C_{flux} * phabs * (uxclumpy+ \\ f_s * uxclumpy\_scattered + \text{Soft Model}), \tag{28}$$

Following the same approach we used with the borus02 model, we linked all the UXCLUMPY parameters in each epoch except the LOS column density (from *uxclumpy*) and C_{flux} for the variability studies.

XCLUMPY

The obscuring torus in XCLUMPY model adopted the IR CLUMPY model from Nenkova, Sirocky, Ivezić, and Elitzur, 2008; Nenkova, Sirocky, Nikutta, et al., 2008. Each clump is assumed to be spherical with uniform gas density and radius. The clumpy distribution follows a power-law along the radial direction from inner edge to the outer edge of the torus and a Gaussian-normal distribution along the vertical axis of torus. The model consists of four components: (a) $cabs * zphabs * zcutoffpl$ is used to compute the primary power-law emission along the LOS; (b) $f_s * zcutoffpl$ is included to for the scattered unabsorbed emission; (c) *xclumpy_reflection* takes into account the reflected component of the torus and (d) *xclumpy_line* computes the fluorescence line

component. All the parameters of (c) and (d) are tied with each other. In `XSPEC` the following model configuration is used:

$$
\begin{aligned}
\text{Model } \texttt{XCLUMPY} = C_{flux} * phabs * (cabs * zphabs* \\
zcutoffpl + f_s * zcutoffpl + xclumpy\_reflection \\
+xclumpy\_line + \text{Soft Model}),
\end{aligned}
\tag{29}
$$

We derive from the X-ray spectral fitting the hydrogen column density along the equatorial plane ($N_{H,eq}$), the torus angular width (σ) within $10° - 90°$ and the inclination angle (θ_i) within $20° - 87°$. We calculate the LOS column density ($N_{H,LOS}$) using these parameters in the following equation:

$$
N_{H,LOS} = N_{H,eq} \left[\exp\left\{ \frac{(\theta_i - 90°)^2}{\sigma^2} \right\} \right]
\tag{30}
$$

We calculated the 90% confidence error range of $N_{H,LOS}$ using the standard error propagation method over the parameters $N_{H,eq}$, σ and θ_i. We kept $N_{H,eq}$ and C_{flux} free to vary in each epoch for the variability studies, linking the rest of the parameters.

4.3.3 Dust and mid-IR torus models

Galaxies are formed of multiple components (e.g., gas, dust, stars, AGN) which emit radiation across all wavelength. We used the `CIGALE` (Boquien et al., 2019) included with the X-ray module of Yang et al., 2020, called 'XCIGALE'. It is a SED fitting code that is used to decouple the different galaxy components and study their physical properties. For NGC 6300, we have collected photometric data from the optical to FIR band at 9″ around the center of the galaxy. The X-ray fluxes are added from the X-ray spectral fits of `borus02` (all the models show consistent results, so we decided to use one of them) as mentioned in Section 4.3.2. In this paper, we will briefly discuss on the host galaxy obscuration from stellar and dust components, but mainly focus on the torus physical properties.

The module we used to study the star formation history (SFH) is `sfhdelayed`, which is a popular model that assumes a continuous star forming rate (SFR) in the galaxy. We used the stellar population library `bc03` from Bruzual and Charlot, 2003 to compute the intrinsic stellar spectrum. The dust attenuation from UV to the NIR is computed by the `dustatt_modified_starburst` module based on Calzetti et al., 2000 and Leitherer et al., 2002. Dust absorbs the optical-UV photons and re-emits at mid-IR to FIR domains covering polycyclic aromatic hydrocarbon (PAH) bands ($\sim 8\mu$m), and also emission from small warm grains ($< 100\mu$m) and big cold grains ($\sim 100\mu$m). We modeled these dust emission processes using the `dl2014` module from Draine et al., 2014.

To model the AGN emission, we used the `skirtor2016` torus model and X-ray model from Yang et al., 2020. The input physical parameters, specifically the opening angle ($40°$), inclination angle ($50°, 60°$) and photon-index ($\Gamma = 1.8$) were selected following the best-fit values of X-ray spectral fits. The accretion disk spectrum is set from the AGN emission module of Schartmann et al., 2005. For the rest of the parameters, such as α_{ox}, AGN fraction, optical depth at 9.7 μm and others, we applied a wide range of input parameters to improve the SED fitting. The X-ray fluxes are derived from the X-ray spectral fits within the range of 2-10 keV and 10-40 keV.

4.4 Results and discussions

4.4.1 Results from X-ray spectral fitting

In this section, we present the results of the X-ray fitting, as well as of the statistical analysis that we conducted to determine if NGC 6300 is variable, either in luminosity or in column density.

Variability Evaluation

One of the objectives of this work is to measure the variability in the obscuring medium ($N_{\mathrm{H,los}}$) and the variability of the intrinsic radiation coming from the central engine of NGC 6300. We used two statistical techniques to test these variabilities: Tension Statistics and Null Hypothesis. The reduced χ^2 (χ^2_{Red}) and statistical comparisons

Table 9: X-ray fitting results for NGC 6300

| Parameter		borus02	UXCLUMPY	XCLUMPY
χ^2/d.o.f		2470/2571	2470/2571	2475/2572
χ^2_ν		0.96	0.96	0.96
Tσ		2.9σ	2.9σ	2.9σ
kT_1		$0.78^{+0.08}_{-0.08}$	$0.78^{+0.08}_{-0.08}$	$0.78^{+0.08}_{-0.08}$
kT_2		$0.11^{+0.00}_{-0.00}$	$0.12^{+0.00}_{-0.00}$	$0.10^{+0.00}_{-0.00}$
apec norm ($\times 10^{-4}$)		$6.97^{+1.33}_{-1.13}$	$6.15^{+1.89}_{-1.28}$	$6.69^{+1.34}_{-1.07}$
Γ		$1.76^{+0.05}_{-0.05}$	$1.82^{+0.03}_{-0.06}$	$1.71^{+0.03}_{-0.04}$
$N_{H,av} \times 10^{24}\,cm^{-2}$		$2.64^{+1.09}_{-0.62}$	$\cdots$	$\cdots$
$f_s \times 10^{-2}$		$0.11^{+0.02}_{-0.02}$	$0.44^{+0.48}_{-0.14}$	$0.07^{+0.02}_{-0.02}$
C_F		$0.59^{+0.12}_{-0.10}$	$\cdots$	$\cdots$
$\cos(\theta_i)$		$0.50^{+0.10}_{-0.07}$	$\cdots$	$\cdots$
θ_i		$\cdots$	0^{+*}_{-*}	$53.26^{+3.35}_{-1.89}$
CTKcover		$\cdots$	$0.60^{+*}_{-0.21}$	$\cdots$
TORσ		$\cdots$	$24.14^{+37.33}_{-4.96}$	$\cdots$
σ		$\cdots$	$\cdots$	$18.64^{+0.96}_{-1.69}$
C_{flux}	Suzaku— 17/10/2007	$1.09^{+0.05}_{-0.04}$	$1.24^{+0.21}_{-0.18}$	$1.13^{+0.03}_{-0.03}$
	Chandra— 03/06/2009	$0.91^{+0.07}_{-0.06}$	$1.03^{+0.19}_{-0.16}$	$0.95^{+0.07}_{-0.06}$
	Chandra— 07/06/2009	$1.14^{+0.08}_{-0.07}$	$1.29^{+0.22}_{-0.18}$	$1.19^{+0.07}_{-0.06}$
	Chandra— 09/06/2009	$0.96^{+0.07}_{-0.07}$	$1.11^{+0.22}_{-0.18}$	$1.01^{+0.06}_{-0.06}$
	Chandra— 10/06/2009	$1.09^{+0.08}_{-0.07}$	$1.23^{+0.21}_{-0.17}$	$1.14^{+0.07}_{-0.07}$
	Chandra— 14/06/2009	$1.09^{+0.08}_{-0.07}$	$1.27^{+0.25}_{-0.21}$	$1.15^{+0.05}_{-0.07}$
	NuSTAR— 25/02/2013	1	1	1
	NuSTAR— 24/01/2016	$0.85^{+0.03}_{-0.03}$	$0.88^{+0.08}_{-0.06}$	$0.85^{+0.02}_{-0.02}$
	NuSTAR— 24/08/2016	$0.96^{+0.03}_{-0.03}$	$1.00^{+0.08}_{-0.07}$	$0.95^{+0.02}_{-0.02}$
	Chandra— 26/04/2020	$0.41^{+0.05}_{-0.05}$	$0.49^{+0.10}_{-0.11}$	$0.40^{+0.03}_{-0.03}$
$N_{H,l.o.s.}$	Suzaku— 17/10/2007	$20.57^{+0.54}_{-0.52}$	$19.30^{+0.34}_{-0.57}$	$20.30^{+16.54}_{-16.69}$
	Chandra— 03/06/2009	$19.60^{+1.03}_{-0.97}$	$18.63^{+0.71}_{-1.04}$	$19.46^{+15.85}_{-16.00}$
	Chandra— 07/06/2009	$18.43^{+0.81}_{-0.76}$	$17.84^{+0.74}_{-1.15}$	$18.31^{+14.95}_{-15.05}$
	Chandra— 09/06/2009	$20.17^{+1.00}_{-0.94}$	$19.21^{+0.62}_{-0.94}$	$20.10^{+16.38}_{-16.54}$
	Chandra— 10/06/2009	$18.84^{+0.90}_{-0.85}$	$18.04^{+0.71}_{-1.04}$	$18.67^{+15.25}_{-15.36}$
	Chandra— 14/06/2009	$20.54^{+0.96}_{-0.91}$	$19.44^{+0.56}_{-0.83}$	$20.52^{+16.72}_{-16.88}$
	NuSTAR— 25/02/2013	$15.50^{+1.05}_{-1.08}$	$14.33^{+1.21}_{-1.03}$	$14.65^{+11.97}_{-12.08}$
	NuSTAR— 24/01/2016	$16.22^{+1.09}_{-1.09}$	$15.26^{+1.17}_{-1.49}$	$15.32^{+12.51}_{-12.62}$
	NuSTAR— 24/08/2016	$13.80^{+0.93}_{-0.99}$	$12.57^{+0.75}_{-0.82}$	$12.87^{+10.52}_{-10.61}$
	Chandra— 26/04/2020	$21.75^{+2.06}_{-1.87}$	$20.79^{+2.43}_{-2.08}$	$20.52^{+16.72}_{-16.78}$
$\log(flux_{2-10keV})$		$-10.38^{+0.06}_{-0.06}$	$-10.34^{+0.07}_{-0.07}$	$-10.41^{+0.05}_{-0.04}$
$\log(flux_{10-40keV})$		$-10.29^{+0.06}_{-0.06}$	$-10.29^{+0.07}_{-0.08}$	$-10.29^{+0.04}_{-0.04}$
$\log(lum_{2-10keV})$		$42.10^{+0.06}_{-0.06}$	$42.14^{+0.07}_{-0.07}$	$42.07^{+0.03}_{-0.05}$
$\log(lum_{10-40keV})$		$42.19^{+0.06}_{-0.06}$	$42.19^{+0.07}_{-0.07}$	$42.19^{+0.03}_{-0.05}$
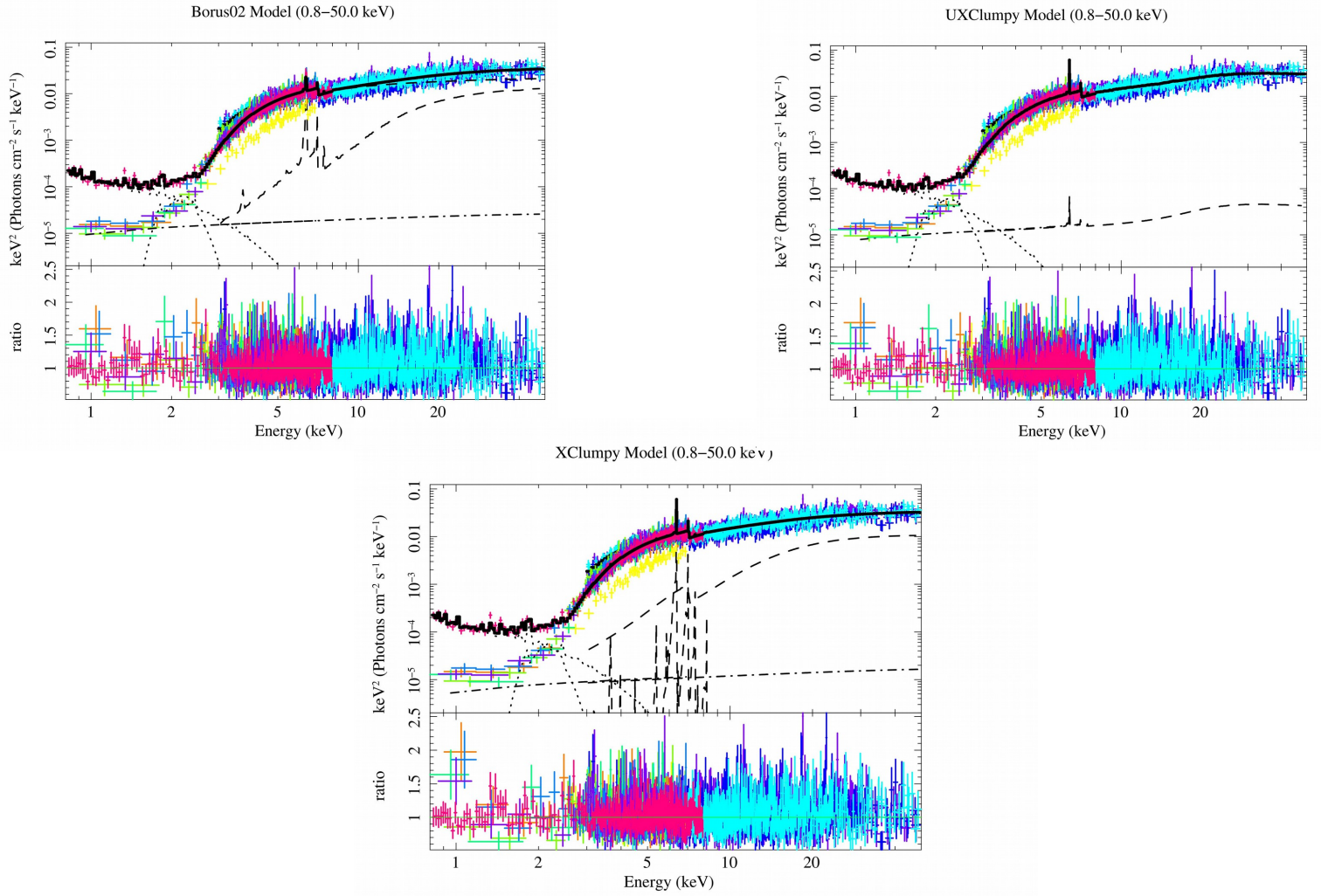
Figure 17: X-ray spectral fitting of `borus02`, `UXCLUMPY` and `XCLUMPY` models over unfolded spectrum of NGC 6300. The *Chandra* data are plotted in royal blue, orange, violet, lime, spring green and yellow. The *NuSTAR* data are plotted in magenta, blue, cyan. The `Suzaku` data are plotted in crimson. The best-fit model prediction is plotted as a black solid line. The single components of the model are plotted in black with different line styles. For `borus02`, the absorbed intrinsic power-law and Compton reflection + line component is plotted with dashed line. The scattered component is marked as dot-dash line and the thermal emission from the multi-phase medium as dotted line. In `UXCLUMPY`, the Compton reflection + line component is marked as dash line and scattered continuum as dot-dash line. In `XCLUMPY`, the Compton reflection and fluorescent line component is plotted as dash lines. The scattered continuum is plotted as dot-dash line. The thermal emission from the multi-phase medium is marked as dotted line for all the three models.

Table 10: Variability analysis of NGC 6300

Parameter	borus02	UXCLUMPY	XCLUMPY
χ^2/d.o.f	2470/2571	2470/2571	2475/2572
Tσ	2.9σ	2.9σ	2.9σ
χ^2/d.o.f (No Var)	6132/2589	6116/2589	6001/2590
$T_{\mathrm{No\,Var}}\ \sigma$	98.5σ	98.0σ	94.8σ
χ^2/d.o.f (N_H Var)	2738/2580	2752/2580	2784/2581
$T_{\mathrm{N_H\,Var}}\ \sigma$	4.4σ	4.8σ	5.6σ
χ^2/d.o.f (C_{AGN} Var)	2631/2580	2670/2580	2657/2581
$T_{\mathrm{C_{flux}\,Var}}\ \sigma$	1.4σ	2.5σ	2.1σ
p-value N_H	0.60	0.48	1.00
p-value C_{AGN}	0.01	0.72	1.52E-9

are reported for all three models in Table 10. A χ^2 distribution is approximated as a Gaussian distribution with large degrees of freedom (N).

For a 'true' model with perfect fit, the reduced χ^2 follows a Gaussian distribution centered around the mean value of 1 and standard deviation σ Andrae et al., 2010. Following the approach outlined in Torres-Albà et al., 2023c, we used 'Tension' or T to define how far or close the applied model is in comparison with a 'true' model fit.

$$T = \frac{|1 - \chi^2_{\mathrm{Red}}|}{\sigma} \tag{31}$$

Here, the standard deviation is $\sigma = \sqrt{\frac{2}{N}}$. In the first two rows of Table 10, we calculated the $T\sigma$ values for the best fit of each model. In the next rows, we displayed three cases: (1) no intrinsic flux or $N_{H,los}$ variability, that is, fixing all the parameters to one value; (2) allowing only $N_{H,los}$ variability, that is, varying the LOS column densities for each epoch but fixing the fluxes to one value; (3) allowing only flux variability, that is, varying the fluxes for each epoch but fixing the $N_{H,los}$ to a single value. We find that for all the models, the $T_{\mathrm{No\,Var}}\ \sigma$ is close to 100σ which is extremely higher than the best fit, showing that the AGN is definitely variable. On the other hand, for the case (3) the fit gets better than the best fit ($T_{\mathrm{C_{flux}\,Var}}\ \sigma = 1.4 - 2.1\sigma$) when we vary the flux and keep $N_{H,los}$ fixed. This shows that the source is not purely $N_{H,los}$-variable. However, for case (2), we find $T_{\mathrm{N_H\,Var}}\ \sigma = 4.4 - 5.6\sigma$, showing the fit slightly worsens
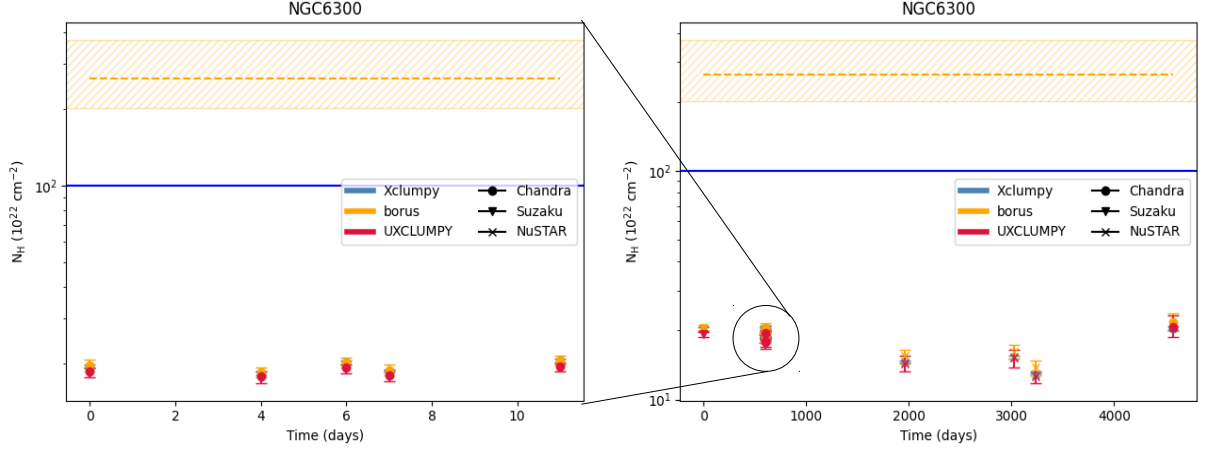
Figure 18: $N_{H,LOS}$ variability in all the six epochs from 2007 to 2020, using all the X-ray torus models. The blue horizontal line indicates the Compton-Thick column density threshold. *Left:* All the observations from *Chandra* from 2009 are shown. *Right:* All the observations, including the *Chandra* ones, are shown.

when we fix the flux. In conclusion, it shows that the source is definitely variable, but not purely $N_{H,los}$ variable.

The other approach we used is by calculating the χ^2 of column density and flux from different epochs, then calculate the p-value. We calculated the p-value by declaring the statement of null hypothesis for obscuring column density as $H_0 : N_H$ non-variable and for intrinsic flux as $H_0 :$ flux non-variable.

$$\chi^2_{N_H} = \sum_i \frac{(N_{H,LOS,i} - \langle N_{H,LOS} \rangle)^2}{\delta(N_{H,LOS,i})^2} \tag{32}$$

$$\chi^2_{flux} = \sum_i \frac{(flux_i - \langle flux \rangle)^2}{\delta(flux_i)^2} \tag{33}$$

We used the best-fit values of $N_{H,los}$ and flux for each epoch of each model. Following the approach outlined in Barlow, 2002 and Torres-Albà et al., 2023c for the asymmetric errors (δ), we used the δ^+ or δ^- depending on which of them deviates from the best-fit values more. From the obtained χ^2, we calculate the probability of the null hypothesis (p-value). We reject the null hypothesis if p-value < 1% for all the models, i.e., the

source is variable. If it shows p-value $> 1\%$ for all the models, then we accept the null hypothesis and declare the source as non-variable. Otherwise, we conclude that it is undetermined whether the statistical parameter is variable or not. For our source, we can conclude that it is not significantly N_H variable as all the models show p-value $> 1\%$. On the other hand, we find evidence of flux variability, as `borus02` shows the p-value $= 0.01$ and `XCLUMPY` shows p-value $\ll 0.01$.

Torus properties

Most of the torus properties are well constrained in all the three X-ray torus models, and are consistent with each other (see Table 9 and Figure 17). The `borus02` estimates the torus column density $N_{H,avr} \sim 2 \times 10^{24}$ cm^{-2} is around one order larger than the LOS column density in each epoch, which is $N_{H,LOS} \sim 2 \times 10^{23}$ cm^{-2} (see Figure 18). Thus, it shows that the reflected region has significantly higher column density, compared to the LOS region. Figure 18 also displays that the LOS column density also remains constant (almost) in all the epochs from 2007 to 2020, below the Compton-Thick blue line. It also portrays the existence of a clumpy torus as $\frac{N_{H,avr}}{N_{H,LOS}} \neq 1$ Sengupta et al., 2023; Torres-Albà et al., 2021. On the other hand, the `UXCLUMPY` model predicts the presence of an inner ring of clouds, having a high covering factor ranging from $0.39 - 0.60$. The torus have moderate to high vertical dispersion ($\mathrm{TOR}\sigma$) of the clouds. The presence of large Compton-Thick clumps of gas along the horizontal region, suggests a thick clumpy reflecting medium which is also predicted by `borus02`, as parameterized by the large $N_{H,avr}$ value. Similar to our source, the thick inner ring component was also required to model the spectra of NGC 7479 (Pizzetti et al., 2022) and IC 4518 A (Torres-Albà et al., 2023c). From the best-fit values of CTKcover and $\mathrm{TOR}\sigma$, we calculated the equatorial column density to be $N_{H,eq} = 4.37 \times 10^{25}$ cm^{-2}, by interpolating the $N_{H,eq}$ grid within `UXCLUMPY` (Pizzetti et al. prep). In comparison, the `XCLUMPY` model, which is constructed in absence of any inner thick clouds also estimates the Compton-Thick equatorial column density $\sim 10^{25}$ cm^{-2}. The inclination angle of the torus is a free parameter in `borus02` and `XCLUMPY`, and we measure it to be $\theta_i \sim 51° - 64°$ within the 90% confidence error, which is also in agreement with the results of García-Burillo et al., 2021a ($\sim 57°$) from ALMA observations. However, the error range of $N_{H,LOS}$ in `XCLUMPY` is one order of magnitude larger than in the other two models, even though the best-fit values are compatible with each other. We note that this over-estimation of the errors does not significantly affect the variability study. Altogether, the physically

motivated models are consistent with each other in portraying the torus properties.

To ensure the comprehensiveness of our investigation, we show that a substantial portion of the torus has been explored through the multi-epoch observations of the time scale of 13 years. Assuming simple Keplerian velocity for the individual clouds with independent circular orbits, the torus would have rotated an angle of:

$$\Delta\theta = \sqrt{\frac{GM}{r^3}} \times \Delta t \qquad (34)$$

For NGC6300, the previous papers like Khorunzhev et al., 2012 (from the mass-buldge luminosity correlation equation) and Gaspar et al., 2019 (from molecular gas radial velocity) estimated the SMBH mass $\sim 10^7$ $M_\odot$. Assuming the outer edge of this torus is somewhere between 1-30 pc (from García-Bernete et al., 2022; García-Burillo et al., 2021a; Gaspar et al., 2019), we calculate the torus have rotated between $0.00097° - 0.16°$. This distance, corresponds to a physical size of $\sim 5 \times 10^{-4} - 3 \times 10^{-3}$ pc. This region may not consist of a single cloud, but a group of clouds with slightly different densities, as observed at both shorter and longer time scales. Overall, the result of no significant N_H-variability shows a more homogeneous obscuring medium along the LOS in a rotating torus scenario.

However, considering clumps of single cloud obscuration from two consecutive epochs, we can obtain an estimate on the distance between the clouds and the SMBH (Marchesi et al., 2022; Risaliti et al., 2002). Using the equation:

$$d_{BH} \sim 600 \, t_{100}^2 \, \rho^2 \, N_{H,LOS}^{-2} \, Rs \qquad (35)$$

where t_{100} is the variability time in 100 ks units, ρ is the cloud density in 10^{10} cm^{-3} units and $N_{H,LOS}$ is the column density in 10^{24} cm^{-2} units. Putting the Khorunzhev et al., 2012 results on the estimated SMBH mass $M_{BH} = 3.89 \times 10^7 M_\odot$, we calculate the Schwarzschild radius $R_S = 1.15 \times 10^{13}$ cm $= 3.73 \times 10^{-6}$ pc. Using the lower ($3R_S$) and upper limit ($15R_S$) of X-ray corona size (Marchesi et al., 2022), we calculate the cloud density for $\rho_{3R_S} = \frac{\Delta(N_{H,LOS})}{3R_S}$ and $\rho_{15R_S} = \frac{\Delta(N_{H,LOS})}{15R_S}$, respectively. From the best-fit value of `borus02`, we calculated the $\Delta(N_{H,LOS})$. Our result in Table 11 suggests that the obscuring clouds are located from a distance of 100Rs to ~ 2.5 kpc scale (depending on the corona size), explaining the clumpy distribution of gas clouds. The

large timescales show $\sim 5 - 7$ times the difference of column density, suggesting that clouds are extended with the density profile increasing towards the centers. These values should be considered as an upper limit, as the observations are taken years apart. This means that the cloud might be at a much closer distance, but we cannot put any stronger constraints. Unlike from the sample of 12 variable AGN in Torres-Albà et al., 2023c, NGC 6300 shows even smaller variability ($\Delta(N_{H,LOS}) < 10 \times 10^{22}$ cm^{-2}) at large time scales greater than 100 days ($t_{100} > 86$). Considering the smallest and largest epoch of observations for $3R_s$ to $15R_s$ corona, we estimate the cloud size is within the range $\sim 5 \times 10^{-7} - 2 \times 10^{-4}$ pc, using equation 34.

4.4.2 Results from optical-FIR SED fitting

The SED-fitting result for the best model in `XCIGALE` is shown in Figure 19. The best-fit parameters of both the AGN (disk + torus) and the stellar components are reported in Table 12. Below we discuss the AGN and dust properties that are responsible for the obscuration.

AGN properties

The `XCIGALE` SED-fitting provides us with the observed AGN disk luminosity $L_{disk,i} = (4.39 \pm 3.43) \times 10^{40}$ erg s^{-1}. It comes out to be 100 times weaker than the intrinsic disk luminosity averaged over all directions, due to absorption along the LOS media of torus. The optical depth of the average edge-on torus at 9.7 μm is also around half of the estimated value from the SED fits on BCS sample of García-Bernete et al., 2022. The fit shows optical to X-ray spectral index $\alpha_{ox} = -1.25 \pm 0.04$, which is slightly lower than the mean value (~ -1.5; Lusso et al., 2010; Silverman et al., 2005) observed from the deep field surveys. The ratio of the AGN luminosity with respect to the total IR luminosity, i.e., AGN fraction, is found to be around 25%. The AGN luminosity averaged over all the directions from the SED fitting is $\sim 4.5 \times 10^{42}$ erg s^{-1}, from the SED fitting. The observed AGN dust i.e., the dust in the torus and polar dust region, re-emits with the luminosity $L_{dust,i} \sim 10^{42}$ erg s^{-1}. Using the luminosity at B-band (440 nm) from the SED fitting ($\sim 1.42 \times 10^{42}$ erg s^{-1}) and the optical bolometric correction factor $\kappa_{O,bol} \sim 5.13$ (Duras et al., 2020), we derive the bolometric luminosity $L_{bol} = \kappa_{bol} L_{B-band} = (7.27 \pm 0.14) \times 10^{42}$ erg s^{-1}. In comparison,

Table 11: Distance between obscuring cloud and SMBH

t_{100} [a]	$\Delta(N_{H,LOS})$ [b]	$d_{BH,3R_S}$	$d_{BH,15R_S}$
(100 ks)	(10^{22} cm^{-2})	(pc)	(pc)
513.87	0.97	472.47	18.90
3.37	1.17	2.03×10^{-2}	0.08×10^{-2}
1.59	1.74	0.45×10^{-2}	0.02×10^{-2}
1.61	1.33	0.46×10^{-2}	0.02×10^{-2}
2.98	1.70	1.59×10^{-2}	0.06×10^{-2}
1168.61	5.04	2443.46	97.74
917.69	0.72	1506.81	60.27
184.30	2.42	60.77	2.43
1159.00	7.95	2403.44	96.14

[a] The observational time differences are calculated following the sequence of observation from Table 8.
[b] Since all the three models are consistent with each other, we showed only the results of $\Delta(N_{H,LOS})$ from borus02.

100

the bolometric luminosity calculated from the X-ray spectral fitting (see Table 9) and using the X-ray bolometric correction factor $\kappa_{X,bol} \sim 15.45$ (Duras et al., 2020) is $L_{bol} = \kappa_{X,bol} L_{2-10keV} = (1.94 \pm 0.06) \times 10^{43}$ erg s^{-1}, which is ~ 2.7 times the one derived from the optical analysis. We adopted the mean of these two derived bolometric luminosities (i.e., $L_{AGN,bol} \sim 1.33 \times 10^{43}$ erg s^{-1}), to proceed with further calculations. From the estimated SMBH mass $\sim 3.89 \times 10^7$ M$_\odot$ (Khorunzhev et al., 2012) for NGC 6300, we calculate the $L_{Edd} = 4.90 \times 10^{45}$ erg s^{-1}[22]. Thus, the Eddington ratio[23] comes out to be $\lambda_{Edd} \sim 2 \times 10^{-3}$, which is almost one order lower than the one observed in Koss et al., 2017 and BAT Complete Seyfert (BCS) sample of García-Bernete et al., 2016.

We calculate the BH accretion rate from the relation $\dot{M} = \frac{L_{AGN,bol}}{\eta c^2}$ by adopting a canonical value of $\eta = 0.1$ (Soltan, 1982), and found to be $\dot{M} \sim 2.3 \times 10^{-3}$ M$_\odot$/yr $<< \dot{M}_{Edd} \sim 1.2$ M$_\odot$/yr. It is also possible that we are not observing a classical 10% efficiency (i.e., the value of η) from the accretion disk. AGN with such low accretion rate are often assumed to posses advection dominated accretion flow (ADAF; Esin et al., 1997; Narayan and Yi, 1994; Yuan and Narayan, 2014) around the inner regions of the accretion disk. For ADAF cases, the gas density within the accretion disk is assumed to be lower than the standard geometrically thin accretion disk (Shakura and Sunyaev, 1973), for which the radiation generated within the disk gets advected inward instead of escaping the disk, forming a geometrically thick accretion disk. NGC 6300 is an obscured AGN having intrinsic luminosity $\sim 10^{42}$ erg s^{-1}, which falls within the range of radiatively inefficient ADAF solutions.

From the best-fit model, we can also obtain the mid-IR luminosity at 12.3 nm, which is $\lambda L_\lambda = 2.9 \times 10^{42}$ erg s^{-1}. Using the mid-IR vs X-ray luminosity correlation equation from equation (2) of Gandhi et al., 2009, we derive the predicted $L_{2-10keV} \sim 2 \times 10^{42}$ erg s^{-1}. This value is very close to the value obtained from the X-ray spectral fit, where the displaying the intrinsic X-ray luminosity varies within the range $L_{2-10keV} \sim 1.2 - 1.4 \times 10^{42}$ erg s^{-1}. This agreement validates the fact that high resolution mid-infrared photometry can accurately proxy the intrinsic X-ray luminosity of local Seyfert galaxies like NGC 6300.

---

[22]Using the formula $L_{Edd} = 1.26 \times 10^{38} \frac{M}{M_\odot}$ erg s^{-1}.

[23]$\lambda_{Edd} = \frac{L_{AGN,bol}}{L_{Edd}}$.

Dust and stellar properties

From Table 12, we obtain the combined luminosity from stellar and dust component i.e. host galaxy luminosity as $L_{host} = (3.54 \pm 0.14) \times 10^{43}$ erg s^{-1}. It shows that the stellar dusts along the LOS is almost one order more luminous ($\frac{L_{host}}{L_{AGN}} \sim 8.8$) than the AGN (torus + polar dust), in the IR band. The SFR of NGC 6300 is found to be very low ~ 0.19 M$_\odot$yr^{-1} from the sfhdelayed module of XCIGALE. We further derived the SFR value from Kennicutt, 1998 relation $\log(\text{SFR/M}_\odot\text{yr}^{-1}) = \log(L_{FIR}/\text{ergs}^{-1}) - 43.34$, assuming $\log(L_{FIR}) \approx \log(L_{dust})$. The result showed SFR $= 0.59 \pm 0.04$ M$_\odot$yr^{-1}, which is compatible with the XCIGALE value. The fit shows a dust mass $\sim 4.56 \times 10^{36}$ kg at radius 9" (~ 600 pc). In comparison, from the ALMA observation at 0.1" ($\sim 3 - 4$ pc), the derived dust mass $\sim 6 \times 10^{35}$ kg (García-Burillo et al., 2021a), showing most of the dust concentration is in the nuclear region.

Table 12: Physical parameters of NGC 6300 from best-fit SED

| Model Component	Parameters	Units	Values
AGN	agn.fracAGN		0.23 ± 0.04
	agn.t		5.71 ± 1.43
	xray.alpha_ox		-1.25 ± 0.04
	xray.gam		1.78 ± 0.08
	agn.accretion_power	W $\times 10^{35}$	4.52 ± 0.90
	agn.disk_luminosity	W $\times 10^{33}$	4.39 ± 3.43
	agn.luminosity	W $\times 10^{35}$	4.01 ± 0.73
Dust and Stellar History	dust.alpha		2.06 ± 0.05
	dust.qpah		3.01 ± 0.69
	dust.umin		5.29 ± 1.30
	dust.mass	kg $\times 10^{36}$	4.56 ± 0.69
	dust.luminosity	W $\times 10^{36}$	1.29 ± 0.08
	sfh.age_main	Myr	4025.81 ± 571.91
	sfh.sfr	$M_\odot$ yr^{-1}	0.19 ± 0.02
	stellar.lum	W $\times 10^{36}$	2.25 ± 0.11
	stellar.m_gas	$M_\odot$ $\times 10^9$	1.69 ± 0.23
	stellar.m_star	$M_\odot$ $\times 10^9$	2.22 ± 0.25
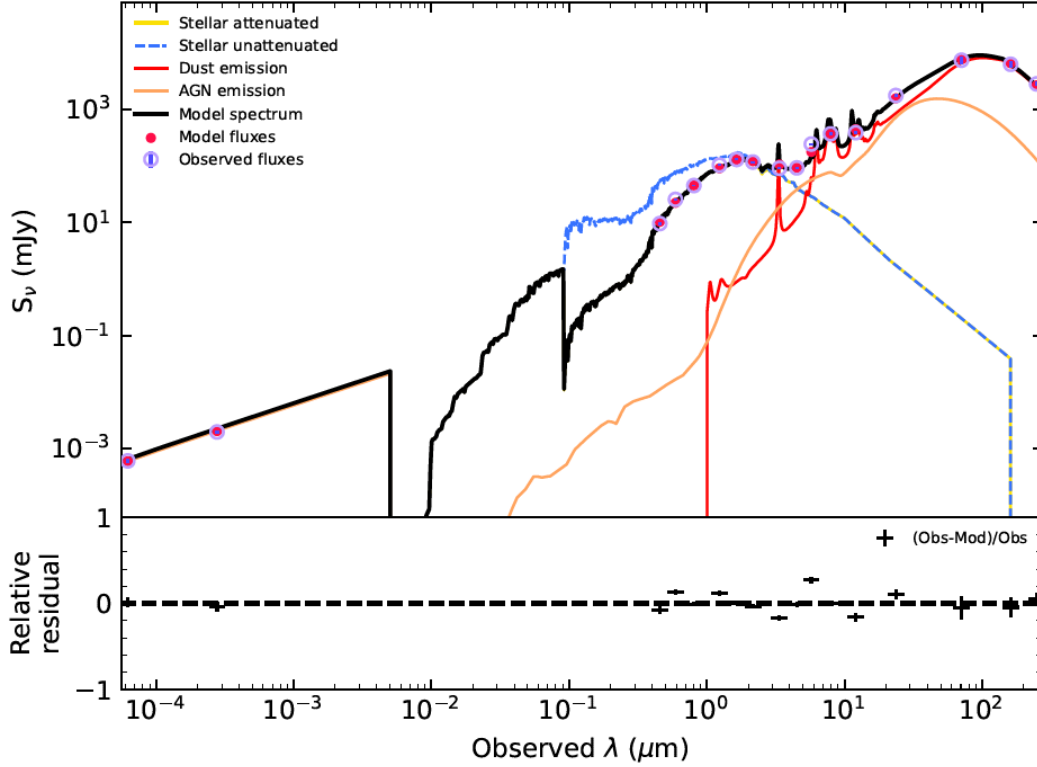
Figure 19: SED fitting of NGC 6300 using `XCIGALE`: with AGN (orange line), host dust or stellar absorption (blue dashed line) and host dust emission (red solid line) components.

4.5 Summary and conclusions

We have analysed multi-epoch X-ray data of NGC 6300 from 2007 to 2020. Using physically motivated X-ray torus models, we have studied column density and flux variability of the X-ray spectra within the energy range 0.8 keV to 50.0 keV. We also estimated torus properties like inclination angle, covering factor, torus cloud dispersion, average column density and others. For a comprehensive picture of the nuclear obscuring medium, we used the X-ray results to fit optical-FIR SED over photometric data points. In this section, we summarise our conclusions:

1. NGC 6300 was reported as a changing-look AGN candidate. But in agreement

with the results of last ~ 20 years, even with the *Chandra* observation of 2020, this source doesn't show any $N_{H,LOS}$ variability. We used both smooth and clumpy torus models, to study the statistical significance of any variability nature along the LOS column density. But all the models agree that the source is non-variable. In conclusion, we observe the source through a Compton-Thin region.

2. While there is no $N_{H,LOS}$ variability, the observation of 2020 showed a significant flux variability in the energy band E= $0.8 - 7.0$ keV. The flux dropped by $\sim 40 - 50\%$ in comparison with all the other observations, since 2007. Two of the three torus models also confirm with high statistical significance that there is an existing signature of intrinsic flux variability for this source.

3. All the models confirm clumpy torus structure. The model `UXCLUMPY` predicts the presence of the inner CT-ring of gaseous medium is responsible for the reflection dominated spectra. The $N_{H,LOS}$ values are ~ 10 times smaller than the `borus02` calculated $N_{H,avr}$ which is the column density from the reflection dominated region.

4. Considering the reflecting medium is same as the obscuring medium of the torus, we are observing the torus of NGC6300 along an almost homogeneous gas distribution with moderately over-dense and under-dense regions. `XCLUMPY` shows that, along the equatorial region, the torus gets highly over-dense compared to the LOS region. In our timescale, we estimated to have observed $\sim 5 \times 10^{-4} - 3 \times 10^{-3}$ pc angular region of the torus. We also roughly estimated the torus cloud sizes to be within $\sim 5 \times 10^{-7} - 2 \times 10^{-4}$ pc, from the observations of last 13 years.

5. The mean bolometric luminosity is evaluated from the optical-IR SED fitting and X-ray spectral fitting. We further estimated sub-eddington accretion ($\lambda_{Edd} \sim 2 \times 10^{-3}$), which falls within the range of ADAF accretion flow, with geometrically thick disk.

6. SED fitting on optical-IR photometry validate the obscuring nature of torus. We find the mid-IR photometry SED fitting can accurately proxy the X-ray luminosity. Further calculation shows shows sub-Eddington accretion, with high dust concentration in the nuclear region.

7. Joint X-ray and mid-IR analysis of AGN SED helps to characterizes the obscuring nature of torus: IR emission of torus, optical depth, accretion rate, dust and gas

influence in obscuration, stellar influence. The results are consistent with recent Alma observations.

5 Summary and Future Aspects

In this thesis, I have analysed the obscuring properties of the torus in local obscured AGN using physically motivated X-ray torus models. Using X-ray spectral analysis, I have also presented an updated census on the CT-AGN population in the local universe and its effect on the CXB. I have also conducted a multi-band SED fitting to characterise the different torus properties.

5.1 Scientific purpose

Most of the CXB radiation from 1 keV to 100 keV is the result of AGN emission (e.g, Gilli et al., 2007). The contribution of unobscured AGN (having absorbing column density column density $<10^{22}$ cm^{-2}) to the CXB is almost completely resolved into point-like sources, thanks to the X-ray observations, especially at E<10 keV. However, the detection of the obscured AGN is found to be challenging, although they are responsible for a significant fraction ($\sim 40\%$ at the peak; Ajello et al., 2008) of the CXB emission, from which the most obscured (N$_H$>10^{24} cm^{-2}) AGN (CT-AGN) contributes $15 - 20\%$. Besides, in the local universe ($z < 0.1$), the CT-AGN fraction (10-20%, Comastri, 2004; Ricci et al., 2015a) is much lower than what is expected from CXB population synthesis models (20-50%, Gilli et al., 2007; Ueda et al., 2014; Ananna et al., 2019). Therefore, there is a significant gap between the observations of heavily obscured AGN like CT-AGN and population synthesis model predictions. This discrepancy is most likely due to an observational bias in the current surveys.

In heavily obscured sources, Compton scattering and absorption by the obscuring torus can significantly reduce the source flux, even above 10 keV (Burlon et al., 2011). Only a small fraction of the primary X-ray emission at energies E> 10 keV pierces through the dusty torus for CT AGN. At larger column densities, the indirect (i.e., scattered) X-ray emission becomes more visible than the primary emission, making CT AGN sources very hard to get detected. Therefore, observational biases must be taken into account to compute the CT AGN fraction. After using the reflection component from

the obscuring torus models such as `MYTorus`, Burlon et al., 2011 showed a significant increase of CT-AGN fraction (from 5% to 20%) in their *Swift-BAT* sample of ~ 200 local AGN ($z < 0.1$). This result clearly showed that, once taking care of the additional effects of Compton scattering and absorption in the X-ray spectra, significantly improve the observational biases. To properly take care of these biases and discover the missing CT-AGN population, a large sample of low redshift AGN is needed to be observed in both the soft band (0.3–10 keV) and hard band (> 10 keV), using physically motivated X-ray torus models. These models can characterize the spectral shape of the observed X-ray SED and classify properly the AGN obscuration by estimating the spectral parameters such as the photon index, column density, covering factor.

One of the ultimate goals of Clemson-INAF CTAGN research group[24] is to identify and characterize the properties of obscured AGN at $z < 0.05$ (d< 200 Mpc). This group has already selected 55 local CT-AGN candidates which have archival *NuSTAR* data (i.e., covering also the E> 10 keV spectral region), from the volume limited sample of 100 month *Swift-BAT* catalog[25]. 48 of them have been analysed and published using `MYTorus` and `borus02` (e.g., Zhao, Marchesi, and Ajello, 2019; Marchesi, Ajello, Zhao, Marcotulli, et al., 2019; Traina et al., 2021; Torres-Albà et al., 2021). In the first part of my thesis, I have worked on the remaining seven CT-AGN candidates using the two above mentioned models. For a better characterization of the obscuring torus, in the second part of my thesis, I have used the most up-to-date uniform and clumpy torus models (such as `borus02`, `UXCLUMPY` and `XCLUMPY`) over a local CTn AGN: NGC 6300, which have multi-epoch X-ray archival data (over a timespan of 20 years). Since NGC 6300 was already classified to have a clumpy torus, I have used the physically motivated clumpy torus models for a better understanding of the torus structure. This is one of the sources from Zhao et al., 2021 sample of obscured CTn AGN population in local universe, which have several epochs of observation in both soft and hard X-ray band. This source was initially identified as a 'transient' or 'variable' AGN (Leighly et al., 1999; Guainazzi, 2002). Along with X-ray spectral analysis, for a better characterization of the dusty torus, I also applied multi-wavelength SED fitting using photometric data from optical to FIR band. In the following subsections, I will briefly mention the results of the analyses carried out so far and the investigations we planned to do in the coming future.

---

[24]https://science.clemson.edu/ctagn/
[25]http://bat.ifc.inaf.it/100m_bat_catalog/100m_bat_catalog_v0.0.htm

5.2 Investigation on torus

5.2.1 Variability Studies

One of the main objectives of this thesis is to measure the variability in the obscuring medium ($N_{H,los}$) and the variability of the intrinsic emission. Through multi-epoch X-ray monitoring of these obscured sources (MCG-02-12-017, NGC 4180, NGC 2788A, NGC 1106, ESO 406-G004, 2MASX 20145928+2523010 and ESO 138-G001), we have studied the LOS column density variability and found the inhomogeneity in the circumnuclear cloud distribution. Previous analysis of some obscured AGN have reported extreme variability, and even a 'changing-look' nature from CT to Compton-thin or vice versa; for example, NGC 7582 (Bianchi et al., 2009; Rivers et al., 2015), IC 751 (Ricci et al., 2016), and NGC 1358 (Marchesi et al., 2022). In my sample from Table 1, 2MASX J20145928+2523010 shows strong variability over a three-year time span. On the other hand, ESO138 G-001 shows almost no variability even after a seven-year observational gap. In order to obtain a clearer picture of the variability of such sources which shows possibilities of flux and/or column density variability, we would need follow-up observations with longer exposures over timescales from weeks to years.

NGC 6300 have 10 observations from 2007 to 2020, including long ($\sim$ 1 day) and short exposure ($\sim$ 3 hours), making it an ideal candidate to study X-ray variability. I used two statistical techniques to test these variabilities: Tension Statistics and Null Hypothesis from χ^2_{Red}. These statistical method show that the source is definitely variable, but not purely $N_{H,los}$ variable. Instead, with high statistical significance, it is found that there is intrinsic flux variability for this source. The 2020 *Chandra* observation of NGC 6300 shows a significant drop in flux (by $\sim 40\% - 50\%$) within the energy band E= 0.8-7.0 keV, in comparison with the other observations. This source was identified as a 'changing-look' AGN candidate, from CT to CTn phase, in the early 2000s, by studying the `RXTE` and `BeppoSAX` data observations. However, since then, it maintained a constant $N_{H,los}$ and flux, with the exception of the 2020 observation. In Torres-Albà et al., 2023a, a similar kind of work was done for a sample of twelve AGN, where five of them showed clear column density variability. ombining the already published results, with those of incoming papers, for twelve more sources in Pizzetti et al. (in prep.), Mrk 477 and NGC 7582 in Torres-Albà et al. (in prep.) and NGC 4507 in Cox et al. (in prep.), will provide a LOS column density variability study over the source sample of $\sim$ 30 obscured CTn AGN, selected from Zhao et al.,

2021. In future, we will ask for more observations on transient candidates like NGC 6300, in both hard ($¿$10 keV) and soft band ($¡$10 keV) for a better characterization of the obscuring medium and study variability.

5.2.2 Torus properties: X-ray and mid-IR SED fitting

Fitting the X-ray data with all the contemporary torus models indicates that most of the sources have clumpy torus structure. Furthermore, in Figure 15, the $N_{\rm H,LOS}$ vs $N_{\rm H,avr}$ plot is shown for the all the previous results of the CT-AGN candidates analysed by the Clemson-INAF group. The $N_{\rm H,LOS}$ is LOS column density that absorbs the primary coronal emission, whereas the $N_{\rm H,avr}$ is the average column density of the torus calculated from the reflection component of the X-ray spectra, which is expected to be originated from Compton scattering inside the torus. Therefore, the sources where $\frac{N_{\rm H,LOS}}{N_{\rm H,avr}} \neq 1$ are classified to have clumpy torus, as the region responsible for the reflection component is either over-dense or under-dense compared to LOS column density. Only 12 sources ($\sim$ 22% of the CI-CTAGN sample) show homogeneous torus. The remaining 43 sources ($\sim$ 78%) instead show significant inhomogeneity. In particular, at the 3 σ level confidence, 34 sources ($\sim$ 62%) show completely inhomogeneous tori within their error ranges. This phenomenon aligns with the expected outcomes of the CCA scenario, wherein multi-phase clouds persistently traverse the mesoscale ($\sim$ 1 − 100 pc), intermittently obstructing the LOS. The remaining gas, which is undergoing fewer inelastic collisions and reduced angular momentum cancellation, tends to aggregate in a torus-like configuration at this scale (Gaspari et al., 2017). Thus, it can be inferred that a substantial majority (approximately 78%) of obscured AGN in our sample exhibit a distinctly clumpy torus structure. It is also important to note that the $N_{\rm H,LOS}$ and $N_{\rm H,avr}$ are significantly uncorrelated. Using Pearson correlation for all 55 sources, we obtained that the correlation coefficient $\rho \approx 0.003$, which is almost close to zero. This also suggests that all heavily obscured AGN, with CT column density along the LOS, are not necessarily composed of CT cloud distribution from the reflection region of torus. From hydrodynamical simulations (see e.g. Gaspari et al., 2020), a realistic torus is a composition of multi-phase and multi-scale clouds, whose integral (e.g. density) can substantially change along each LOS. So, due to extensive clumpy nature and strong non-correlation between the LOS and average column density, heavily obscured AGN are strong candidates for showing changing-look nature. More observation these kind of AGN clumpy torus are required for further investigation.

In case of NGC 6300, we have 13 years of observation. So, we have an almost homogeneous gas distribution with moderately over-dense and under-dense regions along the LOS. I applied the clumpy torus models such as `XCLUMPY` and `UXCLUMPY` to properly characterize the reflection medium. The `XCLUMPY` model shows, along the equatorial region, the torus gets highly over-dense compared to the LOS region. In our timescale, we estimated to have observed $\sim 5 \times 10^{-4} - 3 \times 10^{-3}$ pc angular region of the torus, along the LO. We also roughly estimated the torus cloud sizes from the eclipse event of the accretion disk, is within $\sim 5 \times 10^{-7} - 2 \times 10^{-4}$ pc. The $N_{\mathrm{H,LOS}}$ values are ~ 10 times smaller than the `borus02` calculated $N_{\mathrm{H,avr}}$ which is the column density from the reflection dominated region. The model `UXCLUMPY` predicts the presence of the inner CT-ring of gaseous medium is responsible for the reflection dominated spectra. Using SED fitting, we estimated the properties like optical depth $\tau = 5.71 \pm 1.43$, intrinsic AGN luminosity, α_{ox}, giving a more comprehensive idea of the obscuration and AGN. The X-ray spectra + SED fitting on NGC 6300 is the pilot project. In the next months, we would like to expand this multiwavelength analysis on four local obscured AGN from Zhao et al., 2021, Torres-Albà et al., 2021 and Sengupta et al., 2023: NGC 6552, NGC 1106, Mrk 622 and Mrk 477. Two of these sources are uniform and two are clumpy, and are characterized by a wide range of covering factors. They also have large number of observations in the optical-FIR band for aperture photometry, which would be used for SED fitting.

5.3 Census of CT-AGN population and CXB

One of the aims of this thesis is to provide a census as complete as possible, of the local ($z < 0.05$) CT-AGN population, using all the available archival *NuSTAR* data from the volume limited sample of *Swift-BAT* 100 month catalog. In my analysis (Sengupta et al., 2023), I have found that of the seven analyzed CT-AGN candidates, only three comes out as CT-AGN: NGC 1106, NGC 4180, NGC 2788A. This updates the total number of *NuSTAR*-confirmed (i.e., from hard X-ray flux limited selection) CT-AGN to 35 for $z < 0.05$, which is $\sim 8\%$ of the total AGN population (414) within the same redshift in the 100 month BAT catalogue. This observed value is still relatively far below the value predicted by the CXB population synthesis models ($\sim 20\% - 50\%$). Our results also update the CT-AGN fraction at $z < 0.01$ to $\sim 22\% \pm 5.9\%$. The fraction of CT-AGN drops with higher redshifts ($z > 0.01$) because the CT-AGN sources become too faint to be detected by *Swift-BAT* (Koss et al. 2016). This clearly

suggests that a significant fraction of heavily obscured AGN are missed even by a hard-X-ray coded-mask telescope such as *Swift-BAT*. Thus, we need more high-quality and sensitive X-ray data on the obscured AGN population, especially at energies above 10 keV from *NuSTAR*. *NuSTAR* data, together along with sensitive soft X-ray (2-10 keV) observations from telescopes like *Chandra*, XMM-*Newton*, are needed to reliably confirm the CT nature of AGN and accurately study the properties of their obscuring tori. Eventually, it will help to complete the census and understand the comprehensive picture of the CXB emission sources.

A   Tables of X-Ray spectra

Table 13: Summary of best-fit solutions of NuSTAR data using different models for NGC 4180

Model	MyTorus Edge-on	MyTorus Face-on	borus02
χ^2/dof	76/64	84/64	76/62
C_{Ins}	$1.47^{+0.27}_{-0.21}$	$1.48^{+0.26}_{-0.22}$	$1.47^{+0.26}_{-0.21}$
Γ	$1.66^{+0.39}_{-*}$	$1.40^{+0.22}_{-*}$	$1.55^{+0.44}_{-*}$
C_{Tor}	—	—	$0.88^{+*}_{-0.77}$
θ_{Inc}	—	—	49^{+12}_{-*}
$N_{\mathrm{H,z}}$	$6.10^{+*}_{-4.30}$	$1.49^{+0.36}_{-0.24}$	$1.78^{+1.40}_{-0.51}$
$N_{\mathrm{H,S}}$	$1.97^{+0.33}_{-0.73}$	$3.98^{+1.08}_{-*}$	$1.74^{+2.82}_{-1.08}$
$f_s 10^{-2}$	$0.40^{+1.02}_{-0.20}$	$0.55^{+1.05}_{-*}$	$2.27^{+1.31}_{-1.68}$
$F_{2-10\mathrm{keV}}$	$1.34^{+0.22}_{-*}$	$1.30^{+0.15}_{-*}$	$1.33^{+3.82}_{-*}$
$F_{10-50\mathrm{keV}}$	$4.49^{+20.85}_{-*}$	$4.73^{+9.22}_{-*}$	$4.54^{+0.39}_{-*}$
$L_{2-10\mathrm{keV}}$	$11.01^{+51.43}_{-*}$	$2.72^{+3.18}_{-0.47}$	$3.21^{+7.78}_{-1.38}$
$L_{10-50\mathrm{keV}}$	$19.05^{+89.05}_{-*}$	$7.14^{+0.38}_{-4.27}$	$6.63^{+15.99}_{-2.85}$

We summarise here the best-fits of *NuSTAR* spectra using different torus models between 3 and 50 keV, referred in Section 3.4. The statistics and degrees of freedom for each fit are also reported. The parameters are reported as in Table 2 if not mentioned otherwise.

C_{Ins} is the ratio of cross-normalisation constant between two *NuSTAR* observations through their FPMA detectors.

Intrinsic luminosity between 2 and 10 keV in 10^{41} erg s^{-1}.

Intrinsic luminosity between 10 and 50 keV in 10^{41} erg s^{-1}.

Table 14: Summary of best-fit solutions of *Swift-XRT* and NuSTAR data using different models for NGC 2788A

Model	MyTorus Edge-on	MyTorus Face-on	borus02
C-Stat/dof	136/153	116/153	116/151
C_{Ins_1}	$1.12^{+0.58}_{-0.38}$	$0.93^{+0.40}_{-0.26}$	$0.94^{+0.40}_{-0.27}$
C_{Ins_2}	$1.36^{+0.70}_{-0.46}$	$1.13^{+0.48}_{-0.31}$	$1.14^{+0.47}_{-0.32}$
Γ	$1.56^{+0.20}_{-*}$	$1.75^{+0.17}_{-0.24}$	$1.95^{+0.32}_{-0.31}$
C_{Tor}	—	—	$0.49^{+0.47}_{-0.28}$
θ_{Inc}	—	—	63^{+9}_{-16}
$N_{H,z}$	$3.95^{+*}_{-1.91}$	$1.95^{+0.41}_{-0.28}$	$2.34^{+*}_{-0.58}$
$N_{H,S}$	$1.25^{+0.24}_{-0.60}$	$3.74^{+3.74}_{-1.37}$	$4.26^{+18.43}_{-2.54}$
$f_s\ 10^{-2}$	$0.23^{+0.26}_{-0.13}$	$0.07^{+0.25}_{-*}$	$0.03^{+0.14}_{-*}$
$F_{2-10keV}$	$4.36^{+129.64}_{-2.82}$	$4.56^{+1.73}_{-2.10}$	$4.50^{+7.26}_{-*}$
$F_{10-50keV}$	$1.15^{+1.65}_{-*}$	$1.12^{+0.06}_{-0.52}$	$1.11^{+0.08}_{-0.64}$
$L_{2-10keV}$	$9.48^{+11.06}_{-5.71}$	$5.33^{+4.14}_{-2.82}$	$11.29^{+27.28}_{-*}$
$L_{10-50keV}$	$19.10^{+22.31}_{-11.50}$	$8.04^{+6.23}_{-4.26}$	$12.33^{+29.80}_{-*}$

We summarise here the best-fits of joint *Swift-XRT–NuSTAR* spectra using different torus models at 0.8-50 keV, referred in Section 3.4. The statistics and degrees of freedom for each fit are also reported. The parameters are reported as in Table 2 if not mentioned otherwise.
$C_{Ins_1} = C_{FPMA/XRT}$ is the cross-calibration constant between *NuSTAR* observation of 2019 and *Swift-XRT*. $C_{Ins_2} = C_{FPMA/XRT}$ is the cross-calibration constant between *NuSTAR* observation of 2020 and *Swift-XRT*. Flux between 10–50 keV in 10^{-11} erg cm^{-2} s^{-1}.

Table 15: Summary of best-fit solutions of XMM-Newton and NuSTAR data using different models for NGC 1106

Model	MyTorus Edge-on	MyTorus Face-on	borus02
χ^2/dof	357/295	310/295	304/293
C_{Ins_1}	$0.75^{+0.15}_{-0.14}$	$1.05^{+0.22}_{-0.19}$	$1.07^{+0.24}_{-0.19}$
C_{Ins_2}	$0.92^{+0.15}_{-0.17}$	$1.28^{+0.27}_{-0.22}$	$1.29^{+0.28}_{-0.23}$
Γ	$1.40^{+0.00}_{-*}$	$1.68^{+0.11}_{-0.22}$	$1.92^{+0.44}_{-0.35}$
C_{Tor}	—	—	$0.87^{+0.11}_{-0.24}$
θ_{Inc}	—	—	37^{+37}_{-9}
$N_{H,z}$	$4.00^{+1.73}_{-0.65}$	$3.43^{+*}_{-0.76}$	$4.79^{+*}_{-1.96}$
$N_{H,S}$	$1.46^{+0.18}_{-0.12}$	$7.98^{+*}_{-3.48}$	$4.83^{+*}_{-1.38}$
$f_s\ 10^{-2}$	$0.71^{+0.26}_{-0.19}$	$0.72^{+0.71}_{-0.36}$	$0.46^{+1.04}_{-0.38}$
kT	$0.97^{+0.17}_{-0.11}$	$1.01^{+0.47}_{-0.11}$	$0.99^{+0.32}_{-0.12}$
kT	$0.38^{+0.57}_{-0.31}$	$0.42^{+0.21}_{-0.10}$	$0.42^{+0.21}_{-0.11}$
$F_{2-10keV}$	$2.73^{+94.62}_{-2.70}$	$2.63^{+1.87}_{-2.22}$	$2.60^{+11.20}_{-2.45}$
$F_{10-50keV}$	$7.62^{+23.18}_{-7.61}$	$7.83^{+3.02}_{-7.59}$	$7.98^{+11.97}_{-7.97}$
$L_{2-10keV}$	$6.87^{+1.91}_{-1.66}$	$3.68^{+1.58}_{-0.95}$	$5.02^{+5.75}_{-3.97}$
$L_{10-50keV}$	$18.04^{+5.01}_{-4.37}$	$6.16^{+2.65}_{-1.60}$	$5.50^{+6.29}_{-4.35}$

We summarise here the best fits of joint XMM-*Newton*–*NuSTAR* spectra using different torus models at 0.6-50 keV, referred to in Section 3.4. The statistics and degrees of freedom for each fit are also reported. The parameters are reported as in Table 2 if not mentioned otherwise.

$C_{Ins} = C_{FPMA/PN}$ is the cross-calibration constant between *NuSTAR* observation of 2020 and XMM-*Newton* observation of 2019.

Table 16: Summary of best-fit solutions of Chandra and NuSTAR data using different models for ESO406-G004

Model	MyTorus Edge-on	MyTorus Face-on	borus02
C-Stat/dof	84/86	84/86	83/84
C_{Ins_1}	$0.73^{+0.65}_{-0.30}$	$0.85^{+0.63}_{-0.36}$	$0.68^{+0.60}_{-0.07}$
C_{Ins_2}	$0.35^{+0.32}_{-0.15}$	$0.41^{+0.31}_{-0.18}$	$0.34^{+0.35}_{-0.06}$
Γ	$1.48^{+0.30}_{-*}$	$1.40^{+0.62}_{-*}$	$1.42^{+0.02}_{-*}$
C_{Tor}	—	—	0.10^{+*}_{-*}
θ_{Inc}	—	—	18^{+69}_{-*}
$N_{H,z}$	$0.85^{+0.43}_{-0.23}$	$0.73^{+0.27}_{-0.14}$	$0.79^{+0.04}_{-0.12}$
$N_{H,S}$	$0.49^{+1.11}_{-0.36}$	$1.30^{+0.73}_{-1.19}$	$4.97^{+*}_{-4.80}$
$f_s\ 10^{-2}$	$0.65^{+1.33}_{-0.62}$	$0.81^{+1.29}_{-*}$	$0.37^{+0.65}_{-*}$
kT	$0.51^{+0.20}_{-*}$	$0.52^{+0.19}_{-*}$	$0.52^{+0.18}_{-0.18}$
$F_{2-10keV}$	$3.41^{+1.37}_{-3.41}$	$3.19^{+5.52}_{-3.19}$	$3.56^{+3.47}_{-3.56}$
$F_{10-50keV}$	$3.50^{+0.19}_{-3.50}$	$3.61^{+10.58}_{-*}$	$3.56^{+5.54}_{-3.56}$
$L_{2-10keV}$	$6.77^{+8.68}_{-3.87}$	$3.97^{+26.51}_{-1.71}$	$6.47^{+0.42}_{-0.37}$
$L_{10-50keV}$	$15.58^{+19.96}_{-8.91}$	$10.27^{+68.51}_{-4.44}$	$16.55^{+1.07}_{-0.93}$

We summarise here the best-fits of joint *Chandra–NuSTAR* spectra using different torus models at 0.7-50 keV, referred to in section 3.4. The statistics and degrees of freedom for each fit are also reported. The parameters are reported as in Table 2 if not mentioned otherwise.

$C_{Ins_1} = C_{FPMA/ACIS}$ is the cross-calibration constant between *NuSTAR* observation of 2016 and *Chandra* observation of 2012.

$C_{Ins_2} = C_{FPMA/ACIS}$ is the cross-calibration constant between *NuSTAR* observation of 2020 and *Chandra* observation of 2012.

Table 17: Summary of best-fit solutions of XMM-*Newton*, *Chandra*, and NuSTAR data using different models for 2MASX J20145928+2523010

Model	MyTorus	MyTorus	borus02
	Edge-on	Face-on	
χ^2/dof	545/581	545/581	564/580
C_{Ins_1}	$1.98^{+0.16}_{-0.15}$	$1.98^{+0.16}_{-0.15}$	$1.98^{+0.15}_{-0.15}$
C_{Ins_2}	$1.32^{+0.08}_{-0.08}$	$1.32^{+0.08}_{-0.08}$	$1.31^{+0.08}_{-0.08}$
C_{Ins_3}	$1.95^{+0.16}_{-0.15}$	$1.95^{+0.16}_{-0.15}$	$1.94^{+0.14}_{-0.15}$
Γ	$1.79^{+0.10}_{-0.10}$	$1.77^{+0.11}_{-0.08}$	$1.52^{+0.04}_{-0.05}$
C_{Tor}	—	—	$1.00^{+*}_{-0.23}$
θ_{Inc}	—	—	18^{+*}_{-*}
$N_{\text{H,z}}$	$2.02^{+0.17}_{-0.16}$	$2.04^{+0.19}_{-0.15}$	$2.18^{+0.11}_{-0.13}$
$N_{\text{H,S}}$	$11.93^{+3.85}_{-2.86}$	$20.15^{+8.51}_{-6.33}$	$17.63^{+4.05}_{-4.75}$
$f_s\ 10^{-2}$	$0.68^{+0.40}_{-0.39}$	$0.42^{+0.44}_{-*}$	$1.06^{+0.40}_{-0.43}$
$F_{2-10\text{keV}}$	$1.83^{+0.04}_{-0.06}$	$1.83^{+0.05}_{-0.08}$	$1.81^{+0.04}_{-0.09}$
$F_{10-50\text{keV}}$	$5.04^{+0.21}_{-0.45}$	$5.07^{+0.46}_{-0.52}$	$6.81^{+0.41}_{-0.53}$
$L_{2-10\text{keV}}$	$6.27^{+1.09}_{-0.93}$	$5.95^{+1.18}_{-0.89}$	$8.20^{+0.70}_{-0.64}$
$L_{10-50\text{keV}}$	$8.76^{+1.53}_{-1.31}$	$8.52^{+1.69}_{-1.27}$	$17.57^{+1.50}_{-1.37}$

We summarise here the best-fits of joint XMM-*Newton*, *Chandra* and *NuSTAR* spectra using different torus models at 0.6-50 keV, referred to in Section 3.4.
$C_{Ins_1} = C_{ACIS/PN}$ is the cross-calibration constant between *Chandra* observation of 2018 and XMM-*Newton* observation of 2017.
$C_{Ins_2} = C_{FPMA/PN}$ is the cross-calibration constant between *NuSTAR* observation of 2017 and XMM-*Newton* observation of 2017.
$C_{Ins_3} = C_{FPMA/PN}$ is the cross-calibration constant between *NuSTAR* observation of 2020 and XMM-*Newton* observation of 2017.
'Line of sight' column density in $10^{22}\,\text{cm}^{-2}$.
Average column density from scattering in $10^{22}\,\text{cm}^{-2}$.
Flux between 2 and $10\,\text{keV}$ in 10^{-12} erg cm^{-2} s^{-1}.

Table 18: Summary of best-fit solutions of XMM-Newton and NuSTAR data using different models for ESO138-G001

Model	MyTorus Edge-on	MyTorus Face-on	borus02
χ^2/dof	2636/1818	2566/1818	2419/1816
C_{Ins_1}	$1.15^{+0.04}_{-0.04}$	$1.15^{+0.05}_{-0.05}$	$1.16^{+0.03}_{-0.05}$
C_{Ins_2}	$1.07^{+0.04}_{-0.04}$	$1.08^{+0.04}_{-0.04}$	$1.09^{+0.03}_{-0.05}$
Γ	$1.53^{+0.05}_{-0.05}$	$1.66^{+0.03}_{-0.05}$	$1.98^{+0.01}_{-0.03}$
C_{Tor}	—	—	$0.80^{+0.03}_{-0.12}$
θ_{Inc}	—	—	18^{+*}_{-*}
$N_{\mathrm{H,z}}$	$0.33^{+0.02}_{-0.02}$	$0.34^{+0.01}_{-0.02}$	$0.47^{+0.07}_{-0.06}$
$N_{\mathrm{H,S}}$	$1.47^{+0.60}_{-0.49}$	$3.00^{+0.37}_{-0.55}$	$10.35^{+0.08}_{-0.08}$
Fe K_α	$6.42^{+0.00}_{-0.01}$	$6.42^{+0.00}_{-0.01}$	$6.44^{+0.01}_{-0.01}$
Fe K_α norm 10^{-5}	$2.28^{+0.10}_{-0.11}$	$1.91^{+0.11}_{-0.10}$	$1.04^{+0.10}_{-0.13}$
f_s 10^{-2}	$7.46^{+1.07}_{-0.94}$	$8.14^{+0.67}_{-0.87}$	$3.22^{+0.10}_{-0.24}$
kT	$0.68^{+0.01}_{-0.01}$	$0.68^{+0.01}_{-0.01}$	$0.74^{+0.01}_{-0.01}$
$F_{2-10\mathrm{keV}}$	$2.25^{+0.04}_{-0.07}$	$2.24^{+0.04}_{-0.05}$	$2.24^{+0.11}_{-0.27}$
$F_{10-50\mathrm{keV}}$	$1.42^{+0.03}_{-0.11}$	$1.44^{+0.03}_{-0.09}$	$1.43^{+0.06}_{-0.09}$
$L_{2-10\mathrm{keV}}$	$11.59^{+2.25}_{-1.88}$	$12.11^{+0.95}_{-2.04}$	$3.61^{+0.30}_{-0.94}$
$L_{10-50\mathrm{keV}}$	$24.51^{+4.75}_{-3.97}$	$20.90^{+1.65}_{-3.52}$	$3.34^{+0.28}_{-0.87}$

We summarise here the best-fits of joint XMM-*Newton*–*NuSTAR* spectra using different torus models at 0.6-50 keV, referred to in Section 3.4.

$C_{Ins_1} = C_{FPMA/PN}$ is the cross-calibration constant between *NuSTAR* observation of 2016 and XMM-*Newton* observation of 2013.

$C_{Ins_2} = C_{FPMA/PN}$ is the cross-calibration constant between *NuSTAR* observation of 2020 and XMM-*Newton* observation of 2013.

Energy of the Iron K_α line in keV.

Normalization of line component depicting total photons in $\mathrm{cm}^{-2}\,\mathrm{s}^{-1}$.

Flux between 2 and 10 keV in 10^{-12} erg cm^{-2} s^{-1}.

Flux between 10 and 50 keV in 10^{-11} erg cm^{-2} s^{-1}.

Intrinsic luminosity between 2 and 10 keV in 10^{41} erg s^{-1}.

Intrinsic luminosity between 2 and 10 keV in 10^{41} erg s^{-1}.

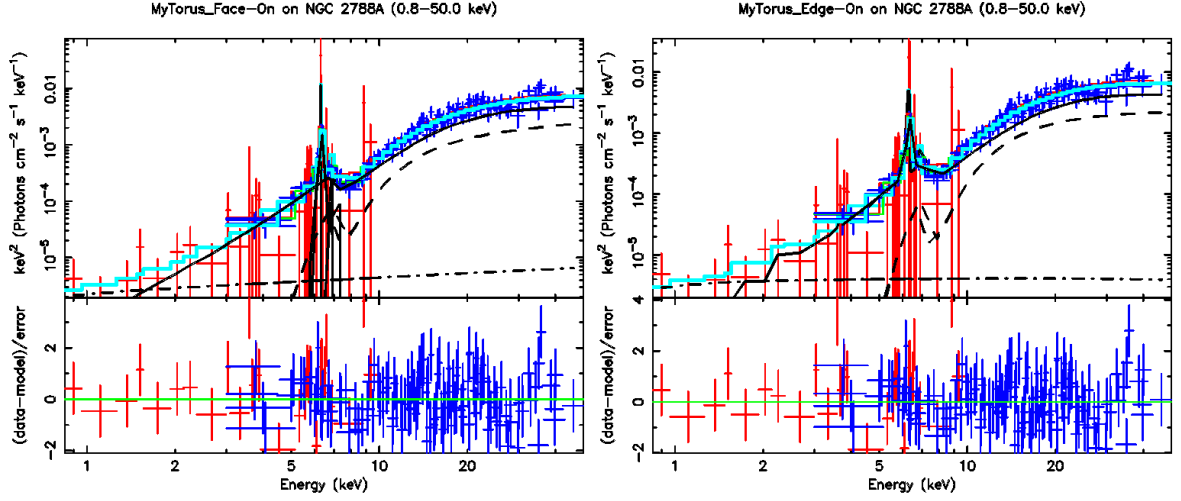# B   Figures of X-Ray Spectra

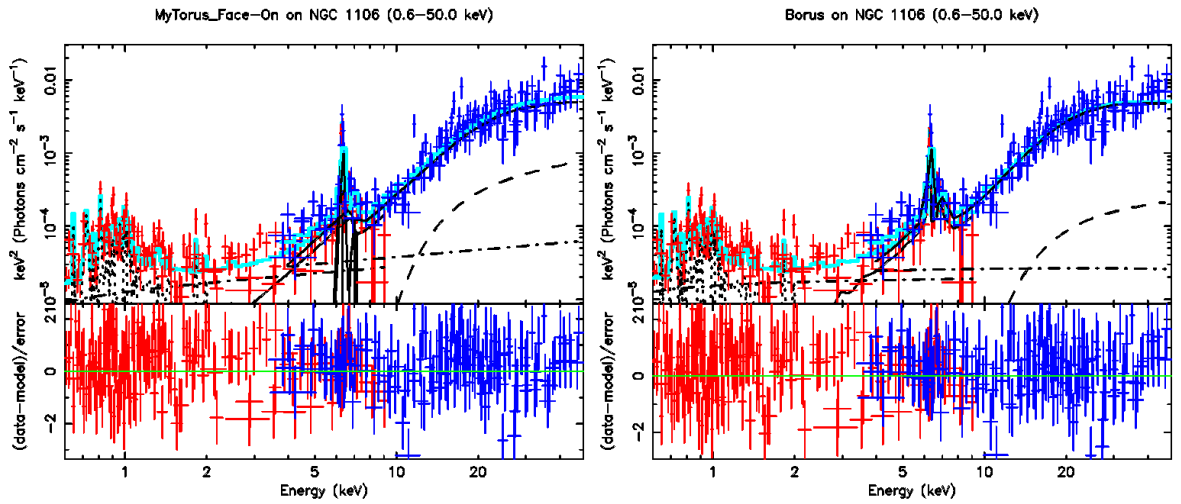Figure 20: Same as Figure 13, for NGC 2788A, without mekal.
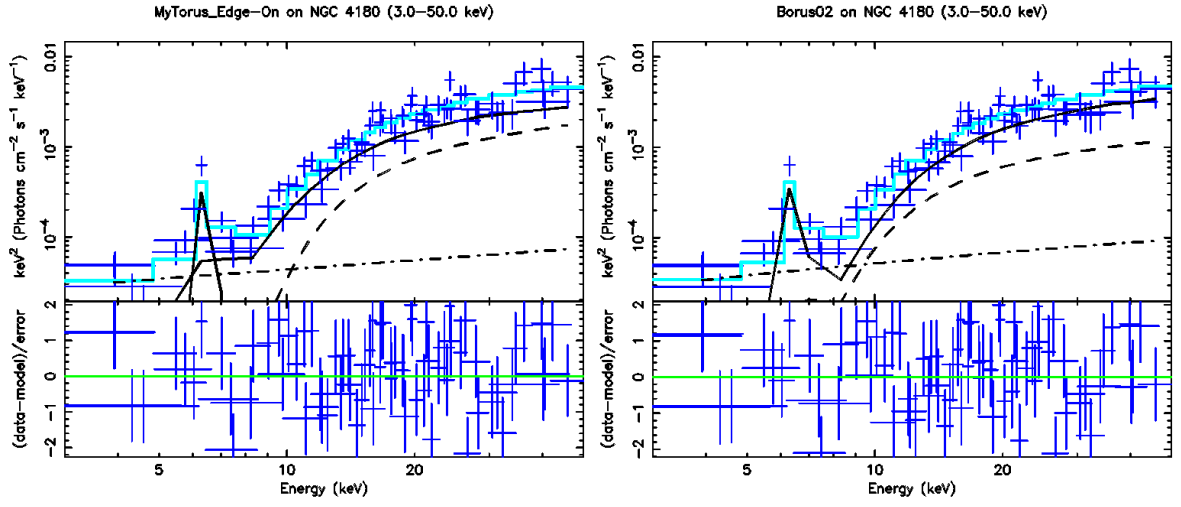

Figure 21: Same as Figure 13, for NGC 1106.

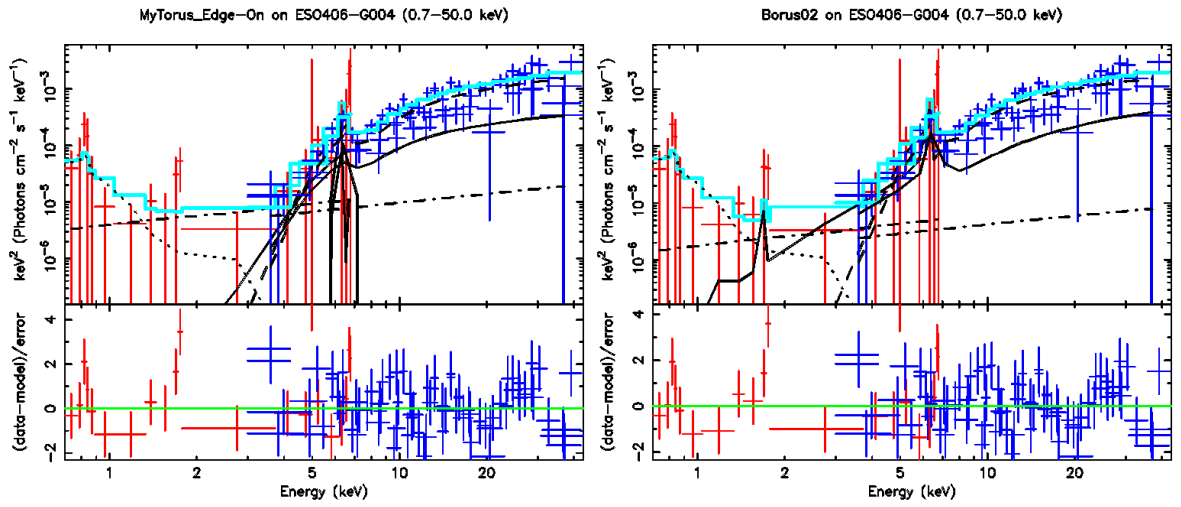Figure 22: Same as Figure 13, for NGC 4180, without any soft X-ray points and mekal.

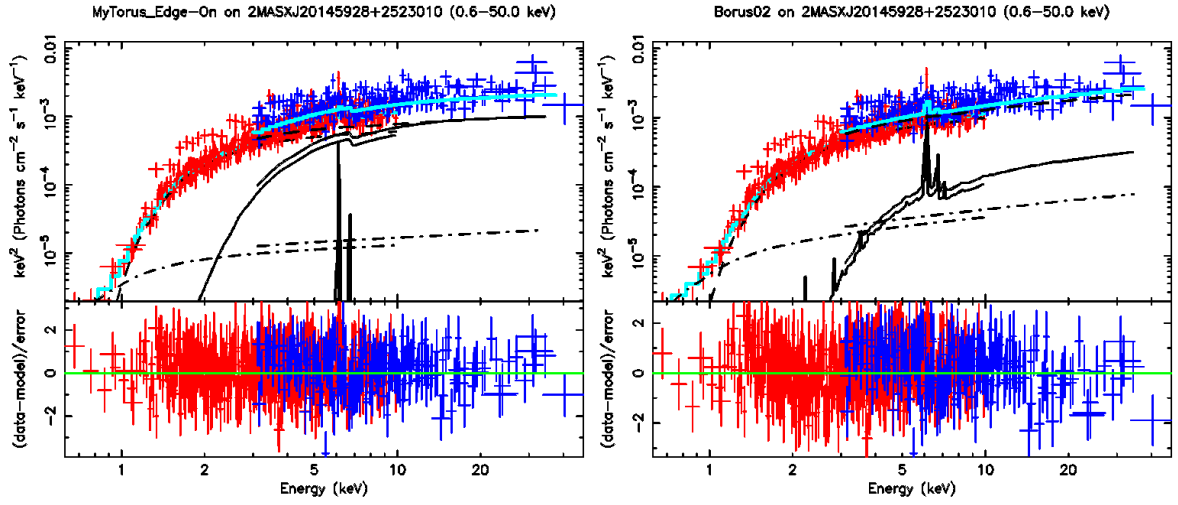Figure 23: Same as Figure 13, for ESO406-G004.

Figure 24: Same as Figure 13, for 2MASXJ20145928+2523010, without mekal.
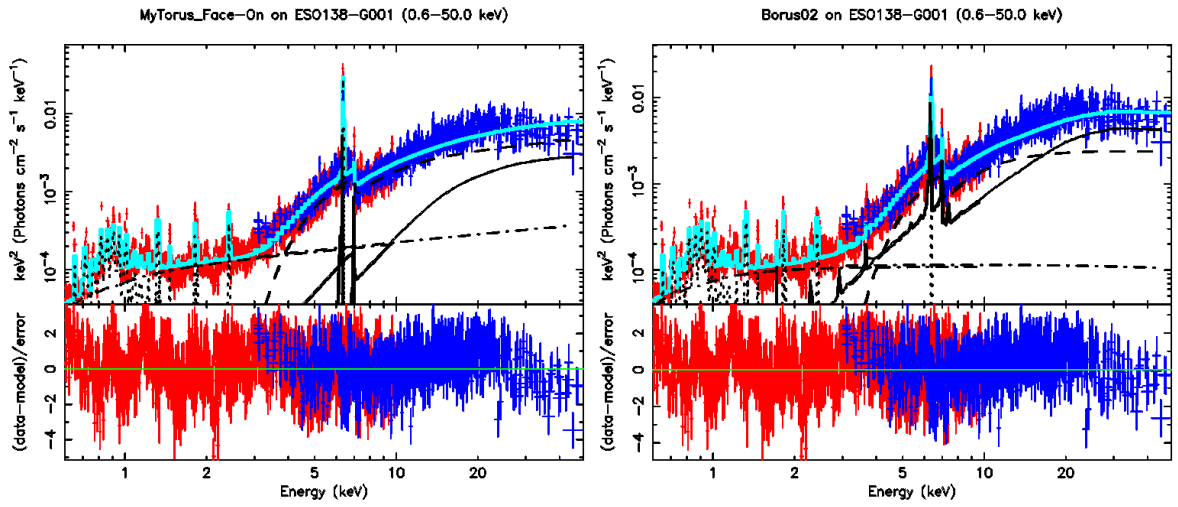

Figure 25: Same as Figure 13, for ESO138-G001, with extra four Gaussian line profiles (dot).

References

Aird, J., Alexander, D. M., Ballantyne, D. R., Civano, F., Del-Moro, A., Hickox, R. C., Lansbury, G. B., Mullaney, J. R., Bauer, F. E., Brandt, W. N., et al. (2015). The nustar extragalactic survey: First direct measurements of the 10 kev x-ray luminosity function for active galactic nuclei at z¿ 0.1. *The Astrophysical Journal*, *815*(1), 66.

Ajello, Greiner, J., Sato, G., Willis, D., Kanbach, G., Strong, A., Diehl, R., Hasinger, G., Gehrels, N., Markwardt, C., et al. (2008). Cosmic x-ray background and earth albedo spectra with swift bat. *The Astrophysical Journal*, *689*(2), 666.

Alexander, D. M., & Hickox, R. C. (2012). What drives the growth of black holes? *NAR*, *56*(4), 93–121. https://doi.org/10.1016/j.newar.2011.11.003

Alexander, D., Bauer, F., Brandt, W. N., Garmire, G., Hornschemeier, A., Schneider, D. P., & Vignali, C. (2003). Resolving the source populations that contribute to the x-ray background: The 2 ms chandra deep field-north survey. *Astronomische Nachrichten: Astronomical Notes*, *324*(1-2), 8–11.

Ananna, T. T., Treister, E., Urry, C. M., Ricci, C., Kirkpatrick, A., LaMassa, S., Buchner, J., Civano, F., Tremmel, M., & Marchesi, S. (2019). The Accretion History of AGNs. I. Supermassive Black Hole Population Synthesis Model. *ApJ*, *871*(2), Article 240, 240. https://doi.org/10.3847/1538-4357/aafb77

Anders, E., & Grevesse, N. (1989). Abundances of the elements: Meteoritic and solar. *GCA*, *53*(1), 197–214. https://doi.org/10.1016/0016-7037(89)90286-X

Andrae, R., Schulze-Hartung, T., & Melchior, P. (2010). Dos and don'ts of reduced chi-squared. *arXiv e-prints*, Article arXiv:1012.3754, arXiv:1012.3754. https://doi.org/10.48550/arXiv.1012.3754

Antonucci. (1993). Unified models for active galactic nuclei and quasars. *Annual review of astronomy and astrophysics*, *31*, 473–521.

Antonucci & Miller. (1985). Spectropolarimetry and the nature of ngc 1068. *The Astrophysical Journal*, *297*, 621–632.

Arnaud, K. A. (1996, January). XSPEC: The First Ten Years. In G. H. Jacoby & J. Barnes (Eds.), *Astronomical data analysis software and systems v* (p. 17, Vol. 101).

Asmus, D., Hönig, S. F., & Gandhi, P. (2016). The Subarcsecond Mid-infrared View of Local Active Galactic Nuclei. III. Polar Dust Emission. *ApJ*, *822*(2), Article 109, 109. https://doi.org/10.3847/0004-637X/822/2/109

Baes, M., Verstappen, J., De Looze, I., Fritz, J., Saftly, W., Vidal Pérez, E., Stalevski, M., & Valcke, S. (2011). Efficient Three-dimensional NLTE Dust Radiative Transfer with SKIRT. *ApJs*, *196*(2), Article 22, 22. https://doi.org/10.1088/0067-0049/196/2/22

Ballantyne, D. R. (2008). Obscuring Active Galactic Nuclei with Nuclear Starburst Disks. *ApJ*, *685*(2), 787–800. https://doi.org/10.1086/591048

Baloković, M., Brightman, M., Harrison, F. A., Comastri, A., Ricci, C., Buchner, J., Gandhi, P., Farrah, D., & Stern, D. (2018). New spectral model for constraining torus covering factors from broadband x-ray spectra of active galactic nuclei. *The Astrophysical Journal*, *854*(1), 42.

Barlow, R. (2002). Systematic Errors: facts and fictions. *arXiv e-prints*, Article hep-ex/0207026, hep–ex/0207026. https://doi.org/10.48550/arXiv.hep-ex/0207026

Barvainis, R. (1987). Hot Dust and the Near-Infrared Bump in the Continuum Spectra of Quasars and Active Galactic Nuclei. *ApJ*, *320*, 537. https://doi.org/10.1086/165571

Bennert, N., Jungwiert, B., Komossa, S., Haas, M., & Chini, R. (2006). Size and properties of the narrow-line region in Seyfert-2 galaxies from spatially-resolved optical spectroscopy. *AA*, *456*(3), 953–966. https://doi.org/10.1051/0004-6361:20065319

Bennett, C. L., Larson, D., Weiland, J. L., & Hinshaw, G. (2014). The 1% Concordance Hubble Constant. *ApJ*, *794*(2), Article 135, 135. https://doi.org/10.1088/0004-637X/794/2/135

Berta, S., Lutz, D., Santini, P., Wuyts, S., Rosario, D., Brisbin, D., Cooray, A., Franceschini, A., Gruppioni, C., Hatziminaoglou, E., Hwang, H. S., Le Floc'h, E., Magnelli, B., Nordon, R., Oliver, S., Page, M. J., Popesso, P., Pozzetti, L., Pozzi, F., Riguccini, L., Rodighiero, G., Roseboom, I., Scott, D., Symeonidis, M., Valtchanov, I., Viero, M., & Wang, L. (2013). Panchromatic spectral energy distributions of Herschel sources. *AA*, *551*, Article A100, A100. https://doi.org/10.1051/0004-6361/201220859

Bianchi, S., & Guainazzi, M. (2007, August). The nature of the soft X-ray emission in obscured AGN. In T. di Salvo, G. L. Israel, L. Piersant, L. Burderi, G. Matt, A. Tornambe, & M. T. Menna (Eds.), *The multicolored landscape of compact objects and their explosive origins* (pp. 822–829, Vol. 924). AIP. https://doi.org/10.1063/1.2774948

Bianchi, S., Piconcelli, E., Chiaberge, M., Bailón, E. J., Matt, G., & Fiore, F. (2009). How Complex is the Obscuration in Active Galactic Nuclei? New Clues from the Suzaku Monitoring of the X-Ray Absorbers in NGC 7582. *ApJ*, *695*(1), 781–787. https://doi.org/10.1088/0004-637X/695/1/781

Blandford & Payne, D. (1982). Hydromagnetic flows from accretion discs and the production of radio jets. *Monthly Notices of the Royal Astronomical Society*, *199*(4), 883–903.

Blandford & Znajek, R. L. (1977). Electromagnetic extraction of energy from kerr black holes. *Monthly Notices of the Royal Astronomical Society*, *179*(3), 433–456.

Boorman, P. G., Gandhi, P., Alexander, D. M., Annuar, A., Ballantyne, D. R., Bauer, F., Boggs, S. E., Brandt, W. N., Brightman, M., Christensen, F. E., Craig, W. W., Farrah, D., Hailey, C. J., Harrison, F. A., Hönig, S. F., Koss, M., LaMassa, S. M., Masini, A., Ricci, C., Risaliti, G., Stern, D., & Zhang, W. W. (2016). IC 3639—a New Bona Fide Compton-Thick AGN Unveiled by NuSTAR. *ApJ*, *833*(2), Article 245, 245. https://doi.org/10.3847/1538-4357/833/2/245

Boquien, M., Buat, V., & Perret, V. (2014). Impact of star formation history on the measurement of star formation rates. *AA*, *571*, Article A72, A72. https://doi.org/10.1051/0004-6361/201424441

Boquien, M., Burgarella, D., Roehlly, Y., Buat, V., Ciesla, L., Corre, D., Inoue, A. K., & Salas, H. (2019). CIGALE: a python Code Investigating GALaxy Emission. *AA*, *622*, Article A103, A103. https://doi.org/10.1051/0004-6361/201834156

Brightman & Nandra. (2011). An xmm–newton spectral survey of 12 μm selected galaxies–i. x-ray data. *Monthly Notices of the Royal Astronomical Society*, *413*(2), 1206–1235.

Bruzual, G., & Charlot, S. (2003). Stellar population synthesis at the resolution of 2003. *MNRAS*, *344*(4), 1000–1028. https://doi.org/10.1046/j.1365-8711.2003.06897.x

Buchner, J., & Bauer, F. E. (2017). Galaxy gas as obscurer - II. Separating the galaxy-scale and nuclear obscurers of active galactic nuclei. *MNRAS*, *465*(4), 4348–4362. https://doi.org/10.1093/mnras/stw2955

Buchner, J., Brightman, M., Nandra, K., Nikutta, R., & Bauer, F. E. (2019). X-ray spectral and eclipsing model of the clumpy obscurer in active galactic nuclei. *AA*, *629*, Article A16, A16. https://doi.org/10.1051/0004-6361/201834771

Buchner, J., Georgakakis, A., Nandra, K., Brightman, M., Menzel, M.-L., Liu, Z., Hsu, L.-T., Salvato, M., Rangel, C., Aird, J., et al. (2015). Obscuration-dependent evolution of active galactic nuclei. *The Astrophysical Journal*, *802*(2), 89.

Burlon, D., Ajello, M., Greiner, J., Comastri, A., Merloni, A., & Gehrels, N. (2011). Three-year swift-bat survey of active galactic nuclei: Reconciling theory and observations? *The Astrophysical Journal*, *728*(1), 58.

Burtscher, L., Meisenheimer, K., Tristram, K. R. W., Jaffe, W., Hönig, S. F., Davies, R. I., Kishimoto, M., Pott, J. .-., Röttgering, H., Schartmann, M., Weigelt, G., & Wolf, S. (2013a). A diversity of dusty AGN tori. Data release for the VLTI/MIDI AGN Large Program and first results for 23 galaxies. *AA*, *558*, Article A149, A149. https://doi.org/10.1051/0004-6361/201321890

Burtscher, L., Meisenheimer, K., Tristram, K. R., Jaffe, W., Hönig, S. F., Davies, R. I., Kishimoto, M., Pott, J.-U., Röttgering, H., Schartmann, M., et al. (2013b). A diversity of dusty agn tori-data release for the vlti/midi agn large program and first results for 23 galaxies. *Astronomy & Astrophysics*, *558*, A149.

Calzetti, D., Armus, L., Bohlin, R. C., Kinney, A. L., Koornneef, J., & Storchi-Bergmann, T. (2000). The Dust Content and Opacity of Actively Star-forming Galaxies. *ApJ*, *533*(2), 682–695. https://doi.org/10.1086/308692

Camps, P., & Baes, M. (2015). SKIRT: An advanced dust radiative transfer code with a user-friendly architecture. *Astronomy and Computing*, *9*, 20–33. https://doi.org/10.1016/j.ascom.2014.10.004

Capetti, A., Macchetto, F., Axon, D. J., Sparks, W. B., & Boksenberg, A. (1995). Hubble Space Telescope Imaging Polarimetry of the Inner Nuclear Region of NGC 1068. *ApJ Letters*, *452*, L87. https://doi.org/10.1086/309732

Casey, C. M. (2012). Far-infrared spectral energy distribution fitting for galaxies near and far. *MNRAS*, *425*(4), 3094–3103. https://doi.org/10.1111/j.1365-2966.2012.21455.x

Charlot, S., & Fall, S. M. (2000). A Simple Model for the Absorption of Starlight by Dust in Galaxies. *ApJ*, *539*(2), 718–731. https://doi.org/10.1086/309250

Chartas, G., Rhea, C., Kochanek, C., Dai, X., Morgan, C., Blackburne, J., Chen, B., Mosquera, A., & MacLeod, C. (2016). Gravitational lensing size scales for quasars. *Astronomische Nachrichten*, *337*(4-5), 356–361.

Chen, C.-T. J., Hickox, R. C., Alberts, S., Harrison, C. M., Alexander, D. M., Assef, R., Brodwin, M., Brown, M. J. I., Del Moro, A., Forman, W. R., Gorjian, V., Goulding, A. D., Hainline, K. N., Jones, C., Kochanek, C. S., Murray, S. S., Pope, A., Rovilos, E., & Stern, D. (2015). A Connection between Obscuration and Star Formation in Luminous Quasars. *ApJ*, *802*(1), Article 50, 50. https://doi.org/10.1088/0004-637X/802/1/50

Clark, C. J. R., Verstocken, S., Bianchi, S., Fritz, J., Viaene, S., Smith, M. W. L., Baes, M., Casasola, V., Cassara, L. P., Davies, J. I., De Looze, I., De Vis, P., Evans, R., Galametz, M., Jones, A. P., Lianou, S., Madden, S., Mosenkov, A. V., & Xilouris, M. (2018). DustPedia: Multiwavelength photometry and imagery of 875 nearby galaxies in 42 ultraviolet-microwave bands. *AA*, *609*, Article A37, A37. https://doi.org/10.1051/0004-6361/201731419

Comastri. (2004). Compton-thick agn: The dark side of the x-ray background. In *Supermassive black holes in the distant universe* (pp. 245–272). Springer.

Comastri, Gilli, R., Marconi, A., Risaliti, G., & Salvati, M. (2015). Mass without radiation: Heavily obscured agns, the x-ray background, and the black hole mass density. *Astronomy & Astrophysics*, *574*, L10.

Dadina, M. (2008). Seyfert galaxies in the local universe (z 0.1): The average x-ray spectrum as seen by bepposax. *Astronomy & Astrophysics*, *485*(2), 417–424.

Dale, D. A., Helou, G., Magdis, G. E., Armus, L., Díaz-Santos, T., & Shi, Y. (2014). A Two-parameter Model for the Infrared/Submillimeter/Radio Spectral Energy Distributions of Galaxies and Active Galactic Nuclei. *ApJ*, *784*(1), Article 83, 83. https://doi.org/10.1088/0004-637X/784/1/83

Davies, R. I., Maciejewski, W., Hicks, E. K. S., Tacconi, L. J., Genzel, R., & Engel, H. (2009). Stellar and Molecular Gas Kinematics Of NGC 1097: Inflow Driven by a Nuclear Spiral. *ApJ*, *702*(1), 114–128. https://doi.org/10.1088/0004-637X/702/1/114

De Cicco, M., Marinucci, A., Bianchi, S., Piconcelli, E., Violino, G., Vignali, C., & Nicastro, F. (2015a). Deep X-ray spectroscopy and imaging of the Seyfert 2 galaxy, ESO 138-G001. *MNRAS*, *453*(2), 2155–2162. https://doi.org/10.1093/mnras/stv1702

De Cicco, M., Marinucci, A., Bianchi, S., Piconcelli, E., Violino, G., Vignali, C., & Nicastro, F. (2015b). Deep X-ray spectroscopy and imaging of the Seyfert 2 galaxy, ESO 138-G001. *MNRAS*, *453*(2), 2155–2162. https://doi.org/10.1093/mnras/stv1702

DiPompeo, M. A., Myers, A. D., Hickox, R. C., Geach, J. E., & Hainline, K. N. (2014). The angular clustering of infrared-selected obscured and unobscured quasars. *MNRAS*, *442*(4), 3443–3453. https://doi.org/10.1093/mnras/stu1115

Donoso, E., Yan, L., Tsai, C., Eisenhardt, P., Stern, D., Assef, R. J., Leisawitz, D., Jarrett, T. H., & Stanford, S. A. (2012). Origin of 12 μm Emission across Galaxy

Populations from WISE and SDSS Surveys. *ApJ*, *748*(2), Article 80, 80. https://doi.org/10.1088/0004-637X/748/2/80

Draine, B. T., Aniano, G., Krause, O., Groves, B., Sandstrom, K., Braun, R., Leroy, A., Klaas, U., Linz, H., Rix, H.-W., Schinnerer, E., Schmiedeke, A., & Walter, F. (2014). Andromeda's Dust. *ApJ*, *780*(2), Article 172, 172. https://doi.org/10.1088/0004-637X/780/2/172

Draine, B. T., & Lee, H. M. (1984a). Optical Properties of Interstellar Graphite and Silicate Grains. *ApJ*, *285*, 89. https://doi.org/10.1086/162480

Draine, B. T., & Li, A. (2007). Infrared Emission from Interstellar Dust. IV. The Silicate-Graphite-PAH Model in the Post-Spitzer Era. *ApJ*, *657*(2), 810–837. https://doi.org/10.1086/511055

Draine & Lee, H. M. (1984b). Optical properties of interstellar graphite and silicate grains. *The Astrophysical Journal*, *285*, 89–108.

Dupke, R. A., & Arnaud, K. A. (2001). Central Elemental Abundance Ratios in the Perseus Cluster: Resonant Scattering or SN IA Enrichment? *ApJ*, *548*(1), 141–149. https://doi.org/10.1086/318694

Duras, F., Bongiorno, A., Piconcelli, E., Bianchi, S., Pappalardo, C., Valiante, R., Bischetti, M., Feruglio, C., Martocchia, S., Schneider, R., Vietri, G., Vignali, C., Zappacosta, L., La Franca, F., & Fiore, F. (2017). The WISSH quasars project. II. Giant star nurseries in hyper-luminous quasars. *AA*, *604*, Article A67, A67. https://doi.org/10.1051/0004-6361/201731052

Duras, F., Bongiorno, A., Ricci, F., Piconcelli, E., Shankar, F., Lusso, E., Bianchi, S., Fiore, F., Maiolino, R., Marconi, A., Onori, F., Sani, E., Schneider, R., Vignali, C., & La Franca, F. (2020). Universal bolometric corrections for active galactic nuclei over seven luminosity decades. *AA*, *636*, Article A73, A73. https://doi.org/10.1051/0004-6361/201936817

Elvis, M., Risaliti, G., Nicastro, F., Miller, J. M., Fiore, F., & Puccetti, S. (2004). An Unveiling Event in the Type 2 Active Galactic Nucleus NGC 4388:A Challenge for a Parsec-Scale Absorber. *ApJ Letters*, *615*(1), L25–L28. https://doi.org/10.1086/424380

Esin, A. A., McClintock, J. E., & Narayan, R. (1997). Advection-Dominated Accretion and the Spectral States of Black Hole X-Ray Binaries: Application to Nova Muscae 1991. *ApJ*, *489*(2), 865–889. https://doi.org/10.1086/304829

Esparza-Arredondo, D., Gonzalez-Martín, O., Dultzin, D., Masegosa, J., Ramos-Almeida, C., García-Bernete, I., Fritz, J., & Osorio-Clavijo, N. (2021). The

dust-gas AGN torus as constrained from X-ray and mid-infrared observations. *AA*, *651*, Article A91, A91. https://doi.org/10.1051/0004-6361/202040043

Esparza-Arredondo, D., González-Martín, O., Dultzin, D., Ramos Almeida, C., Fritz, J., Masegosa, J., Pasetto, A., Martínez-Paredes, M., Osorio-Clavijo, N., & Victoria-Ceballos, C. (2019). Physical Parameters of the Torus for the Type 2 Seyfert IC 5063 from Mid-IR and X-Ray Simultaneous Spectral Fitting. *ApJ*, *886*(2), Article 125, 125. https://doi.org/10.3847/1538-4357/ab4ced

Fabian, A. C. (2008). XMM-Newton and broad iron lines. *Astronomische Nachrichten*, *329*(2), 155. https://doi.org/10.1002/asna.200710902

Fabian, A. C. (2012). Observational Evidence of Active Galactic Nuclei Feedback. *ARAA*, *50*, 455–489. https://doi.org/10.1146/annurev-astro-081811-125521

Fath, E. A. (1909). The spectra of some spiral nebulae and globular star clusters. *Lick Observatory Bulletin*, *149*, 71–77. https://doi.org/10.5479/ADS/bib/1909LicOB.5.71F

Feltre, A., Hatziminaoglou, E., Fritz, J., & Franceschini, A. (2012). Smooth and clumpy dust distributions in AGN: a direct comparison of two commonly explored infrared emission models. *MNRAS*, *426*(1), 120–127. https://doi.org/10.1111/j.1365-2966.2012.21695.x

Ferland, G. J., Korista, K. T., Verner, D. A., Ferguson, J. W., Kingdon, J. B., & Verner, E. M. (1998). CLOUDY 90: Numerical Simulation of Plasmas and Their Spectra. *PASP*, *110*(749), 761–778. https://doi.org/10.1086/316190

Ferland, G. J., Porter, R. L., van Hoof, P. A. M., Williams, R. J. R., Abel, N. P., Lykins, M. L., Shaw, G., Henney, W. J., & Stancil, P. C. (2013). The 2013 Release of Cloudy. *RMXAA*, *49*, 137–163. https://doi.org/10.48550/arXiv.1302.4485

Fritz, J., Franceschini, A., & Hatziminaoglou, E. (2006). Revisiting the infrared spectra of active galactic nuclei with a new torus emission model. *MNRAS*, *366*(3), 767–786. https://doi.org/10.1111/j.1365-2966.2006.09866.x

Furui, S., Fukazawa, Y., Odaka, H., Kawaguchi, T., Ohno, M., & Hayashi, K. (2016). X-Ray Spectral Model of Reprocess by Smooth and Clumpy Molecular Tori in Active Galactic Nuclei with the Framework MONACO. *ApJ*, *818*(2), Article 164, 164. https://doi.org/10.3847/0004-637X/818/2/164

Gandhi, P., Horst, H., Smette, A., Hönig, S., Comastri, A., Gilli, R., Vignali, C., & Duschl, W. (2009). Resolving the mid-infrared cores of local Seyferts. *AA*, *502*(2), 457–472. https://doi.org/10.1051/0004-6361/200811368

García-Bernete, I., González-Martín, O., Ramos Almeida, C., Alonso-Herrero, A., Martínez-Paredes, M., Ward, M. J., Roche, P. F., Acosta-Pulido, J. A., López-Rodríguez, E., Rigopoulou, D., & Esparza-Arredondo, D. (2022). Torus and polar dust dependence on active galactic nucleus properties. *AA*, *667*, Article A140, A140. https://doi.org/10.1051/0004-6361/202244230

García-Bernete, I., Ramos Almeida, C., Acosta-Pulido, J. A., Alonso-Herrero, A., González-Martín, O., Hernán-Caballero, A., Pereira-Santaella, M., Levenson, N. A., Packham, C., Perlman, E. S., Ichikawa, K., Esquej, P., & Díaz-Santos, T. (2016). The nuclear and extended mid-infrared emission of Seyfert galaxies. *MNRAS*, *463*(4), 3531–3555. https://doi.org/10.1093/mnras/stw2125

García-Burillo, S., Alonso-Herrero, A., Ramos Almeida, C., González-Martín, O., Combes, F., Usero, A., Hönig, S., Querejeta, M., Hicks, E. K. S., Hunt, L. K., Rosario, D., Davies, R., Boorman, P. G., Bunker, A. J., Burtscher, L., Colina, L., Díaz-Santos, T., Gandhi, P., García-Bernete, I., García-Lorenzo, B., Ichikawa, K., Imanishi, M., Izumi, T., Labiano, A., Levenson, N. A., López-Rodríguez, E., Packham, C., Pereira-Santaella, M., Ricci, C., Rigopoulou, D., Rouan, D., Shimizu, T., Stalevski, M., Wada, K., & Williamson, D. (2021a). The Galaxy Activity, Torus, and Outflow Survey (GATOS). I. ALMA images of dusty molecular tori in Seyfert galaxies. *AA*, *652*, Article A98, A98. https://doi.org/10.1051/0004-6361/202141075

García-Burillo, S., Alonso-Herrero, A., Ramos Almeida, C., González-Martín, O., Combes, F., Usero, A., Hönig, S., Querejeta, M., Hicks, E. K. S., Hunt, L. K., Rosario, D., Davies, R., Boorman, P. G., Bunker, A. J., Burtscher, L., Colina, L., Díaz-Santos, T., Gandhi, P., García-Bernete, I., García-Lorenzo, B., Ichikawa, K., Imanishi, M., Izumi, T., Labiano, A., Levenson, N. A., López-Rodríguez, E., Packham, C., Pereira-Santaella, M., Ricci, C., Rigopoulou, D., Rouan, D., Shimizu, T., Stalevski, M., Wada, K., & Williamson, D. (2021b). The Galaxy Activity, Torus, and Outflow Survey (GATOS). I. ALMA images of dusty molecular tori in Seyfert galaxies. *AA*, *652*, Article A98, A98. https://doi.org/10.1051/0004-6361/202141075

García-Burillo, S., Combes, F., Ramos Almeida, C., Usero, A., Krips, M., Alonso-Herrero, A., Aalto, S., Casasola, V., Hunt, L. K., Martín, S., Viti, S., Colina, L., Costagliola, F., Eckart, A., Fuente, A., Henkel, C., Márquez, I., Neri, R., Schinnerer, E., Tacconi, L. J., & van der Werf, P. P. (2016). ALMA Resolves

the Torus of NGC 1068: Continuum and Molecular Line Emission. *ApJ Letters*, *823*(1), Article L12, L12. https://doi.org/10.3847/2041-8205/823/1/L12

Gaskell, C. M., Goosmann, R. W., Antonucci, R. R. J., & Whysong, D. H. (2004). The Nuclear Reddening Curve for Active Galactic Nuclei and the Shape of the Infrared to X-Ray Spectral Energy Distribution. *ApJ*, *616*(1), 147–156. https://doi.org/10.1086/423885

Gaspar, G., Díaz, R. J., Mast, D., D'Ambra, A., Agüero, M. P., & Günthardt, G. (2019). A Near-infrared View of Nearby Galaxies: The Case of NGC 6300. *AJ*, *157*(2), Article 44, 44. https://doi.org/10.3847/1538-3881/aaf4b9

Gaspari, M., Eckert, D., Ettori, S., Tozzi, P., Bassini, L., Rasia, E., Brighenti, F., Sun, M., Borgani, S., Johnson, S. D., Tremblay, G. R., Stone, J. M., Temi, P., Yang, H. .-. K., Tombesi, F., & Cappi, M. (2019). The X-Ray Halo Scaling Relations of Supermassive Black Holes. *ApJ*, *884*(2), Article 169, 169. https://doi.org/10.3847/1538-4357/ab3c5d

Gaspari, M., Ruszkowski, M., & Oh, S. P. (2013). Chaotic cold accretion on to black holes. *MNRAS*, *432*(4), 3401–3422. https://doi.org/10.1093/mnras/stt692

Gaspari, M., Temi, P., & Brighenti, F. (2017). Raining on black holes and massive galaxies: the top-down multiphase condensation model. *MNRAS*, *466*(1), 677–704. https://doi.org/10.1093/mnras/stw3108

Gaspari, M., Tombesi, F., & Cappi, M. (2020). Linking macro-, meso- and microscales in multiphase AGN feeding and feedback. *Nature Astronomy*, *4*, 10–13. https://doi.org/10.1038/s41550-019-0970-1

Georgantopoulos, I., & Akylas, A. (2019). NuSTAR observations of heavily obscured Swift/BAT AGNs: Constraints on the Compton-thick AGNs fraction. *AA*, *621*, Article A28, A28. https://doi.org/10.1051/0004-6361/201833038

Giacconi, R., Gursky, H., Paolini, F. R., & Rossi, B. B. (1962). Evidence for x rays from sources outside the solar system. *Physical Review Letters*, *9*(11), 439.

Gilli et al. (2007). The synthesis of the cosmic x-ray background in the chandra and xmm-newton era. *Astronomy & Astrophysics*, *463*(1), 79–96.

Gilli, R., Norman, C., Calura, F., Vito, F., Decarli, R., Marchesi, S., Iwasawa, K., Comastri, A., Lanzuisi, G., Pozzi, F., D'Amato, Q., Vignali, C., Brusa, M., Mignoli, M., & Cox, P. (2022). Supermassive Black Holes at High Redshift are Expected to be Obscured by their Massive Host Galaxies' Inter Stellar Medium. *arXiv e-prints*, Article arXiv:2206.03508, arXiv:2206.03508.

Glikman, E., Simmons, B., Mailly, M., Schawinski, K., Urry, C. M., & Lacy, M. (2015). Major Mergers Host the Most-luminous Red Quasars at z ~2: A Hubble Space Telescope WFC3/IR Study. *ApJ*, *806*(2), Article 218, 218. https://doi.org/10.1088/0004-637X/806/2/218

Goulding, A. D., & Alexander, D. M. (2009). Towards a complete census of AGN in nearby Galaxies: a large population of optically unidentified AGN. *MNRAS*, *398*(3), 1165–1193. https://doi.org/10.1111/j.1365-2966.2009.15194.x

Goulding, A. D., Alexander, D. M., Bauer, F. E., Forman, W. R., Hickox, R. C., Jones, C., Mullaney, J. R., & Trichas, M. (2012). Deep Silicate Absorption Features in Compton-thick Active Galactic Nuclei Predominantly Arise due to Dust in the Host Galaxy. *ApJ*, *755*(1), Article 5, 5. https://doi.org/10.1088/0004-637X/755/1/5

Goulding, A. D., Greene, J. E., Bezanson, R., Greco, J., Johnson, S., Leauthaud, A., Matsuoka, Y., Medezinski, E., & Price-Whelan, A. M. (2018). Galaxy interactions trigger rapid black hole growth: An unprecedented view from the Hyper Suprime-Cam survey. *PASJ*, *70*, Article S37, S37. https://doi.org/10.1093/pasj/psx135

Guainazzi, M. (2002). The formerly X-ray reflection-dominated Seyfert 2 galaxy NGC 6300. *MNRAS*, *329*(1), L13–L17. https://doi.org/10.1046/j.1365-8711.2002.05132.x

Harrison, F., Aird, J., Civano, F., Lansbury, G., Mullaney, J., Ballantyne, D., Alexander, D., Stern, D., Ajello, M., Barret, D., et al. (2016). The nustar extragalactic surveys: The number counts of active galactic nuclei and the resolved fraction of the cosmic x-ray background. *The Astrophysical Journal*, *831*(2), 185.

Harrison, F. A., Boggs, S., Christensen, F., Craig, W., Hailey, C., Stern, D., Zhang, W., Angelini, L., An, H., Bhalereo, V., Brejnholt, N., Cominsky, L., Cook, W. R., Doll, M., Giommi, P., Grefenstette, B., Hornstrup, A., Kaspi, V. M., Kim, Y., Kitaguchi, T., Koglin, J., Liebe, C. C., Madejski, G., Kruse Madsen, K., Mao, P., Meier, D., Miyasaka, H., Mori, K., Perri, M., Pivovaroff, M., Puccetti, S., Rana, V., & Zoglauer, A. (2010). The Nuclear Spectroscopic Telescope Array (NuSTAR). *arXiv e-prints*, Article arXiv:1008.1362, arXiv:1008.1362. https://doi.org/10.48550/arXiv.1008.1362

Harrison, F. A., Craig, W. W., Christensen, F. E., Hailey, C. J., Zhang, W. W., Boggs, S. E., Stern, D., Cook, W. R., Forster, K., Giommi, P., Grefenstette, B. W., Kim, Y., Kitaguchi, T., Koglin, J. E., Madsen, K. K., Mao, P. H., Miyasaka,

H., Mori, K., Perri, M., Pivovaroff, M. J., Puccetti, S., Rana, V. R., Westergaard, N. J., Willis, J., Zoglauer, A., An, H., Bachetti, M., Barrière, N. M., Bellm, E. C., Bhalerao, V., Brejnholt, N. F., Fuerst, F., Liebe, C. C., Markwardt, C. B., Nynka, M., Vogel, J. K., Walton, D. J., Wik, D. R., Alexander, D. M., Cominsky, L. R., Hornschemeier, A. E., Hornstrup, A., Kaspi, V. M., Madejski, G. M., Matt, G., Molendi, S., Smith, D. M., Tomsick, J. A., Ajello, M., Ballantyne, D. R., Baloković, M., Barret, D., Bauer, F. E., Blandford, R. D., Brandt, W. N., Brenneman, L. W., Chiang, J., Chakrabarty, D., Chenevez, J., Comastri, A., Dufour, F., Elvis, M., Fabian, A. C., Farrah, D., Fryer, C. L., Gotthelf, E. V., Grindlay, J. E., Helfand, D. J., Krivonos, R., Meier, D. L., Miller, J. M., Natalucci, L., Ogle, P., Ofek, E. O., Ptak, A., Reynolds, S. P., Rigby, J. R., Tagliaferri, G., Thorsett, S. E., Treister, E., & Urry, C. M. (2013). The Nuclear Spectroscopic Telescope Array (NuSTAR) High-energy X-Ray Mission. *ApJ*, *770*(2), Article 103, 103. https://doi.org/10.1088/0004-637X/770/2/103

Hatziminaoglou, Hernán-Caballero, A., Feltre, A., & Ferrer, N. P. (2015). A complete census of silicate features in the mid-infrared spectra of active galaxies. *The Astrophysical Journal*, *803*(2), 110.

Hickox & Alexander. (2018). Obscured active galactic nuclei. *Annual Review of Astronomy and Astrophysics*, *56*, 625–671.

Hickox, R. C., & Markevitch, M. (2006). Absolute Measurement of the Unresolved Cosmic X-Ray Background in the 0.5-8 keV Band with Chandra. *ApJ*, *645*(1), 95–114. https://doi.org/10.1086/504070

Hickox, R. C., Myers, A. D., Brodwin, M., Alexander, D. M., Forman, W. R., Jones, C., Murray, S. S., Brown, M. J. I., Cool, R. J., Kochanek, C. S., Dey, A., Jannuzi, B. T., Eisenstein, D., Assef, R. J., Eisenhardt, P. R., Gorjian, V., Stern, D., Le Floc'h, E., Caldwell, N., Goulding, A. D., & Mullaney, J. R. (2011). Clustering of Obscured and Unobscured Quasars in the Boötes Field: Placing Rapidly Growing Black Holes in the Cosmic Web. *ApJ*, *731*(2), Article 117, 117. https://doi.org/10.1088/0004-637X/731/2/117

Hitomi Collaboration, Aharonian, F., Akamatsu, H., Akimoto, F., Allen, S. W., Anabuki, N., Angelini, L., Arnaud, K., Audard, M., Awaki, H., Axelsson, M., Bamba, A., Bautz, M., Blandford, R., Brenneman, L., Brown, G. V., Bulbul, E., Cackett, E., Chernyakova, M., Chiao, M., Coppi, P., Costantini, E., de Plaa, J., den Herder, J.-W., Done, C., Dotani, T., Ebisawa, K., Eckart, M., Enoto, T., Ezoe, Y., Fabian, A. C., Ferrigno, C., Foster, A., Fujimoto, R., Fukazawa, Y.,

Furuzawa, A., Galeazzi, M., Gallo, L., Gandhi, P., Giustini, M., Goldwurm, A., Gu, L., Guainazzi, M., Haba, Y., Hagino, K., Hamaguchi, K., Harrus, I., Hatsukade, I., Hayashi, K., Hayashi, T., Hayashida, K., Hiraga, J., Hornschemeier, A., Hoshino, A., Hughes, J., Iizuka, R., Inoue, H., Inoue, Y., Ishibashi, K., Ishida, M., Ishikawa, K., Ishisaki, Y., Itoh, M., Iyomoto, N., Kaastra, J., Kallman, T., Kamae, T., Kara, E., Kataoka, J., Katsuda, S., Katsuta, J., Kawaharada, M., Kawai, N., Kelley, R., Khangulyan, D., Kilbourne, C., King, A., Kitaguchi, T., Kitamoto, S., Kitayama, T., Kohmura, T., Kokubun, M., Koyama, S., Koyama, K., Kretschmar, P., Krimm, H., Kubota, A., Kunieda, H., Laurent, P., Lebrun, F., Lee, S.-H., Leutenegger, M., Limousin, O., Loewenstein, M., Long, K. S., Lumb, D., Madejski, G., Maeda, Y., Maier, D., Makishima, K., Markevitch, M., Matsumoto, H., Matsushita, K., McCammon, D., McNamara, B., Mehdipour, M., Miller, E., Miller, J., Mineshige, S., Mitsuda, K., Mitsuishi, I., Miyazawa, T., Mizuno, T., Mori, H., Mori, K., Moseley, H., Mukai, K., Murakami, H., Murakami, T., Mushotzky, R., Nagino, R., Nakagawa, T., Nakajima, H., Nakamori, T., Nakano, T., Nakashima, S., Nakazawa, K., Nobukawa, M., Noda, H., Nomachi, M., O'Dell, S., Odaka, H., Ohashi, T., Ohno, M., Okajima, T., Ota, N., Ozaki, M., Paerels, F., Paltani, S., Parmar, A., Petre, R., Pinto, C., Pohl, M., Porter, F. S., Pottschmidt, K., Ramsey, B., Reynolds, C., Russell, H., Safi-Harb, S., Saito, S., Sakai, K., Sameshima, H., Sato, G., Sato, K., Sato, R., Sawada, M., Schartel, N., Serlemitsos, P., Seta, H., Shidatsu, M., Simionescu, A., Smith, R., Soong, Y., Stawarz, L., Sugawara, Y., Sugita, S., Szymkowiak, A., Tajima, H., Takahashi, H., Takahashi, T., Takeda, S., Takei, Y., Tamagawa, T., Tamura, K., Tamura, T., Tanaka, T., Tanaka, Y., Tanaka, Y., Tashiro, M., Tawara, Y., Terada, Y., Terashima, Y., Tombesi, F., Tomida, H., Tsuboi, Y., Tsujimoto, M., Tsunemi, H., Tsuru, T., Uchida, H., Uchiyama, H., Uchiyama, Y., Ueda, S., Ueda, Y., Ueno, S., Uno, S., Urry, M., Ursino, E., de Vries, C., Watanabe, S., Werner, N., Wik, D., Wilkins, D., Williams, B., Yamada, S., Yamaguchi, H., Yamaoka, K., Yamasaki, N. Y., Yamauchi, M., Yamauchi, S., Yaqoob, T., Yatsu, Y., Yonetoku, D., Yoshida, A., Yuasa, T., Zhuravleva, I., & Zoghbi, A. (2016). The quiescent intracluster medium in the core of the Perseus cluster. *NAT*, *535*(7610), 117–121. https://doi.org/10.1038/nature18627

Ho, L. C. (2008). Nuclear activity in nearby galaxies. *ARAA*, *46*, 475–539. https://doi.org/10.1146/annurev.astro.45.051806.110546

Ho, L. C., Filippenko, A. V., & Sargent, W. L. W. (1997). A Search for "Dwarf" Seyfert Nuclei. III. Spectroscopic Parameters and Properties of the Host Galaxies. *ApJs*, *112*(2), 315–390. https://doi.org/10.1086/313041

Hopkins, P. F., Hernquist, L., Cox, T. J., & Kereš, D. (2008). A Cosmological Framework for the Co-Evolution of Quasars, Supermassive Black Holes, and Elliptical Galaxies. I. Galaxy Mergers and Quasar Activity. *ApJs*, *175*(2), 356–389. https://doi.org/10.1086/524362

Hopkins, P. F., Torrey, P., Faucher-Giguère, C.-A., Quataert, E., & Murray, N. (2016). Stellar and quasar feedback in concert: effects on AGN accretion, obscuration, and outflows. *MNRAS*, *458*(1), 816–831. https://doi.org/10.1093/mnras/stw289

Hubble, E. P. (1926). Extragalactic nebulae. *ApJ*, *64*, 321–369. https://doi.org/10.1086/143018

Humason, M. L. (1932). The Emission Spectrum of the Extra-Galactic Nebula N. G. C. 1275. *PASP*, *44*(260), 267. https://doi.org/10.1086/124242

Ichikawa, K., Packham, C., Ramos Almeida, C., Asensio Ramos, A., Alonso-Herrero, A., González-Martín, O., Lopez-Rodriguez, E., Ueda, Y., Díaz-Santos, T., Elitzur, M., Hönig, S. F., Imanishi, M., Levenson, N. A., Mason, R. E., Perlman, E. S., & Alsip, C. D. (2015). The Differences in the Torus Geometry between Hidden and Non-hidden Broad Line Active Galactic Nuclei. *ApJ*, *803*(2), Article 57, 57. https://doi.org/10.1088/0004-637X/803/2/57

Inoue, A. K. (2011). Rest-frame ultraviolet-to-optical spectral characteristics of extremely metal-poor and metal-free galaxies. *MNRAS*, *415*(3), 2920–2931. https://doi.org/10.1111/j.1365-2966.2011.18906.x

Iwasawa, K., Sanders, D. B., Teng, S. H., U, V., Armus, L., Evans, A. S., Howell, J. H., Komossa, S., Mazzarella, J. M., Petric, A. O., Surace, J. A., Vavilkin, T., Veilleux, S., & Trentham, N. (2011). C-GOALS: Chandra observations of a complete sample of luminous infrared galaxies from the IRAS Revised Bright Galaxy Survey. *AA*, *529*, Article A106, A106. https://doi.org/10.1051/0004-6361/201015264

Jana, A., Chatterjee, A., Kumari, N., Nandi, P., Naik, S., & Patra, D. (2020). Probing the nuclear and circumnuclear properties of NGC 6300 using X-ray observations. *MNRAS*, *499*(4), 5396–5409. https://doi.org/10.1093/mnras/staa2552

Jansen, F., Lumb, D., Altieri, B., Clavel, J., Ehle, M., Erd, C., Gabriel, C., Guainazzi, M., Gondoin, P., Much, R., et al. (2001). Xmm-newton observatory-i. the space-craft and operations. *Astronomy & Astrophysics*, *365*(1), L1–L6.

Just, D. W., Brandt, W. N., Shemmer, O., Steffen, A. T., Schneider, D. P., Chartas, G., & Garmire, G. P. (2007). The X-Ray Properties of the Most Luminous Quasars from the Sloan Digital Sky Survey. *ApJ*, *665*(2), 1004–1022. https://doi.org/10.1086/519990

Kaastra, J. (1992). An X-Ray Spectral Code for Optically Thin Plasmas. *Internal SRON-Leiden Report*.

Kalberla, P. M. W., Burton, W. B., Hartmann, D., Arnal, E. M., Bajaja, E., Morras, R., & Pöppel, W. G. L. (2005). The Leiden/Argentine/Bonn (LAB) Survey of Galactic HI. Final data release of the combined LDS and IAR surveys with improved stray-radiation corrections. *AA*, *440*(2), 775–782. https://doi.org/10.1051/0004-6361:20041864

Kammoun, E. S., Miller, J. M., Koss, M., Oh, K., Zoghbi, A., Mushotzky, R. F., Barret, D., Behar, E., Brandt, W. N., Brenneman, L. W., Kaastra, J. S., Lohfink, A. M., Proga, D., & Stern, D. (2020). A Hard Look at Local, Optically Selected, Obscured Seyfert Galaxies. *ApJ*, *901*(2), Article 161, 161. https://doi.org/10.3847/1538-4357/abb29f

Kara, E., Alston, W., Fabian, A., Cackett, E., Uttley, P., Reynolds, C., & Zoghbi, A. (2016). A global look at x-ray time lags in seyfert galaxies. *Monthly Notices of the Royal Astronomical Society*, *462*(1), 511–531.

Kawaguchi, T., & Mori, M. (2010). Orientation Effects on the Inner Region of Dusty Torus of Active Galactic Nuclei. *ApJ Letters*, *724*(2), L183–L187. https://doi.org/10.1088/2041-8205/724/2/L183

Kawaguchi, T., & Mori, M. (2011). Near-infrared Reverberation by Dusty Clumpy Tori in Active Galactic Nuclei. *ApJ*, *737*(2), Article 105, 105. https://doi.org/10.1088/0004-637X/737/2/105

Kellermann, K., Sramek, R., Schmidt, M., Shaffer, D., & Green, R. (1989). Vla observations of objects in the palomar bright quasar survey. *The Astronomical Journal*, *98*, 1195–1207.

Kennicutt, J., Robert C. (1998). The Global Schmidt Law in Star-forming Galaxies. *ApJ*, *498*(2), 541–552. https://doi.org/10.1086/305588

Khorunzhev, G. A., Sazonov, S. Y., Burenin, R. A., & Tkachenko, A. Y. (2012). Masses and accretion rates of supermassive black holes in active galactic nuclei from

the INTEGRAL survey. *Astronomy Letters*, *38*(8), 475–491. https://doi.org/10.1134/S1063773712080026

Koss, M., Trakhtenbrot, B., Ricci, C., Lamperti, I., Oh, K., Berney, S., Schawinski, K., Baloković, M., Baronchelli, L., Crenshaw, D. M., Fischer, T., Gehrels, N., Harrison, F., Hashimoto, Y., Hogg, D., Ichikawa, K., Masetti, N., Mushotzky, R., Sartori, L., Stern, D., Treister, E., Ueda, Y., Veilleux, S., & Winter, L. (2017). BAT AGN Spectroscopic Survey. I. Spectral Measurements, Derived Quantities, and AGN Demographics. *ApJ*, *850*(1), Article 74, 74. https://doi.org/10.3847/1538-4357/aa8ec9

Koss, M. J., Assef, R., Baloković, M., Stern, D., Gandhi, P., Lamperti, I., Alexander, D., Ballantyne, D., Bauer, F., Berney, S., et al. (2016). A new population of compton-thick agns identified using the spectral curvature above 10 kev. *The Astrophysical Journal*, *825*(2), 85.

Krolik, J. H., & Begelman, M. C. (1988). Molecular tori in seyfert galaxies-feeding the monster and hiding it. *The Astrophysical Journal*, *329*, 702–711.

Laha, S., Markowitz, A. G., Krumpe, M., Nikutta, R., Rothschild, R., & Saha, T. (2020). The Variable and Non-variable X-Ray Absorbers in Compton-thin Type II Active Galactic Nuclei. *ApJ*, *897*(1), Article 66, 66. https://doi.org/10.3847/1538-4357/ab92ab

Leighly, K. M., Halpern, J. P., Awaki, H., Cappi, M., Ueno, S., & Siebert, J. (1999). An RXTE Observation of NGC 6300: A New Bright Compton Reflection-dominated Seyfert 2 Galaxy. *ApJ*, *522*(1), 209–213. https://doi.org/10.1086/307649

Leitherer, C., Calzetti, D., & Martins, L. P. (2002). Ultraviolet Spectra of Star-forming Galaxies with Time-dependent Dust Obscuration. *ApJ*, *574*(1), 114–125. https://doi.org/10.1086/340902

Liedahl, D. A., Osterheld, A. L., & Goldstein, W. H. (1995). New Calculations of Fe L-Shell X-Ray Spectra in High-Temperature Plasmas. *ApJ Letters*, *438*, L115. https://doi.org/10.1086/187729

Liu, Taam, R. E., Qiao, E., & Yuan, W. (2017). Centrally concentrated x-ray radiation from an extended accreting corona in active galactic nuclei. *The Astrophysical Journal*, *847*(2), 96.

Liu, Y., & Li, X. (2014). An X-Ray Spectral Model for Clumpy Tori in Active Galactic Nuclei. *ApJ*, *787*(1), Article 52, 52. https://doi.org/10.1088/0004-637X/787/1/52

López, G. (2016). The structure of the dusty cores of active galactic nuclei.

Lusso, E., Comastri, A., Vignali, C., Zamorani, G., Brusa, M., Gilli, R., Iwasawa, K., Salvato, M., Civano, F., Elvis, M., Merloni, A., Bongiorno, A., Trump, J. R., Koekemoer, A. M., Schinnerer, E., Le Floc'h, E., Cappelluti, N., Jahnke, K., Sargent, M., Silverman, J., Mainieri, V., Fiore, F., Bolzonella, M., Le Fèvre, O., Garilli, B., Iovino, A., Kneib, J. P., Lamareille, F., Lilly, S., Mignoli, M., Scodeggio, M., & Vergani, D. (2010). The X-ray to optical-UV luminosity ratio of X-ray selected type 1 AGN in XMM-COSMOS. *AA*, *512*, Article A34, A34. https://doi.org/10.1051/0004-6361/200913298

Lusso, E., & Risaliti, G. (2017). Quasars as standard candles. I. The physical relation between disc and coronal emission. *AA*, *602*, Article A79, A79. https://doi.org/10.1051/0004-6361/201630079

Maccagni, F. M., Serra, P., Gaspari, M., Kleiner, D., Morokuma-Matsui, K., Oosterloo, T. A., Onodera, M., Kamphuis, P., Loi, F., Thorat, K., Ramatsoku, M., Smirnov, O., & White, S. V. (2021). AGN feeding and feedback in Fornax A. Kinematical analysis of the multi-phase ISM. *AA*, *656*, Article A45, A45. https://doi.org/10.1051/0004-6361/202141143

Maraston, C. (2005). Evolutionary population synthesis: models, analysis of the ingredients and application to high-z galaxies. *MNRAS*, *362*(3), 799–825. https://doi.org/10.1111/j.1365-2966.2005.09270.x

Marchesi et al. (2018). Compton-thick agns in the nustar era. *The Astrophysical Journal*, *854*(1), 49.

Marchesi, S., Ajello, M., Zhao, X., Comastri, A., La Parola, V., & Segreto, A. (2019). Compton-thick AGNs in the NuSTAR Era. V. Joint NuSTAR and XMM-Newton Spectral Analysis of Three "Soft-gamma" Candidate CT-AGNs in the Swift/BAT 100-month Catalog. *ApJ*, *882*(2), Article 162, 162. https://doi.org/10.3847/1538-4357/ab340a

Marchesi, S., Ajello, M., Zhao, X., Marcotulli, L., Baloković, M., Brightman, M., Comastri, A., Cusumano, G., Lanzuisi, G., La Parola, V., Segreto, A., & Vignali, C. (2019). Compton-thick AGNs in the NuSTAR Era. III. A Systematic Study of the Torus Covering Factor. *ApJ*, *872*(1), Article 8, 8. https://doi.org/10.3847/1538-4357/aafbeb

Marchesi, S., Lanzuisi, G., Civano, F., Iwasawa, K., Suh, H., Comastri, A., Zamorani, G., Allevato, V., Griffiths, R., Miyaji, T., Ranalli, P., Salvato, M., Schawinski, K., Silverman, J., Treister, E., Urry, C. M., & Vignali, C. (2016). The Chan-

dra COSMOS-Legacy Survey: Source X-Ray Spectral Properties. *ApJ*, *830*(2), Article 100, 100. https://doi.org/10.3847/0004-637X/830/2/100

Marchesi, S., Zhao, X., Torres-Albà, N., Ajello, M., Gaspari, M., Pizzetti, A., Buchner, J., Bertola, E., Comastri, A., Feltre, A., Gilli, R., Lanzuisi, G., Matzeu, G., Pozzi, F., Salvestrini, F., Sengupta, D., Silver, R., Tombesi, F., Traina, A., Vignali, C., & Zappacosta, L. (2022). Compton-thick AGN in the NuSTAR Era. VIII. A joint NuSTAR-XMM-Newton Monitoring of the Changing-look Compton-thick AGN NGC 1358. *ApJ*, *935*(2), Article 114, 114. https://doi.org/10.3847/1538-4357/ac80be

Markowitz, A. G., Krumpe, M., & Nikutta, R. (2014). First X-ray-based statistical tests for clumpy-torus models: eclipse events from 230 years of monitoring of Seyfert AGN. *MNRAS*, *439*(2), 1403–1458. https://doi.org/10.1093/mnras/stt2492

Matsumoto, C., Nava, A., Maddox, L. A., Leighly, K. M., Grupe, D., Awaki, H., & Ueno, S. (2004). An XMM-Newton Observation of the Seyfert 2 Galaxy NGC 6300. I. The Nucleus. *ApJ*, *617*(2), 930–938. https://doi.org/10.1086/425566

Mayall, N. U. (1934). The Spectrum of the Spiral Nebula NGC 4151. *PASP*, *46*(271), 134. https://doi.org/10.1086/124429

McKinley, B., Tingay, S. J., Gaspari, M., Kraft, R. P., Matherne, C., Offringa, A. R., McDonald, M., Calzadilla, M. S., Veilleux, S., Shabala, S. S., Gwyn, S. D. J., Bland-Hawthorn, J., Crnojević, D., Gaensler, B. M., & Johnston-Hollitt, M. (2022). Multi-scale feedback and feeding in the closest radio galaxy Centaurus A. *Nature Astronomy*, *6*, 109–120. https://doi.org/10.1038/s41550-021-01553-3

Mewe, R., Gronenschild, E., & Van Den Oord, G. (1985). Calculated x-radiation from optically thin plasmas. v. *Astronomy and Astrophysics supplement series*, *62*, 197–254.

Mullaney, J. R., Alexander, D. M., Goulding, A. D., & Hickox, R. C. (2011). Defining the intrinsic AGN infrared spectral energy distribution and measuring its contribution to the infrared output of composite galaxies. *MNRAS*, *414*(2), 1082–1110. https://doi.org/10.1111/j.1365-2966.2011.18448.x

Murphy & Yaqoob. (2009). An x-ray spectral model for compton-thick toroidal reprocessors. *Monthly Notices of the Royal Astronomical Society*, *397*(3), 1549–1562.

Nagao, T., Maiolino, R., Marconi, A., & Matsuhara, H. (2011). Metallicity diagnostics with infrared fine-structure lines. *AA*, *526*, Article A149, A149. https://doi.org/10.1051/0004-6361/201015471

Narayan, R., & Yi, I. (1994). Advection-dominated accretion: A self-similar solution. *arXiv preprint astro-ph/9403052*.

Nenkova, M., et al. (2002). Dust emission from active galactic nuclei. *The Astrophysical Journal Letters*, *570*(1), L9.

Nenkova, M., Sirocky, M. M., Ivezić, Ž., & Elitzur, M. (2008). AGN Dusty Tori. I. Handling of Clumpy Media. *ApJ*, *685*(1), 147–159. https://doi.org/10.1086/590482

Nenkova, M., Sirocky, M. M., Nikutta, R., Ivezić, Ž., & Elitzur, M. (2008). AGN Dusty Tori. II. Observational Implications of Clumpiness. *ApJ*, *685*(1), 160–180. https://doi.org/10.1086/590483

Netzer, H. (1987). Quasar discs. II - A composite model for the broad-line region. *MNRAS*, *225*, 55–72. https://doi.org/10.1093/mnras/225.1.55

Netzer, H. (2015). Revisiting the unified model of active galactic nuclei. *Annual Review of Astronomy and Astrophysics*, *53*, 365–408.

Oda, S., Tanimoto, A., Ueda, Y., Imanishi, M., Terashima, Y., & Ricci, C. (2017). Shedding Light on the Compton-thick Active Galactic Nucleus in the Ultraluminous Infrared Galaxy UGC 5101 with Broadband X-Ray Spectroscopy. *ApJ*, *835*(2), Article 179, 179. https://doi.org/10.3847/1538-4357/835/2/179

Odaka, H., Tanaka, Y., Watanabe, S., Khangulyan, D., Takahashi, T., & Aharonian, F. (2011, August). Calculation framework of X-ray radiation based on Monte Carlo simulations. In J.-U. Ness & M. Ehle (Eds.), *The x-ray universe 2011* (p. 115).

Odaka, H., Yoneda, H., Takahashi, T., & Fabian, A. (2016). Sensitivity of the Fe Kα Compton shoulder to the geometry and variability of the X-ray illumination of cosmic objects. *MNRAS*, *462*(3), 2366–2381. https://doi.org/10.1093/mnras/stw1764

Oh, K., Koss, M., Markwardt, C. B., Schawinski, K., Baumgartner, W. H., Barthelmy, S. D., Cenko, S. B., Gehrels, N., Mushotzky, R., Petulante, A., Ricci, C., Lien, A., & Trakhtenbrot, B. (2018). The 105-Month Swift-BAT All-sky Hard X-Ray Survey. *ApJs*, *235*(1), Article 4, 4. https://doi.org/10.3847/1538-4365/aaa7fd

Pacifici, C., Charlot, S., Blaizot, J., & Brinchmann, J. (2012). Relative merits of different types of rest-frame optical observations to constrain galaxy physical parameters. *MNRAS*, *421*(3), 2002–2024. https://doi.org/10.1111/j.1365-2966.2012.20431.x

Padovani, P. (2011). The microjansky and nanojansky radio sky: Source population and multiwavelength properties. *Monthly Notices of the Royal Astronomical Society*, *411*(3), 1547–1561.

Page, K. L., Starling, R. L. C., Fitzpatrick, G., Pandey, S. B., Osborne, J. P., Schady, P., McBreen, S., Campana, S., Ukwatta, T. N., Pagani, C., Beardmore, A. P., & Evans, P. A. (2011). GRB 090618: detection of thermal X-ray emission from a bright gamma-ray burst. *MNRAS*, *416*(3), 2078–2089. https://doi.org/10.1111/j.1365-2966.2011.19183.x

Penzias, A. A., & Wilson, R. W. (1965). A Measurement of Excess Antenna Temperature at 4080 Mc/s. *ApJ*, *142*, 419–421. https://doi.org/10.1086/148307

Piconcelli, E., Bianchi, S., Vignali, C., Jiménez-Bailón, E., & Fiore, F. (2011a). X-ray spectroscopy of the compton-thick seyfert 2 eso 138- g1. *Astronomy & Astrophysics*, *534*, A126.

Piconcelli, E., Bianchi, S., Vignali, C., Jiménez-Bailón, E., & Fiore, F. (2011b). X-ray spectroscopy of the Compton-thick Seyfert 2 ESO 138 - G1. *AA*, *534*, Article A126, A126. https://doi.org/10.1051/0004-6361/201117462

Pizzetti, A., Torres-Albà, N., Marchesi, S., Ajello, M., Silver, R., & Zhao, X. (2022). A Multiepoch X-Ray Study of the Nearby Seyfert 2 Galaxy NGC 7479: Linking Column Density Variability to the Torus Geometry. *ApJ*, *936*(2), Article 149, 149. https://doi.org/10.3847/1538-4357/ac86c6

Polletta, M., Courvoisier, T. J. .-., Hooper, E. J., & Wilkes, B. J. (2000). The far-infrared emission of radio loud and radio quiet quasars. *AA*, *362*, 75–96. https://doi.org/10.48550/arXiv.astro-ph/0006315

Prevot, M. L., Lequeux, J., Maurice, E., Prevot, L., & Rocca-Volmerange, B. (1984). The typical interstellar extinction in the Small Magellanic Cloud. *AA*, *132*, 389–392.

Ramos Almeida, C., Alonso-Herrero, A., Esquej, P., González-Martín, O., Riffel, R. A., García-Bernete, I., Rodríguez Espinosa, J. M., Packham, C., Levenson, N. A., Roche, P., Díaz-Santos, T., Aretxaga, I., & Álvarez, C. (2014). A mid-infrared view of the inner parsecs of the Seyfert galaxy Mrk 1066 using CanariCam/GTC. *MNRAS*, *445*(2), 1130–1143. https://doi.org/10.1093/mnras/stu1756

Ramos Almeida, C., & Ricci, C. (2017). Nuclear obscuration in active galactic nuclei. *Nature Astronomy*, *1*, 679–689. https://doi.org/10.1038/s41550-017-0232-z

Ramos Almeida, C., Sánchez-Portal, M., Pérez García, A. M., Acosta-Pulido, J., Castillo, M., Asensio Ramos, A., González-Serrano, J. I., Alonso-Herrero, A.,

Rodríguez Espinosa, J., Hatziminaoglou, E., et al. (2011). Resolving the nuclear dust distribution of the seyfert 2 galaxy ngc 3081. *Monthly Notices of the Royal Astronomical Society: Letters*, *417*(1), L46–L50.

Ricci et al. (2017). Bat agn spectroscopic survey. v. x-ray properties of the swift/bat 70-month agn catalog. *The Astrophysical Journal Supplement Series*, *233*(2), 17.

Ricci, C., Bauer, F. E., Treister, E., Romero-Cañizales, C., Arevalo, P., Iwasawa, K., Privon, G. C., Sanders, D. B., Schawinski, K., Stern, D., & Imanishi, M. (2016). NUSTAR Unveils a Heavily Obscured Low-luminosity Active Galactic Nucleus in the Luminous Infrared Galaxy NGC 6286. *ApJ*, *819*(1), Article 4, 4. https://doi.org/10.3847/0004-637X/819/1/4

Ricci, C., Ueda, Y., Koss, M. J., Trakhtenbrot, B., Bauer, F. E., & Gandhi, P. (2015a). Compton-thick Accretion in the Local Universe. *ApJ Letters*, *815*(1), Article L13, L13. https://doi.org/10.1088/2041-8205/815/1/L13

Ricci, C., Ueda, Y., Koss, M. J., Trakhtenbrot, B., Bauer, F. E., & Gandhi, P. (2015b). Compton-thick accretion in the local universe. *The Astrophysical Journal Letters*, *815*(1), L13.

Risaliti et al. (2002). Ubiquitous variability of x-ray-absorbing column densities in seyfert 2 galaxies. *The Astrophysical Journal*, *571*(1), 234.

Risaliti & Elvis, M. (2004). A panchromatic view of agn. In *Supermassive black holes in the distant universe* (pp. 187–224). Springer.

Risaliti, G., Elvis, M., Fabbiano, G., Baldi, A., & Zezas, A. (2005). Rapid compton-thick/compton-thin transitions in the seyfert 2 galaxy ngc 1365. *The Astrophysical Journal Letters*, *623*(2), L93.

Rivers, E., Baloković, M., Arévalo, P., Bauer, F. E., Boggs, S. E., Brandt, W. N., Brightman, M., Christensen, F. E., Craig, W. W., Gandhi, P., Hailey, C. J., Harrison, F., Koss, M., Ricci, C., Stern, D., Walton, D. J., & Zhang, W. W. (2015). The NuSTAR View of Reflection and Absorption in NGC 7582. *ApJ*, *815*(1), Article 55, 55. https://doi.org/10.1088/0004-637X/815/1/55

Rosario, D. J., Santini, P., Lutz, D., Shao, L., Maiolino, R., Alexander, D. M., Altieri, B., Andreani, P., Aussel, H., Bauer, F. E., Berta, S., Bongiovanni, A., Brandt, W. N., Brusa, M., Cepa, J., Cimatti, A., Cox, T. J., Daddi, E., Elbaz, D., Fontana, A., Förster Schreiber, N. M., Genzel, R., Grazian, A., Le Floch, E., Magnelli, B., Mainieri, V., Netzer, H., Nordon, R., Pérez Garcia, I., Poglitsch, A., Popesso, P., Pozzi, F., Riguccini, L., Rodighiero, G., Salvato, M., Sanchez-

Portal, M., Sturm, E., Tacconi, L. J., Valtchanov, I., & Wuyts, S. (2012). The mean star formation rate of X-ray selected active galaxies and its evolution from z ~2.5: results from PEP-Herschel. *AA*, *545*, Article A45, A45. https://doi.org/10.1051/0004-6361/201219258

Rose, T., Edge, A. C., Combes, F., Gaspari, M., Hamer, S., Nesvadba, N., Peck, A. B., Sarazin, C., Tremblay, G. R., Baum, S. A., Bremer, M. N., McNamara, B. R., O'Dea, C., Oonk, J. B. R., Russell, H., Salomé, P., Donahue, M., Fabian, A. C., Ferland, G., Mittal, R., & Vantyghem, A. (2019). Constraining cold accretion on to supermassive black holes: molecular gas in the cores of eight brightest cluster galaxies revealed by joint CO and CN absorption. *MNRAS*, *489*(1), 349–365. https://doi.org/10.1093/mnras/stz2138

Rossland, S., Wik, D. R., Grefenstette, B., Cappelluti, N., Civano, F., Gastaldello, F., Gilli, R., Harrison, F., Hornschemeier, A., Hickox, R., Krivonos, R., Madsen, K., Molendi, S., Ptak, A., Stern, D., & Zoglauer, A. (2023). Measuring the Cosmic X-Ray Background in 3-20 KeV with Stray Light from NuSTAR. *AJ*, *166*(1), Article 20, 20. https://doi.org/10.3847/1538-3881/acd0ae

Satyapal, S., Ellison, S. L., McAlpine, W., Hickox, R. C., Patton, D. R., & Mendel, J. T. (2014). Galaxy pairs in the Sloan Digital Sky Survey - IX. Merger-induced AGN activity as traced by the Wide-field Infrared Survey Explorer. *MNRAS*, *441*(2), 1297–1304. https://doi.org/10.1093/mnras/stu650

Schartmann, M., Meisenheimer, K., Camenzind, M., Wolf, S., & Henning, T. (2005). Towards a physical model of dust tori in Active Galactic Nuclei. Radiative transfer calculations for a hydrostatic torus model. *AA*, *437*(3), 861–881. https://doi.org/10.1051/0004-6361:20042363

Scharwächter, J., Dopita, M. A., Zuther, J., Fischer, S., Komossa, S., & Eckart, A. (2011). Extended Narrow-line Emission in the Bright Seyfert 1.5 Galaxy HE 2211-3903. *AJ*, *142*(2), Article 43, 43. https://doi.org/10.1088/0004-6256/142/2/43

Schoonjans, T., Brunetti, A., Golosio, B., Sanchez del Rio, M., Solé, V. A., Ferrero, C., & Vincze, L. (2011). The xraylib library for X-ray-matter interactions. Recent developments. *Spectrochimica Acta*, *66*(11-12), 776–784. https://doi.org/10.1016/j.sab.2011.09.011

Sengupta, D., Marchesi, S., Vignali, C., Torres-Albà, N., Bertola, E., Pizzetti, A., Lanzuisi, G., Salvestrini, F., Zhao, X., Gaspari, M., Gilli, R., Comastri, A., Traina, A., Tombesi, F., Silver, R., Pozzi, F., & Ajello, M. (2023). Compton-

thick AGN in the NuSTAR Era X: Analysing seven local CT-AGN candidates. *AA*, *676*, Article A103, A103. https://doi.org/10.1051/0004-6361/202245646

Seyfert, C. K. (1943). Nuclear emission in spiral nebulae. *The Astrophysical Journal*, *97*, 28.

Shakura, N. I., & Sunyaev, R. A. (1973). Reprint of 1973a&a.... 24.. 337s. black holes in binary systems. observational appearance. *A&A*, *500*, 33–51.

Silver, R., Torres-Albà, N., Zhao, X., Marchesi, S., Pizzetti, A., Cox, I., Ajello, M., Cusumano, G., La Parola, V., & Segreto, A. (2022). Compton-thick AGN in the NuSTAR Era. IX. A Joint NuSTAR and XMM-Newton Analysis of Four Local AGN. *ApJ*, *940*(2), Article 148, 148. https://doi.org/10.3847/1538-4357/ac9bf8

Silverman, J. D., Green, P. J., Barkhouse, W. A., Kim, D. .-., Aldcroft, T. L., Cameron, R. A., Wilkes, B. J., Mossman, A., Ghosh, H., Tananbaum, H., Smith, M. G., Smith, R. C., Smith, P. S., Foltz, C., Wik, D., & Jannuzi, B. T. (2005). Hard X-Ray-emitting Active Galactic Nuclei Selected by the Chandra Multiwavelength Project. *ApJ*, *618*(1), 123–138. https://doi.org/10.1086/425895

Slipher, V. M. (1917). The spectrum and velocity of the nebula N.G.C. 1068 (M 77). *Lowell Observatory Bulletin*, *3*, 59–62.

Soltan, A. (1982). Masses of quasars. *MNRAS*, *200*, 115–122. https://doi.org/10.1093/mnras/200.1.115

Stalevski, M., Fritz, J., Baes, M., Nakos, T., & Popović, L. Č. (2012). 3D radiative transfer modelling of the dusty tori around active galactic nuclei as a clumpy two-phase medium. *MNRAS*, *420*(4), 2756–2772. https://doi.org/10.1111/j.1365-2966.2011.19775.x

Stalevski, M., Ricci, C., Ueda, Y., Lira, P., Fritz, J., & Baes, M. (2016). The dust covering factor in active galactic nuclei. *MNRAS*, *458*(3), 2288–2302. https://doi.org/10.1093/mnras/stw444

Stanley, F., Harrison, C. M., Alexander, D. M., Swinbank, A. M., Aird, J. A., Del Moro, A., Hickox, R. C., & Mullaney, J. R. (2015). A remarkably flat relationship between the average star formation rate and AGN luminosity for distant X-ray AGN. *MNRAS*, *453*(1), 591–604. https://doi.org/10.1093/mnras/stv1678

Steffen, A. T., Strateva, I., Brandt, W. N., Alexander, D. M., Koekemoer, A. M., Lehmer, B. D., Schneider, D. P., & Vignali, C. (2006). The X-Ray-to-Optical Properties of Optically Selected Active Galaxies over Wide Luminosity and Redshift Ranges. *AJ*, *131*(6), 2826–2842. https://doi.org/10.1086/503627

Suganuma, M., Yoshii, Y., Kobayashi, Y., Minezaki, T., Enya, K., Tomita, H., Aoki, T., Koshida, S., & Peterson, B. A. (2006). Reverberation Measurements of the Inner Radius of the Dust Torus in Nearby Seyfert 1 Galaxies. *ApJ*, *639*(1), 46–63. https://doi.org/10.1086/499326

Tanimoto, A., Ueda, Y., Odaka, H., Kawaguchi, T., Fukazawa, Y., & Kawamuro, T. (2019a). XCLUMPY: X-Ray Spectral Model from Clumpy Torus and Its Application to the Circinus Galaxy. *ApJ*, *877*(2), Article 95, 95. https://doi.org/10.3847/1538-4357/ab1b20

Tanimoto, A., Ueda, Y., Odaka, H., Kawaguchi, T., Fukazawa, Y., & Kawamuro, T. (2019b). XCLUMPY: X-Ray Spectral Model from Clumpy Torus and Its Application to the Circinus Galaxy. *ApJ*, *877*(2), Article 95, 95. https://doi.org/10.3847/1538-4357/ab1b20

Tanimoto, A., Ueda, Y., Odaka, H., Yamada, S., & Ricci, C. (2022). NuSTAR Observations of 52 Compton-thick Active Galactic Nuclei Selected by the Swift/BAT All-sky Hard X-Ray Survey. *arXiv e-prints*, Article arXiv:2203.13266, arXiv:2203.13266.

Temi, P., Gaspari, M., Brighenti, F., Werner, N., Grossova, R., Gitti, M., Sun, M., Amblard, A., & Simionescu, A. (2022). Probing Multiphase Gas in Local Massive Elliptical Galaxies via Multiwavelength Observations. *ApJ*, *928*(2), Article 150, 150. https://doi.org/10.3847/1538-4357/ac5036

Thompson, T. A., Quataert, E., & Murray, N. (2005). Radiation Pressure-supported Starburst Disks and Active Galactic Nucleus Fueling. *ApJ*, *630*(1), 167–185. https://doi.org/10.1086/431923

Torres-Albà, N., Iwasawa, K., Díaz-Santos, T., Charmandaris, V., Ricci, C., Chu, J. K., Sanders, D. B., Armus, L., Barcos-Muñoz, L., Evans, A. S., Howell, J. H., Inami, H., Linden, S. T., Medling, A. M., Privon, G. C., U, V., & Yoon, I. (2018). C-GOALS. II. Chandra observations of the lower luminosity sample of nearby luminous infrared galaxies in GOALS. *AA*, *620*, Article A140, A140. https://doi.org/10.1051/0004-6361/201834105

Torres-Albà, N., Marchesi, S., Zhao, X., Ajello, M., Silver, R., Ananna, T. T., Baloković, M., Boorman, P. B., Comastri, A., Gilli, R., Lanzuisi, G., Murphy, K., Urry, C. M., & Vignali, C. (2021). Compton-thick AGN in the NuSTAR Era VI: The Observed Compton-thick Fraction in the Local Universe. *ApJ*, *922*(2), Article 252, 252. https://doi.org/10.3847/1538-4357/ac1c73

Torres-Albà, N., Marchesi, S., Zhao, X., Cox, I., Pizzetti, A., Sengupta, D., Ajello, M., & Silver, R. (2023a). Hydrogen column density variability in a sample of local

Compton-thin AGN. *AA*, *678*, Article A154, A154. https://doi.org/10.1051/0004-6361/202345947

Torres-Albà, N., Marchesi, S., Zhao, X., Cox, I., Pizzetti, A., Sengupta, D., Ajello, M., & Silver, R. (2023b). Hydrogen column density variability in a sample of local Compton-thin AGN. *AA*, *678*, Article A154, A154. https://doi.org/10.1051/0004-6361/202345947

Torres-Albà, N., Marchesi, S., Zhao, X., Cox, I., Pizzetti, A., Sengupta, D., Ajello, M., & Silver, R. (2023c). Hydrogen column density variability in a sample of local Compton-thin AGN. *AA*, *678*, Article A154, A154. https://doi.org/10.1051/0004-6361/202345947

Traina, A., Marchesi, S., Vignali, C., Torres-Albà, N., Ajello, M., Pizzetti, A., Silver, R., Zhao, X., Ananna, T., Baloković, M., Boorman, P., Gandhi, P., Gilli, R., & Lanzuisi, G. (2021). Compton-Thick AGN in the NuSTAR ERA VII. A joint NuSTAR, Chandra, and XMM-Newton Analysis of Two Nearby, Heavily Obscured Sources. *ApJ*, *922*(2), Article 159, 159. https://doi.org/10.3847/1538-4357/ac1fee

Ueda, Y., Akiyama, M., Hasinger, G., Miyaji, T., & Watson, M. G. (2014). Toward the standard population synthesis model of the x-ray background: Evolution of x-ray luminosity and absorption functions of active galactic nuclei including compton-thick populations. *The Astrophysical Journal*, *786*(2), 104.

Ueda, Y., Akiyama, M., Ohta, K., & Miyaji, T. (2003). Cosmological Evolution of the Hard X-Ray Active Galactic Nucleus Luminosity Function and the Origin of the Hard X-Ray Background. *ApJ*, *598*(2), 886–908. https://doi.org/10.1086/378940

Urry, C. M., & Padovani, P. (1995). Unified schemes for radio-loud active galactic nuclei. *Publications of the Astronomical Society of the Pacific*, *107*(715), 803.

Vasudevan, R. V., Mushotzky, R. F., & Gandhi, P. (2013). Can We Reproduce the X-Ray Background Spectral Shape Using Local Active Galactic Nuclei? *ApJ Letters*, *770*(2), Article L37, L37. https://doi.org/10.1088/2041-8205/770/2/L37

Vazquez, B., Galianni, P., Richmond, M., Robinson, A., Axon, D. J., Horne, K., Almeyda, T., Fausnaugh, M., Peterson, B. M., Bottorff, M., Gallimore, J., Eltizur, M., Netzer, H., Storchi-Bergmann, T., Marconi, A., Capetti, A., Batcheldor, D., Buchanan, C., Stirpe, G., Kishimoto, M., Packham, C., Perez, E., Tadhunter, C., Upton, J., & Estrada-Carpenter, V. (2015). Spitzer Space Telescope

Measurements of Dust Reverberation Lags in the Seyfert 1 Galaxy NGC 6418. *ApJ*, *801*(2), Article 127, 127. https://doi.org/10.1088/0004-637X/801/2/127

Verner, D. A., Ferland, G. J., Korista, K. T., & Yakovlev, D. G. (1996). Atomic Data for Astrophysics. II. New Analytic FITS for Photoionization Cross Sections of Atoms and Ions. *ApJ*, *465*, 487. https://doi.org/10.1086/177435

Weston, M. E., McIntosh, D. H., Brodwin, M., Mann, J., Cooper, A., McConnell, A., & Nielsen, J. L. (2017). Incidence of WISE -selected obscured AGNs in major mergers and interactions from the SDSS. *MNRAS*, *464*(4), 3882–3906. https://doi.org/10.1093/mnras/stw2620

Worsley, M., Fabian, A., Bauer, F., Alexander, D., Hasinger, G., Mateos, S., Brunner, H., Brandt, W. N., & Schneider, D. P. (2005). The unresolved hard x-ray background: The missing source population implied by the chandra and xmm—newton deep fields. *Monthly Notices of the Royal Astronomical Society*, *357*(4), 1281–1287.

Xue, Y., Wang, S., Brandt, W. N., Luo, B., Alexander, D., Bauer, F., Comastri, A., Fabian, A., Gilli, R., Lehmer, B., et al. (2012). Tracking down the source population responsible for the unresolved cosmic 6-8 kev background. *The Astrophysical Journal*, *758*(2), 129.

Yang, G., Boquien, M., Buat, V., Burgarella, D., Ciesla, L., Duras, F., Stalevski, M., Brandt, W. N., & Papovich, C. (2020). X-CIGALE: Fitting AGN/galaxy SEDs from X-ray to infrared. *MNRAS*, *491*(1), 740–757. https://doi.org/10.1093/mnras/stz3001

Yang, G., Brandt, W. N., Luo, B., Xue, Y. Q., Bauer, F. E., Sun, M. Y., Kim, S., Schulze, S., Zheng, X. C., Paolillo, M., Shemmer, O., Liu, T., Schneider, D. P., Vignali, C., Vito, F., & Wang, J. .-. (2016). Long-term X-Ray Variability of Typical Active Galactic Nuclei in the Distant Universe. *ApJ*, *831*(2), Article 145, 145. https://doi.org/10.3847/0004-637X/831/2/145

Yaqoob. (2012). The nature of the compton-thick x-ray reprocessor in ngc 4945. *Monthly Notices of the Royal Astronomical Society*, *423*(4), 3360–3396.

Yaqoob et al. (2015). A compton-thin solution for the suzaku x-ray spectrum of the seyfert 2 galaxy mkn 3. *Monthly Notices of the Royal Astronomical Society*, *454*(1), 973–990.

Yuan, F., & Narayan, R. (2014). Hot Accretion Flows Around Black Holes. *ARAA*, *52*, 529–588. https://doi.org/10.1146/annurev-astro-082812-141003

Zhao, X., Marchesi, S., & Ajello, M. (2019). Compton-thick AGN in the NuSTAR Era. IV. A Deep NuSTAR and XMM-Newton View of the Candidate Compton-thick AGN in ESO 116-G018. *ApJ*, *871*(2), Article 182, 182. https://doi.org/10.3847/1538-4357/aaf80b

Zhao, X., Marchesi, S., Ajello, M., Baloković, M., & Fischer, T. (2020). A Broadband X-Ray Study of a Sample of AGNs with [O III] Measured Inclinations. *ApJ*, *894*(1), Article 71, 71. https://doi.org/10.3847/1538-4357/ab879d

Zhao, X., Marchesi, S., Ajello, M., Cole, D., Hu, Z., Silver, R., & Torres-Albà, N. (2021). The properties of the AGN torus as revealed from a set of unbiased NuSTAR observations. *AA*, *650*, Article A57, A57. https://doi.org/10.1051/0004-6361/202140297

Zhao, X., Marchesi, S., Ajello, M., Marcotulli, L., Cusumano, G., La Parola, V., & Vignali, C. (2019). Compton-thick AGNs in the NuSTAR Era. II. A Deep NuSTAR and XMM-Newton View of the Candidate Compton-thick AGN in NGC 1358. *ApJ*, *870*(2), Article 60, 60. https://doi.org/10.3847/1538-4357/aaf1a0

Acknowledgements

Once, a great man named Karl Marx said, "The ideal is nothing else than the material world reflected by the human mind and translated into forms of thought." My ideas and perceptions of reality have been highly influenced by my father, Dhisankar Sengupta, and my maternal grandfather, Prof. Haridas Mukherjee, since my childhood. Along with that, the idea of creativity and life was instilled in me by my mother, Gargi Sengupta. I am forever grateful to them, for constructing my ideological foundation, upon which I am endeavoring to build my existence.

I would like to express my heartfelt gratitude to my supervisor, Prof. Cristian Vignali, and my co-supervisor, Dr. Stefano Marchesi, for their invaluable guidance and support whenever I reached out to them, even during their busiest moments. Thank you for your kindness and understanding, for being both my academic-father and academic-confidant during one of the darkest phases of my life. I would also express my gratitude to Dr. Núria Torres-Albà for her invaluable research advice and enriching conversations on topics like CT-AGN and academic life. Along with them, I would like to thank University of Bologna, INAF-OAS Bologna and Clemson University (USA) for providing access to facilities, fundings, and conducive research environment.

In addition to them, I am profoundly grateful to the following institutions and individuals whose steadfast support, guidance, and encouragement have been indispensable throughout my life's journey, enabling me to reach the point where I stand today. I also extend my heartfelt appreciation for their academic and non-academic engagement during my PhD days, which significantly contributed to the successful completion of this doctoral thesis:

- I would like to thank my schools- Sudhindranath Sishu Vidyalaya (Kolkata), Labanhrad Vidyapith (Kolkata) and Patha Bhavan (Kolkata) for providing me with a solid educational foundation and nurturing my creative side.

- I am deeply grateful to Gurudas College (University of Calcutta, Kolkata) and Presidency University (Kolkata) for nurturing my intellectual curiosity. The knowledge and skills I gained as a student and also as a Lecturer (in Gurudas College), have been invaluable in shaping my academic journey.

been invaluable to me. I am also grateful to her family for their unwavering support.

And finally, I would like to conclude this section by expressing my gratitude to all the researchers, teachers, students, workers, peasants, and members of the working class community worldwide for their unwavering support, both through their labor and their intellect, in striving to build a better society. As I conclude my thesis with the scientific objective to delve further into the nature of obscured AGN, I also hold a dream close to my heart: to unite all the workers of the world in the endeavor to create a society free from discrimination and human exploitation in the form of class, religion, caste, nationality, language or gender, paving the way for a brighter future.